PROGRESSIVE INTERLAMINAR FAILURE ANALYSIS IN
COMPOSITE MISSILE STRUCTURES

A THESIS SUBMITTED TO
THE GRADUATE SCHOOL OF NATURAL AND APPLIED SCIENCES
OF
MIDDLE EAST TECHNICAL UNIVERSITY

BY

BÜŞRA BARTAN KUMBASAR

IN PARTIAL FULFILLMENT OF THE REQUIREMENTS
FOR
THE DEGREE OF MASTER OF SCIENCE
IN
AEROSPACE ENGINEERING

SEPTEMBER 2016

Approval of the thesis:

PROGRESSIVE INTERLAMINAR FAILURE ANALYSIS IN COMPOSITE MISSILE STRUCTURES

submitted by **BÜŞRA BARTAN KUMBASAR** in partial fulfillment of the requirements for the degree of **Master of Science in Aerospace Engineering Department, Middle East Technical University** by,

Prof. Dr. Gülbin Dural Ünver
Dean, Graduate School of **Natural and Applied Sciences**   _____

Prof. Dr. Ozan Tekinalp
Head of Department, **Aerospace Engineering**   _____

Prof. Dr. Altan Kayran
Supervisor, **Aerospace Engineering Dept., METU**   _____

Examining Committee Members:

Assoc. Prof. Dr. Demirkan Çöker
Aerospace Engineering Dept., METU   _____

Prof. Dr. Altan Kayran
Aerospace Engineering Dept., METU   _____

Asst. Prof. Dr. Ercan Gürses
Aerospace Engineering Dept., METU   _____

Prof. Dr. Ozan Tekinalp
Mechanical Engineering Dept., METU   _____

Prof. Dr. K. Levend Parnas
Mechanical Engineering Dept., TED UNIV.   _____

Date: 06.09.2016

I hereby declare that all information in this document has been obtained and presented in accordance with academic rules and ethical conduct. I also declare that, as required by these rules and conduct, I have fully cited and referenced all material and results that are not original to this work.

Name, Last name: Büşra BARTAN KUMBASAR

Signature   :

ABSTRACT

PROGRESSIVE INTERLAMINAR FAILURE ANALYSIS IN COMPOSITE MISSILE STRUCTURES

Bartan Kumbasar, Büşra

M.S. Department of Aerospace Engineering

Supervisor: Prof. Dr. Altan Kayran

September 2016, 129 Pages

Interlaminar damage in composite structures is very crucial because it may cause splitting of the layers and lead to progressive failure of the whole structure. Delamination initiation and progression must be predicted accurately to aid the design of composites structures. Objective of the thesis is to investigate the interlaminar progressive failure behavior of the composite wing of a missile manufactured by twill composite by finite element analysis and tests. For this purpose, before the analyses and tests of the missile wing are performed, a simpler structure is modelled and tested to investigate the delamination behavior in the twill composite. In this study, simpler structure is selected as the open-hole plate. To initiate delamination, a thin film is inserted in a known location the composite plate in order to provoke delamination and examine the delamination progression behavior at different load levels. After the prediction of delamination initiation and propagation behavior by finite element analysis, open hole tensile test specimens are manufactured by the same twill composite which is used in the missile. Intact (OHT) and delaminated (DOHT) open hole tensile specimens are tested in tensile loading and comparisons are made with the experimental results. The load - displacement curve and load-strain curves obtained for the OHT specimens and DOHT specimens by the finite element analysis and the tests showed relatively good agreement. It is also shown that the increment of delamination areas measured for the DOHT specimens by the C-Scan differed from the finite element solution by %17. For the composite missile wings, similar analysis and test method is followed as the open-hole

specimens but in bending load condition. It is shown that the increment of delamination areas measured for DWs by the C-Scan differed from the finite element solution by %7.3. The preliminary analysis performed on a real structure such as a composite missile wing showed that with the cohesive zone modeling, the progression of delamination can be predicted fairly accurately.

Keywords: Delamination, Cohesive Zone Method, Finite Element Analysis, Double Cantilever Beam Test, End Notched Flexure Test, Open Hole Test, Missile Wing.

ÖZ

KOMPOZİT FÜZE YAPILARINDA KATMANLAR ARASI İLERLEMİŞ HASAR ANALİZİ

Bartan Kumbasar, Büşra

Yüksek Lisans, Havacılık ve Uzay Mühendisliği Bölümü

Tez Yöneticisi: Prof. Dr. Altan Kayran

Eylül 2016, 129 Sayfa

Kompozit yapılarda katmanlar arası ayrılma (delaminasyon) katmanların ayrılmasına ve bütün yapının ilerlemiş hasarına neden olduğu için oldukça tehlikelidir. Delaminasyon başlangıcı ve ilerlemesi kompozit yapıların tasarımına yardımcı olması için doğru bir şekilde tahmin edilebilmelidir. Bu tezin amacı "twill" (bir çeşit örgü kumaş) malzemeden üretilmiş olan kompozit bir füze kanadının katmanlar arası ilerlemiş hasar davranışını test ve sonlu elemanlar analizleriyle incelemektir. Bu amaçla füze kanadının analiz ve testleri yapılmadan önce, ilgili örgü malzemedeki delaminasyon daha basit bir yapıda incelenmiş ve modellenmiştir. Bu çalışmada basit yapı olarak delikli plaka seçilmiştir. Delaminasyonu başlatmak ve ilerleme davranışını farklı yük seviyelerinde incelemek için teflon film yeri bilinen bir bölgeye yerleştirilmiştir. Sonlu elemanlar analiziyle delaminasyon başlama ve ilerlemesi tahmin edildikten sonra, füzede kullanılan aynı örgü kumaşından delikli plakalar üretilmiştir. Filmsiz (OHT) ve filmli (DOHT) delikli plakalar çekme yüklemesine maruz bırakılmıştır ve karşılaştırmalar test sonuçlarıyla yapılmıştır. Yük-yerdeğiştirme ve yük-gerinim ölçer eğrileri OHT ve DOHT numuneleri için test ve analizlerle doğrulanmıştır. Böylece kompozitlerdeki 3 boyutlu katı elemanlı sonlu elemanlar delaminasyon analiz metodu doğrulanmıştır. Ayrıca C-Scan tarama yöntemiyle sonlu elemanlar analizleri sonuçları delaminasyon alanı artışı için filmli delikli plakalarda 17 % oranında tutmaktadır. Ardından kompozit kanatlar için delikli plakalar ile benzer eğme yüklemesiyle test ve analizler gerçekleştirilmiştir. C-Scan tarama yöntemiyle sonlu elemanlar analizleri sonuçları delaminasyon alanı artışı için filmli kanatlarda 7.3% oranında tutmaktadır. Böylece kompozit

bir füze kanadı gibi gerçek yapılar için yapılan kohezif bölge modeli içeren ön analizler, delaminasyon ilerlemesini oldukça doğru tahmin edebilmektedir.

Anahtar Kelimeler: Delaminasyon, Yapışkan Bölge Metodu, Sonlu Eleman Analizi, Çift Dirsek Kiriş Testi, Sonu Çentikli Esneklik Testi, Delikli Plaka Testi, Füze Kanadı.

To My Mom

ACKNOWLEDGMENTS

TABLE OF CONTENTS

LIST OF TABLES

TABLES

LIST OF FIGURES

FIGURES

NOMENCLATURE

CZM	Cohesive Zone Method
FEA	Finite Element Analyses
FEM	Finite Element Modeling
DCB	Double Cantilever Beam
ENF	End Notch Flexure
OHT	Open Hole Tensile Specimens without The Film
DOHT	Open Hole Tensile Specimens with The Film
W	Missile Wing without The Film
DW	Missile Wing with The Film

CHAPTER 1

1. INTRODUCTION

1.1. Overview

Composite material is defined as the combination of more than one material in order to create a superior material. The usage of composite materials is very extensive in aerospace industry because of their high specific stiffness, high specific strength, corrosion and chemical resistance. The widespread failure behavior of composites is fiber or matrix tension/compression failure, intralaminar failure, interlaminar failure, matrix cracking, fiber and matrix debonding [1] [2]. Interlaminar damage (i.e. delamination, debonding) in composite structures is very critical because it causes progressive failure of layer separation in laminated composites [3] [4]. There are many examples on the use of cohesive zone method (CZM) and interlaminar progressive failure behavior in the literature [5]–[7].

Laminated composites are widely preferred in aerospace industry because of their high performance. A laminated composite consists of multiple lamina and is designed by selection of the count, direction of sequence, thickness and material of the lamina [8]. The strength of the epoxy or resin layer between the laminas is very weak in the thickness direction so it may lead the delamination.

Delamination can easily grow under the static, quasi-static or dynamic loads and the loss of the stiffness occurs in the thickness direction. Therefore, it causes the progressive and ultimate failure in laminated composites. Finite element modelling of cohesive behavior must be confirmed by tests in order to verify the delamination beginning and progress.

The expectation from a missile is that missile should perform its mission with success. The aim is the completion of the mission for the missile without catastrophic

delamination. Typical trajectory for a missile is represented in Figure 1. In Figure 1, load cases 2, 3 or 4 might induce the highest loads during the motion of the missile. A missile might have very short duration in operation but probable manufacturing defects in the form of disbonds may be the main source of failure during critical load cases in a missile structure. Disbonds may exist in many regions in a missile structure. Therefore, finite element analysis based check of failure progression must be performed to cover many manufacturing defect configurations. In this respect, finite element analysis of the missile structure has significant advantages over testing due to high number of manufacturing defect configurations that may exist. In this study, a composite missile wing is exposed to bending load condition until the wing is broken.
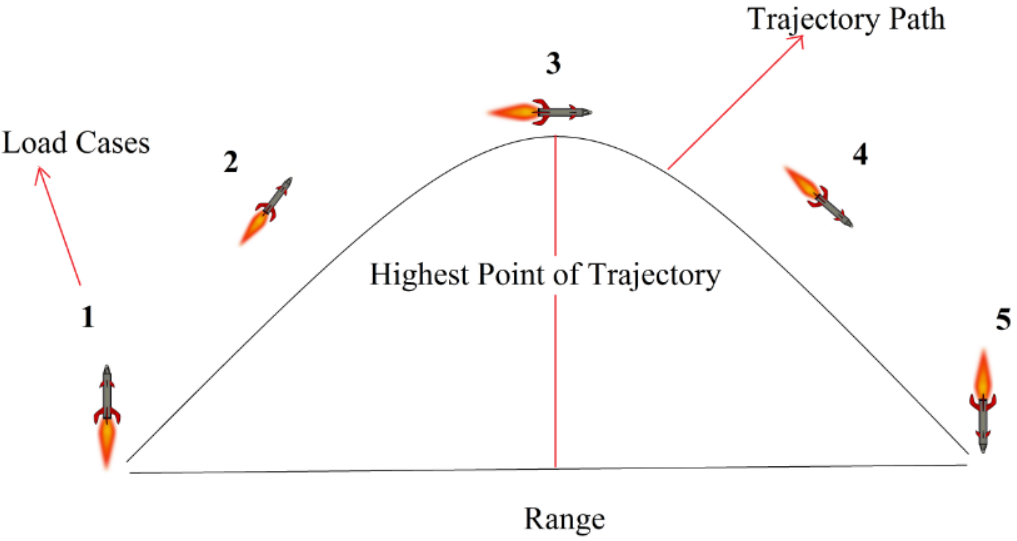
Figure 1: The trajectory for a missile

To model the delamination, Cohesive Zone Method (CZM) is used as an approach to Fracture Mechanics. In CZM, delamination between the layers is represented by cohesive elements in composite structures. Delamination initiation and propagation in the structure is predicted with the behavior of these interface elements. In CZM, damage mechanism is modeled by traction-displacement constitutive relationships. Finite element analyses (FEA) are conducted for delamination analysis in composites

using three dimensional (3D) solid cohesive elements. Finite element analyses are performed by ABAQUS [9].

1.2. Motivation

As already stated in the overview section, interlaminar damage (i.e. delamination) in composite structures is very dangerous because it causes progressive failure of the composite structure. Delamination initiation and progression must be predicted accurately to aid the design of composite structures. The current trend in the failure analysis of composite structures is to analyze the structures as manufactured. That is, after the manufacturing of the composite structure or component, non-destructive evaluation of the structure is made and finite element analysis of the structure is performed with defects identified added to the finite element model by proper modeling approaches. Present study, although not exactly the same, in a way follows a similar approach to check the delamination progression behavior in composite missile wing structures.

1.3. Objective

Objective of the thesis is to investigate the interlaminar progressive failure behavior of the composite wing of a missile manufactured by carbon-epoxy twill composite by finite element analyses and tests. Figure 2 shows the wrap tow and the fill tow in a planar view of the twill composite used in this study. Prepreg layers are stacked together in order to obtain composite parts with different angle orientations. In Figure 2, it can be seen that a single horizontal tow passes over two vertical tows and then under two vertical tows. Therefore this type of the twill is called as 2/2. [10]
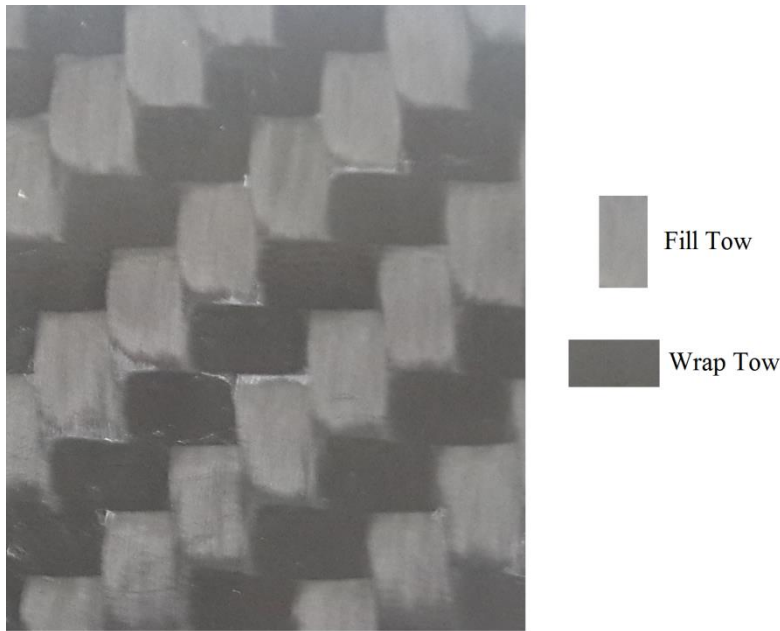
Figure 2: A planar view of 2/2 twill weave

For the purpose of the study, before the analyses and tests of the missile wing are performed, a simpler structure is modelled and tested to investigate the delamination behavior in the twill composite. In this study, simpler structure is selected as the open-hole plate. In the literature, twill composite is used in composite structures such as the double-cantilever beam (DCB) and the end notched flexure (ENF) specimens for fracture toughness measurements, open hole tensile specimens, composite wings and other parts [11] [12] [13] [14] [15]. To initiate delamination, a thin film (i.e. polytetrafluoroethylene, PTFE) is inserted in a known location the composite plate in order to examine the delamination behavior. After the prediction of delamination initiation and propagation by finite element analysis, open hole tensile test specimens are manufactured by the same twill composite which is used in the missile. Intact (OHT) and delaminated (DOHT) open hole tensile specimens are tested in tensile loading and comparisons are made with the experimental results.

For the composite missile wing, a thin film is also inserted in a known location of the wing in order to examine the delamination behavior. Composite wings without the teflon film (W) and composite wings with the film (DW) are exposed bending load condition and they are tested and analyzed subject to same conditions.

4

The main objective of the study is to compare the increment in the delamination area obtained by finite element based delamination analysis and tests in the missile wing at different load levels. Having good agreement between the analysis and test results indicates that CZM approach can predict the extent of damage accurately. Reliable analysis model allows performing frequent design changes faster and greatly improves in the design process.

1.4. Content

Chapter 2 is about the strain and the stress based failure criteria which are used for the prediction of failure in composites and the delamination in composites. The composites generally fail in two basic failure modes: failure of individual plies and delamination between the plies. In this study, for the determination of the placement of the thin film insert for the onset of delamination, the critical location in the open-hole specimens is predicted utilizing the failure criteria available in the literature for the failure of individual plies. Failure analysis results obtained with the Tsai-Wu, Tsai-Hill, maximum stress and Hashin failure criterion are compared in order to decide the most appropriate intralaminar failure criterion for the failure of the twill composite and for the determining the most appropriate location of the thin film insert. To implement the failure criteria, UVARM subroutine is written for ABAQUS to perform failure analysis of open hole tensile specimens. On the other hand, delamination can easily grow under the static, quasi-static or dynamic loads and the loss of the stiffness occurs in the thickness direction. Therefore, it causes the progressive and ultimate failure in laminated composites. Failure modes in delamination and delamination analysis method are mentioned in this chapter.

Chapter 3 is about verification of the analysis model with a study from the literature. In this study, implicit finite element analysis is used in the 3D models of the double-cantilever beam (DCB) and the end notched flexure (ENF) specimens with 3D cohesive elements in the delamination interface. For the verification study, delamination analysis results of the present study are compared with the DCB and ENF analysis and test data of Travesa [16].

In Chapter 4, the carbon-epoxy twill composite material is used in the present study and its fracture toughness data is obtained from tests to be used in open hole tensile and wing bending analysis. This chapter describes the test and analysis verification of the DCB and ENF tests performed to determine the fracture toughness data of the twill composite.

In Chapter 5, after the completion of delamination initiation and propagation study for the DCB and the ENF specimens by finite element analysis, open hole tensile specimens which are manufactured by the same twill composite is tested in tensile loading condition. Intact (OHT) and delaminated (DOHT) open hole tensile specimens are tested in tensile loading and comparisons are made with the experimental results. Delamination progression test and analysis study is presented.

In Chapter 6, after the completion of delamination initiation and propagation study for the DCB, the ENF, the OHT and the DOHT specimens by FEA, composite missile wings manufactured by the same twill composite are tested in bending loading. Delamination progression test and analysis study are presented.

The general concept of this thesis is given as a flowchart in Figure 3.
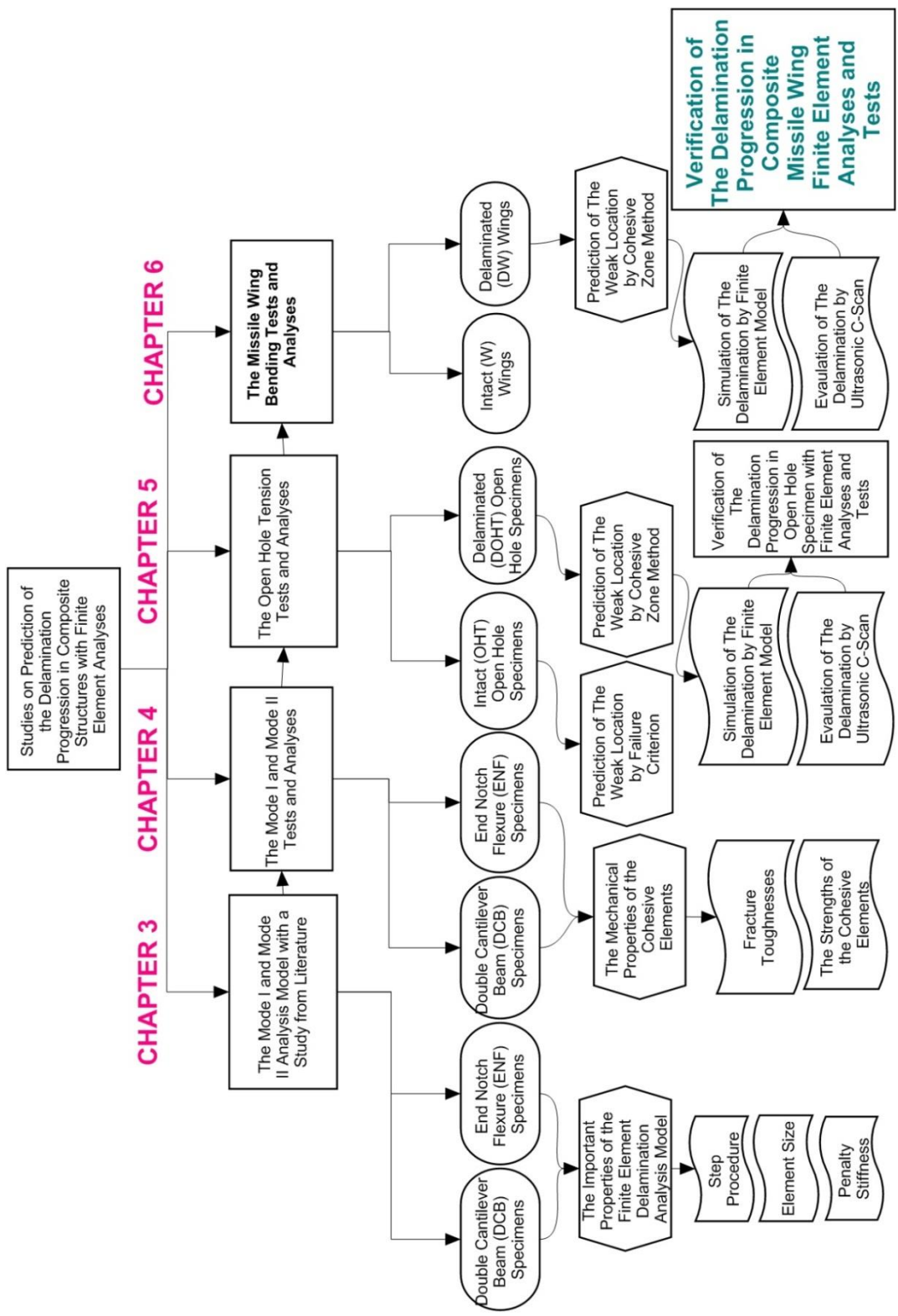
Figure 3: The flowchart of this thesis

CHAPTER 2

2. INTRALAMINAR AND INTERLAMINAR FAILURES

In this chapter, the strain and the stress based failure criteria which are used for the prediction of failure in composites and the delamination in composites are discussed. In this study, for the determination of the placement of the thin film insert for the onset of delamination, the critical location in the open-hole specimens is predicted utilizing the failure criteria available in the literature for the failure of individual plies.

2.1. Failure Theories

In general, strain or stress based failure criteria are used for the prediction of failure in composites. The composites generally fail in two basic failure modes: failure of individual plies and delamination between plies. In this study, for the determination of the placement of the thin film insert for the onset of delamination, the critical location in the open-hole specimens is predicted utilizing failure criteria available in the literature for failure of individual plies. Failure analysis results obtained with the Tsai-Wu, Tsai-Hill, maximum stress and Hashin failure criteria are compared in order to decide on the most appropriate intralaminar failure criterion for the failure of the twill composite and for the determining the most appropriate location of the thin film insert. To implement the failure criteria, UVARM subroutine is written for ABAQUS to perform failure analysis of open hole tensile specimens.

2.1.1. Tsai-Wu Failure Criterion

The failure theory is a relatively new multi-axial strength theory [17]. The Tsai–Wu failure criterion provides that for no failure the constraint given in Eq. 2.1 should be satisfied.

$$F_{11}(\sigma_1)^2 + F_{22}(\sigma_2)^2 + F_{66}(\sigma_6)^2 + 2F_{12}\sigma_1\sigma_2 + F_1\sigma_1 + F_2\sigma_2 - 1 \leq 0 \qquad (2.1)$$

The strength parameters F_{11}, F_{22}, F_{66}, F_1, F_2 and F_{12} are given by

$$F_{11} = \frac{1}{X_T X_C}, \qquad F_{22} = \frac{1}{Y_T Y_C}, \qquad F_{66} = \frac{1}{(S)^2},$$

$$F_1 = \frac{1}{X_T} - \frac{1}{X_C}, \quad F_2 = \frac{1}{Y_T} - \frac{1}{Y_C}, \quad F_{12} = -\frac{1}{2}\sqrt{F_{11} F_{22}} \qquad (2.2)$$

where σ_1 and σ_2 are the in-plane stresses in the longitudinal and transverse directions and σ_6 is the in-plane shear stress. X_T and X_C are the longitudinal tensile and compressive strengths, respectively. Y_T and Y_c are the tensile and compressive strengths for the transverse direction and S is the in-plane shear strength. [17] [18].

2.1.2. Tsai-Hill Failure Criterion

Tsai-Hill failure criterion is a quadratic failure criterion given by Eqn. 2.3 [18].

$$F_{11}(\sigma_1)^2 + F_{22}(\sigma_2)^2 + F_{66}(\sigma_6)^2 + 2F_{12}\sigma_1\sigma_2 \geq 1 \qquad (2.3)$$

The strength parameters F_{11}, F_{22}, F_{66} and F_{12} are given by

$$F_{11} = \frac{1}{X^2}, \; F_{22} = \frac{1}{Y^2}, \; F_{66} = \frac{1}{S^2}, \quad F_{12} = -\frac{1}{2}\left(\frac{1}{X^2} - \frac{1}{Y^2}\right) \qquad (2.4)$$

where σ_1 and σ_2 are the in-plane stresses in the longitudinal and transverse directions and σ_6 is the in-plane shear stress. X is the longitudinal tensile or compressive strengths, respectively. Y is the tensile or compressive strength in the transverse direction and S is the in-plane shear strength [18].

2.1.3. Maximum Stress Failure Criterion

The maximum stress criterion is the simplest stress-based failure criterion. No interaction exists between the failure modes in the maximum stress criterion so its accuracy is limited. The failure begins if at least one of the criteria given by Eqn. (2.5) is satisfied for the maximum stress failure criterion [18].

$$\left|\frac{\sigma_1}{X}\right| \geq 1, \; \left|\frac{\sigma_2}{Y}\right| \geq 1, \; \left|\frac{\sigma_6}{S}\right| \geq 1 \qquad (2.5)$$

where σ_1 and σ_2 are the in-plane stresses in the longitudinal and transverse directions and σ_6 is the in-plane shear stress. X is the longitudinal tensile or compressive

strengths, respectively. Y is the tensile or compressive strengths in the transverse direction and S is the in-plane shear strength [18].

2.1.4. Hashin Failure Criterion

Hashin failure criterion examines the failure such as tension and compression modes because different failure mechanisms occur in tension and compression. In the following, the failure modes are summarized for the case of plane stress [19]:

Tensile fiber mode, $\sigma_1 \geq 0$

$$\left(\frac{\sigma_1}{X_T}\right)^2 + \left(\frac{\sigma_6}{S}\right)^2 \geq 1 \tag{2.6}$$

Compressive fiber mode, $\sigma_1 < 0$

$$\left(\frac{\sigma_1}{X_C}\right)^2 \geq 1 \tag{2.7}$$

Tensile matrix mode, $\sigma_2 > 0$

$$\left(\frac{\sigma_2}{Y_T}\right)^2 + \left(\frac{\sigma_6}{S}\right)^2 \geq 1 \tag{2.8}$$

Compressive matrix mode, $\sigma_2 < 0$

$$\frac{\sigma_2}{Y_C}\left[\left(\frac{Y_C}{2S}\right)^2 - 1\right] + \frac{\sigma_2}{2S} + \left(\frac{\sigma_6}{S^2}\right)^2 \geq 1 \tag{2.9}$$

where σ_1 and σ_2 are the in-plane stresses in the longitudinal and transverse directions and σ_6 is the in-plane shear stress. X_T and X_C are the longitudinal tensile and compressive strengths, respectively. Y_T and Y_c are the tensile and compressive strengths for the transverse direction and S is the in-plane shear strength.

2.2. Delamination in Composites

Delamination in composites results in the loss of load carrying capacity that causes reduction of the material stiffness. Stiffness degradation is achieved by using cohesive elements by means of traction-separation law. Cohesive stress zone

approach is applied to fracture mechanics first by Dugdale [20] and Barenblatt [21]. Then, the concept of the cohesive zone is improved by Needleman [22]. The concept of the cohesive elements is based on modelling separation between two initially bonded surfaces. In cohesive zone modeling, bonded interface, adhesive connections and gaskets are represented by cohesive elements with the traction-separation law. The main stages of delamination damage are commonly divided into damage initiation and damage evolution.

2.2.1. Delamination Initiation and Propagation

Delamination initiation is governed by the traction-separation law. Traction-separation law refers to the relation between the peak strength or the traction (τ) and the displacement jump (Δ) between the layers. Damage initiation is based on the material strength with a stress limit for the cohesive zone. The damage starts between the layers when the stress value is at the stress limit. There is a decline in the stress while the damage propagates and the displacement between the layers increases. Finally, a new crack surface is created and fracture energy when the stress reaches to zero level as shown in Figure 4 [23] [24].
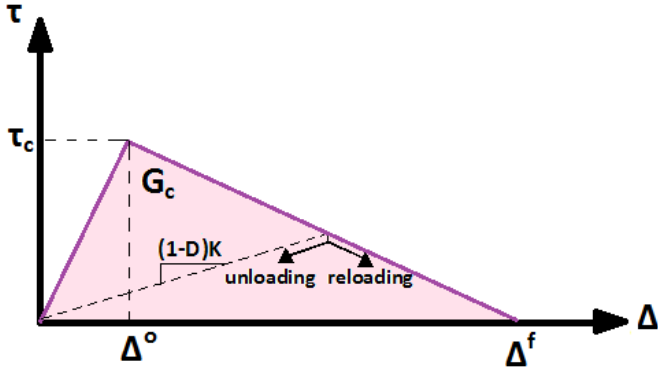
Figure 4: Typical traction-separation law (Bi-linear cohesive law) [23]

A crack propagates along the bonded surfaces for an isotropic and homogeneous material. However, the crack propagates in its own plane for laminated composites because of the low toughness of the interface. The energy released, ΔU, is the

required energy for crack propagation and it is given by the difference between the elastic strain energies before and after the crack propagation. The rate of the energy released per unit of crack surface area is the energy release rate, G given by Equation 2.10.

$$G = -\frac{\Delta U}{\Delta A} \qquad (2.10)$$

The crack propagates, when the energy release rate is higher than or equal to the critical fracture energy, G_c. Critical fracture energy is the area under the traction-separation law curve shown in Figure 4.

2.2.2. Failure Modes

The basic failure modes for delamination are the opening mode (Mode I), the sliding shear mode (Mode II), the tearing shear mode or scissoring mode (Mode III) and the mixed-mode. The material properties governing the delamination onset and growth (fracture toughness, interface strength etc.) are obtained from tests for these modes and they are given as input data for the delamination analysis. These failure modes are shown in Figure 5.
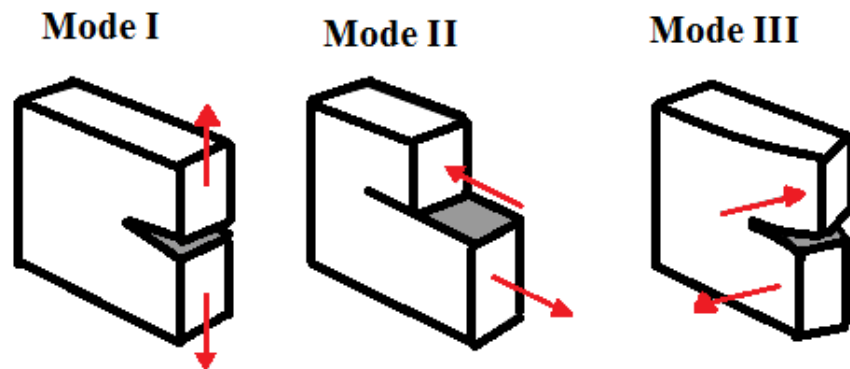
Figure 5: Failure modes

2.2.2.1.Mode I Failure Mode

Delamination is a great weakness of laminated composite materials and detection the strength of the fiber reinforced polymer materials to interlaminar fracture under static

or dynamic loading is very important so as to determine allowable and damage tolerance design in the structures. The geometry used to determine the interlaminar fracture toughness in Mode I (G_{Ic}) is the double-cantilever beam (DCB) specimen, shown in Figure 6. This specimen is made of unidirectional fiber-reinforced laminate containing a thin insert at the mid-plane near the loaded end.
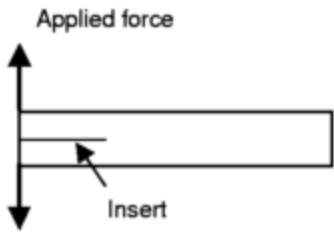
Figure 6: DCB test specimen [1]

The thickness of the inserted film, the data reduction procedures for obtaining fracture toughness values and the most proper load mechanism are suggested with a generic round-robin test program. The delaminations in composite structures occur in interfaces between layers with different orientations instead of unidirectional (0°) plies. Many results in the literature show that unidirectional composites have the most conservative values for G_{Ic}. Thus, it is important to calculate the interlaminar fracture toughness for interfaces between layers with different orientations [1].

2.2.2.2. Mode II Failure Mode

There are four test specimens in order to measure of interlaminar fracture toughnesses under Mode II loading [4] [5]. These are the end notched flexure specimen (ENF), the stabilized end notched flexure specimen (SENF), the four point end notched flexure specimen (4ENF), and the end loaded split specimen (ELS). The most common specimen is the ENF test specimen as shown in Figure 7. However, it has problems based on the unstable crack propagation for short crack lengths. Feedback load control of the test machine can be used so as to stabilize the ENF test

[1]. As in the case of mode I crack propagation test, ENF tests are made to calculate the interlaminar fracture toughness in Mode II, G_{IIC} [25].
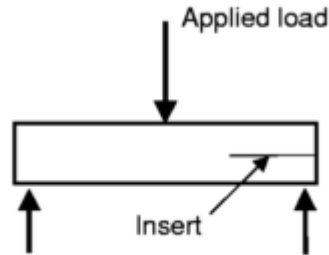
Figure 7: ENF test specimen [1]

2.2.2.3.Mode III Failure Mode

The most researches on the calculation of interlaminar fracture toughness has been performed for Mode I and Mode II loading. Mode III delamination tests are also required to have an exact characterization of the fracture procedure. The effect of the transverse shear modulus G_{23} on the Mode III toughness was studied by Li and O'Brien [2]. G_{23} is a requirement for the analysis and the determination of G_{23} is difficult experimentally. The assuming G_{23} to be equal to G_{12} results in a conservative evaluation for the initial delamination length [1].

2.2.2.4.Mixed-Mode Failure

The general specimen for mixed-mode fracture is the mixed-mode bending (MMB) specimen, shown in Figure 8, which was proposed by Reeder and Crews [26]. This specimen was later re-designed in order to reduce geometric nonlinearities. The main advantage of the MMB test method is the possibility of using practically the same specimen geometry for Mode I tests and making it possible to control mixed mode test by varying the mixed mode ratio from pure Mode I to pure Mode II [1]. The different mixed-mode ratios can be measured, if the location of the applied load point (the loading arm) is changed [23].
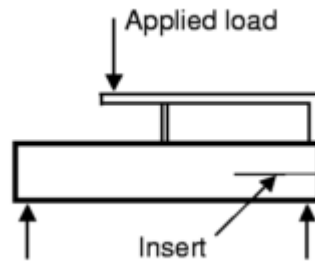
Figure 8: MMB test specimen [1]

2.2.3.Delamination Analysis Methods

2.2.3.1.Virtual Crack Closure Technic (VCCT)

The most widely and successfully used technique for the delamination propagation is the Virtual Crack Closure Technique (VCCT) [27]. VCCT is related with Irwin's assumption that the energy absorbed in the expanding crack is equal to the work required to close the crack to its initial length. The energy release rates can be calculated from the nodal forces and displacements taken from a finite element model [1]. The first VCCT approach to compute Strain Energy Release Rates, beginning from forces at the crack tip and relative displacements of the crack faces behind it, was recommended for four node elements. A debonding between two adjacent parts of the same structure along the thickness is a delamination. This debonding can be modelled in the finite element method with keeping not merged nodes on two attached faces of the volumes or surfaces. Thus, the Strain Energy Release Rate along the crack front can be calculated by using only nodal forces and displacements. An example of application of the VCCT to a circular delamination is shown in Figure 9 [7].

16

$$G_I^H = \frac{1}{2} \frac{1}{(A_1 + A_2)/2} F_n^H \left(u_n^M - u_n^L \right)$$

$$G_{II}^H = \frac{1}{2} \frac{1}{(A_1 + A_2)/2} F_t^H \left(u_t^M - u_t^L \right)$$

$$G_{III}^H = \frac{1}{2} \frac{1}{(A_1 + A_2)/2} F_s^H \left(u_s^M - u_s^L \right)$$
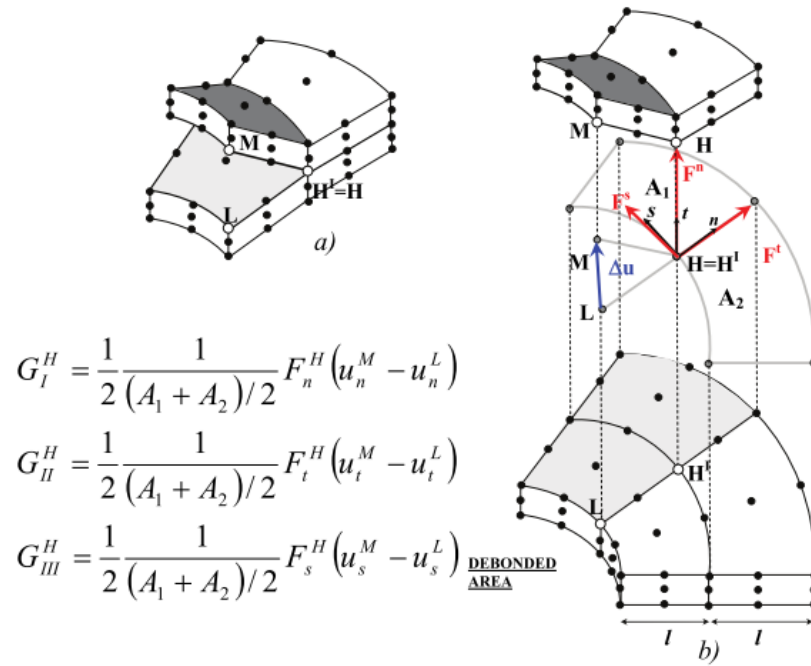
Figure 9: Force at the crack tip (measure at the node H=H') and displacements (components of the vector connecting the nodes L and M) [7]

2.2.3.2.The Extended Finite Element Method (XFEM)

The XFEM is related with the method of partition of integrity. The crack extension can be modelled without remeshing in this method, so the XFEM is an effective way to reduce mesh dependency when it is used to analyze crack growth. The discontinuity field is approximated by the enrichment of degrees of freedom in the region of concern, such as the potential damage zone. Therefore, only some degrees of freedom of nodes are improved [28]. As a result, a powerful method has been developed in order to completely use the potential of cohesive-zone models for the arbitrary crack propagation.

Generally two criteria are needed so as to model the crack propagation with the XFEM,:

•a criterion to decide whether a crack progresses or not,

•a criterion to define the direction of the crack progression [29].

2.2.3.3. Cohesive Zone Method (CZM)

In this thesis CZM is used to model the delamination in finite element analyses. Cohesive stress zone approach is used in fracture mechanics first by Dugdale [20] and Barenblatt [21]. Then, the concept of CZM has been used by Needleman [22] to simulate fast crack growth in brittle solids. The basic idea of the CZM is that all the inelastic effects that occur at the vicinity of a crack can be lumped into a surface – cohesive damage zone [30]. In CZM, there is no requirement for the definition of an initial crack, the initiation and propagation of damage can both be simulated. This method is based on a relationship between stresses and relative displacements at points where damage can occur [31] [32].

The cohesive elements are located between the layers where debonding is expected to progress. The connectivity of cohesive elements is like as continuum elements. The geometric features of a 3D cohesive element are shown in Figure 10 [9].
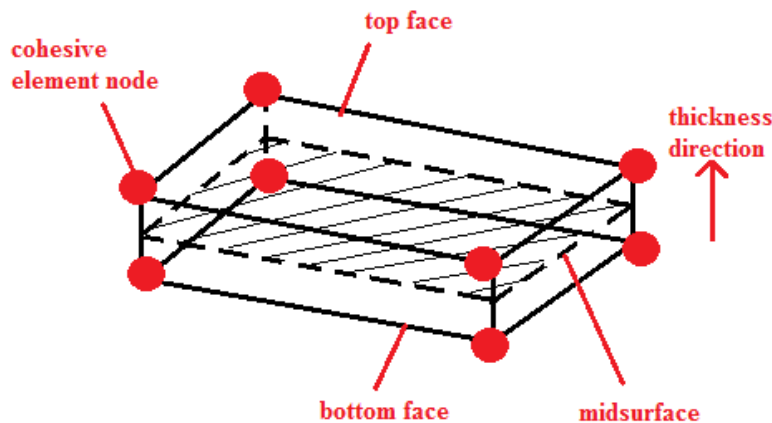
Figure 10: The representation of a 3D cohesive element [9]

In composite structures, the delamination generally grows such as under mixed-mode loading. Thus, mixed-mode delamination is the problem for the formulation of the cohesive elements [23] [33]. The damage onset can be obtained easily by the allowable tractions and the allowable strengths for pure mode I, II or III loading.

However, in mixed-mode loading, the damage onset can occur before any of the tractions or the strengths reach their allowable limits. Thus, a mixed-mode criterion is a requirement in order to make a connection between components of the energy release rate [23].

Delamination onset and delamination propagation are simulated by the damage model. A single scalar variable, d, is used to track the damage at the interface under general loading cases. An initiation criterion generates from the Benzeggagh–Kenane fracture criterion (B-K) [23].

Interpenetration of the faces of the crack during closing is prevented by the constitutive model and a criterion from the Fracture Mechanics evaluates the crack propagation. The parameter λ is the norm of the equivalent displacement jump norm, and it is used to compare different phases of the displacement jump stage so that it is possible to describe 'loading', 'unloading' and 'reloading'. The equivalent displacement jump is a non-negative and continuous function, defined as [23]:

$$\lambda = \sqrt{\langle \Delta_3 \rangle^2 + \langle \Delta_{shear} \rangle^2} \qquad (2.11)$$

where $\langle . \rangle$ is the MacAulay bracket defined as $\langle x \rangle = \frac{1}{2}(x + |x|)$, which adjusts any negative values to zero. The term Δ_3 is the displacement jump in mode I, i.e., normal to the mid-plane, and Δ_{shear} is the tangential displacement calculated as the Euclidean norm of the displacement jump in mode II and in mode III [23]:

$$\Delta_{shear} = \sqrt{\langle \Delta_1 \rangle^2 + \langle \Delta_2 \rangle^2} \qquad (2.12)$$

where Δ_1 and Δ_2 are displacement jumps. A bilinear cohesive law for mixed-mode delamination can be written by determining the initial damage threshold Δ^o from the criterion for damage initiation and the final displacement jump, Δ^f, from the formulation of the propagation surface or propagation criterion. For the B-K fracture criterion, the mixed-mode displacement jump for damage initiation is [23]:

$$(\Delta^o) = \left\{ (\Delta_3^0)^2 + [(\Delta_{shear}^0)^2 - (\Delta_3^0)^2]\left(\frac{G_{II}+G_{III}}{G_T}\right)^\eta \right\}^{1/2} \qquad (2.13)$$

where the B-K parameter η is obtained by curve-fitting the toughness of mixed-mode tests and the fracture mode ratio is [23]:

$$\left(\frac{G_{II}+G_{III}}{G_T}\right) = \frac{\beta^2}{1+2\beta^2-2\beta} \tag{2.14}$$

and where the displacement jump ratio is defined as [23]:

$$\beta = \frac{\Delta_{shear}}{\Delta_{shear}+\langle\Delta_3\rangle} \tag{2.15}$$

The displacement jump for final fracture is also obtained from critical displacement jumps as [23]:

$$(\Delta^f) = \Delta_3^0\Delta_3^f + \frac{\left(\Delta_{shear}^0\Delta_{shear}^f - \Delta_3^0\Delta_3^f\right)\left(\frac{G_{II}+G_{III}}{G_T}\right)^\eta}{\Delta^0} \tag{2.16}$$

During loading or overload, the state of damage d is afunction of the current equivalent displacement jump λ [23]:

$$d = \frac{\Delta^f(\lambda-\Delta^0)}{\lambda(\Delta^f-\Delta^0)} \tag{2.17}$$

The corresponding tractions can be written as [23]:

$$\tau_i = D_{ij}\Delta_j = \bar{\delta}_{ij}K\left[1 - d\left(1 + \bar{\delta}_{3j}\frac{\langle-\Delta_j\rangle}{\Delta_j}\right)\right]\Delta_j \tag{2.18}$$

where the Kronecker $\bar{\delta}_{ij}$ is used to prevent the interpenetration of the surfaces of a damaged element when contact starts [23] and K is the penalty stiffness of the cohesive elements.

CHAPTER 3

3. COHESIVE ZONE METHOD IN FINITE ELEMENT ANALYSIS

In this chapter, verification of the delamination analysis model with a study from the literature is presented. In this study, implicit finite element analysis is used in the 3D models of the double-cantilever beam (DCB) and the end notched flexure (ENF) specimens with 3D cohesive elements in the delamination interface. For the verification study, delamination analysis results of the present study are compared with the DCB and ENF analysis and test data of Travesa [16].

3.1. Verification study for cohesive zone modeling

For the verification study on the cohesive zone modeling, three dimensional models of Double Cantilever Beam (DCB) and End Notch Flexure (ENF) specimens are generated in ABAQUS with 3D cohesive elements in the delamination interface [34]. In the literature, for the delamination analysis in 3D, generally explicit finite element analysis is performed for better convergence characteristics. In the present study, implicit finite element analysis is used in the 3D models of the DCB and ENF specimens with 3D cohesive elements in the delamination interface. For the verification study, delamination analysis results of the present study are compared with the DCB and ENF analysis and test data of Travesa [16].

DCB and ENF analysis and test data of the study by Travesa [16] are taken as reference to build the finite element model for the delamination analysis and to compare the results of the present analysis with the results of the Travesa [16]. The finite element models of the DCB and ENF specimens, shown in Figure 11 and Figure 12, are generated in ABAQUS. DCB specimen is exposed to pure Mode I loading in opening mode. ENF specimen is exposed to pure Mode II loading in sliding-shear mode. DCB specimen is clamped at the end of the specimen whereas

21

ENF specimen is pinned at the ends of the specimen and three point bending simulation is performed. The applied displacements at the end of the DCB specimen are 4.5 mm in top and bottom directions. The applied displacement for the ENF specimen is 6.5 mm in the middle of the specimen.
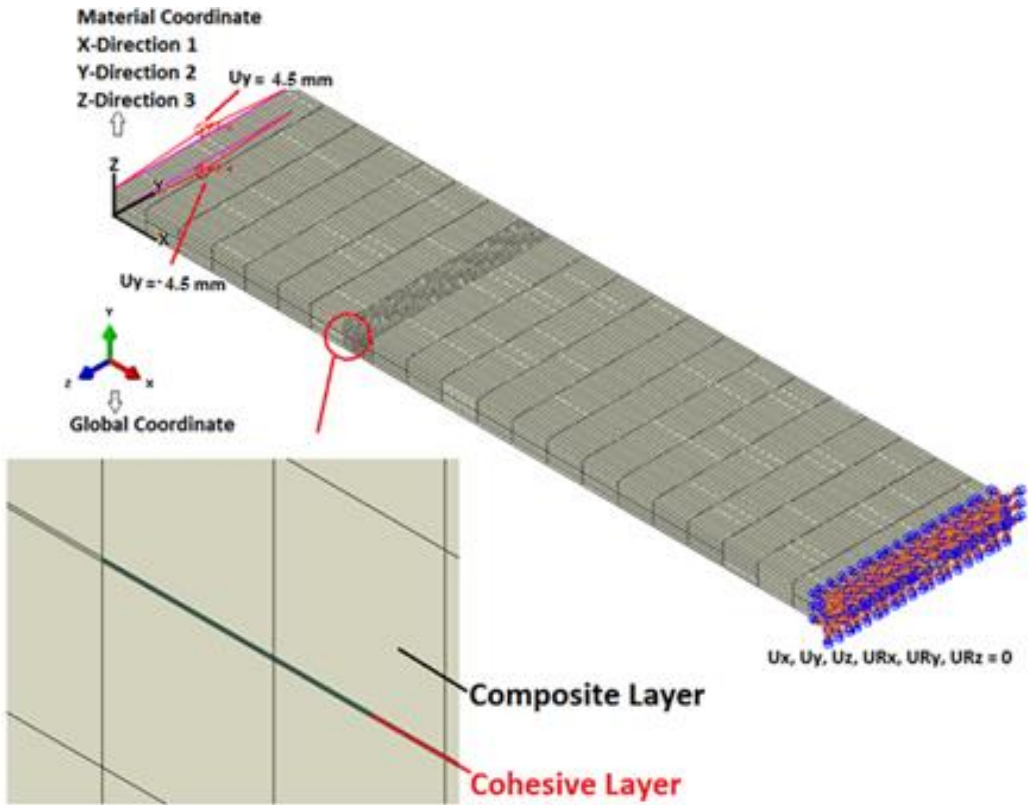
Figure 11: Finite element model for the DCB specimen
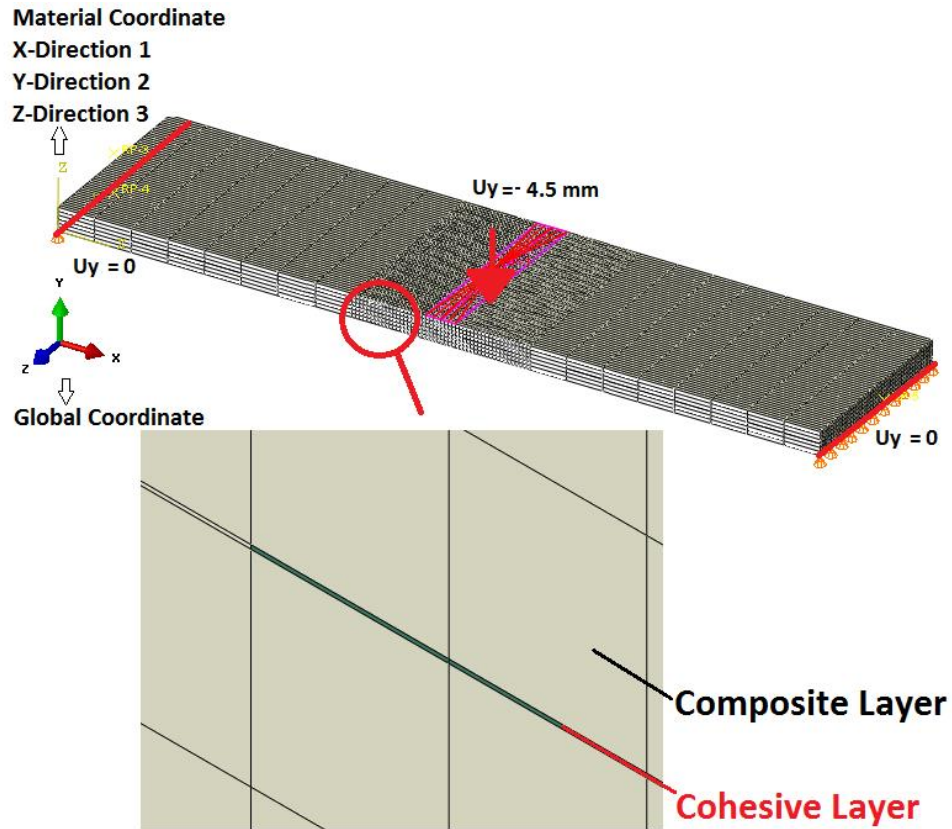
Figure 12: Finite element model for the ENF specimen

The ply properties of the unidirectional AS4/PEEK carbon fiber reinforced composite, used by Travesa [16], are given in Table 1. The laminates contain an even number of plies and align in 0° degree throughout the length of the specimens. In his analysis, Travesa [16] took the stiffness of cohesive elements is as 10^6 N/(mm)^3, normal strength of cohesive elements is taken as 80 MPa, and shear strength of cohesive elements is taken as 100 MPa. The specimens modeled are 102-mm-long, 25.4-mm-wide, with two 1.56-mm-thick arms. Models used by Travesa [16] have 150 cohesive elements along the length of the specimens and at the middle section of the laminate, and 4 cohesive elements along the width. Initial delamination is 32.9 mm for the DCB specimens and 39.2 mm for the ENF specimens at the beginning and the middle section of the specimens. In the present study, firstly, composite layups are modelled with 8-node brick elements C3D8 in ABAQUS. With the C3D8 elements convergence problem is encountered in the finite element analyses. To overcome the convergence problem, composite layups are modelled with 8-node

23

linear brick, incompatible mode elements C3D8I in ABAQUS. It should be noted that incompatible mode elements use full integration in finite element analysis and improve the bending behavior. Therefore, composite layups are modelled with 8-node linear brick, incompatible mode elements (C3D8I) and the cohesive layer is modelled with 8-node three-dimensional cohesive elements (COH3D8). In the finite element models, global element size is taken as 5 mm and the cohesive element size is taken as 0.5 mm. This is enough resolution for the verification because the cohesive element size smaller than 0.5 mm has true results, too but there is a huge increment in the computation time for the analysis. The material properties of the composite ply are given in Table 1, and boundary conditions for the DCB and the ENF specimens are displayed in Figure 11 and Figure 12 [16].

Table 1: Ply properties of the DCB and ENF specimens [16]

E_{11}	$E_{22}=E_{33}$	$G_{12}=G_{13}$	G_{23}	$v_{12}=v_{13}$	V_{23}	G_{Ic}	G_{IIc}	The B-K Parameter
122.7 GPa	10.1 GPa	5.5 GPa	3.7 GPa	0.25	0.45	0.969 kJ/m^2	1.179 kJ/m^2	2.284

In ABAQUS, the step procedure of the delamination analysis is selected as dynamic-implicit step because of the convergence that it provides in 3D implicit analyses. The other step procedures are static general step with default definition and static general step with automatic stabilization definition. It is noted that the analysis results do not match the results of Travesa [16] if static general steps are used. The experimental data and numerical predictions of Travesa [16] and present analysis results with three step procedures for the DCB specimen are shown in Figure 13. In the static general step with automatic stabilization definition, the loss of stiffness occurs before the damage starts. In the static general step with default definition, analysis does not converge and stops at damage initiation, so the damage evolution cannot be observed. It can be seen that the step procedure dynamic-implicit step with quasi-static application predicts the damage initiation and progression properly and in accordance with the results of Travesa [16]. It should be noted that there is a difference between the results of the present analysis and the results of Travesa [16] because of the type and formulation of the cohesive elements used in the present

analysis and used by Travesa. In the present analysis, cohesive elements defined in the finite element code ABAQUS are used. However, in the study of Travesa, the cohesive elements were implemented using a user-written subroutine in the finite element code ABAQUS [16]. The cohesive elements in both study are 8-node elements and these nodes can be used to connect three-dimensional elements with three degrees of freedom per node [16]. Cohesive elements used in Travesa's study [16] are zero-thickness elements while the cohesive elements used in the present study are not zero-thickness elements and they have a predefined thickness. In the results presented in this chapter, experimental results are the test results of Travesa's study [16], numerical results are the finite element analysis results of Travesa's study [16], and the present analysis represent the finite element analysis results obtained in the present study.
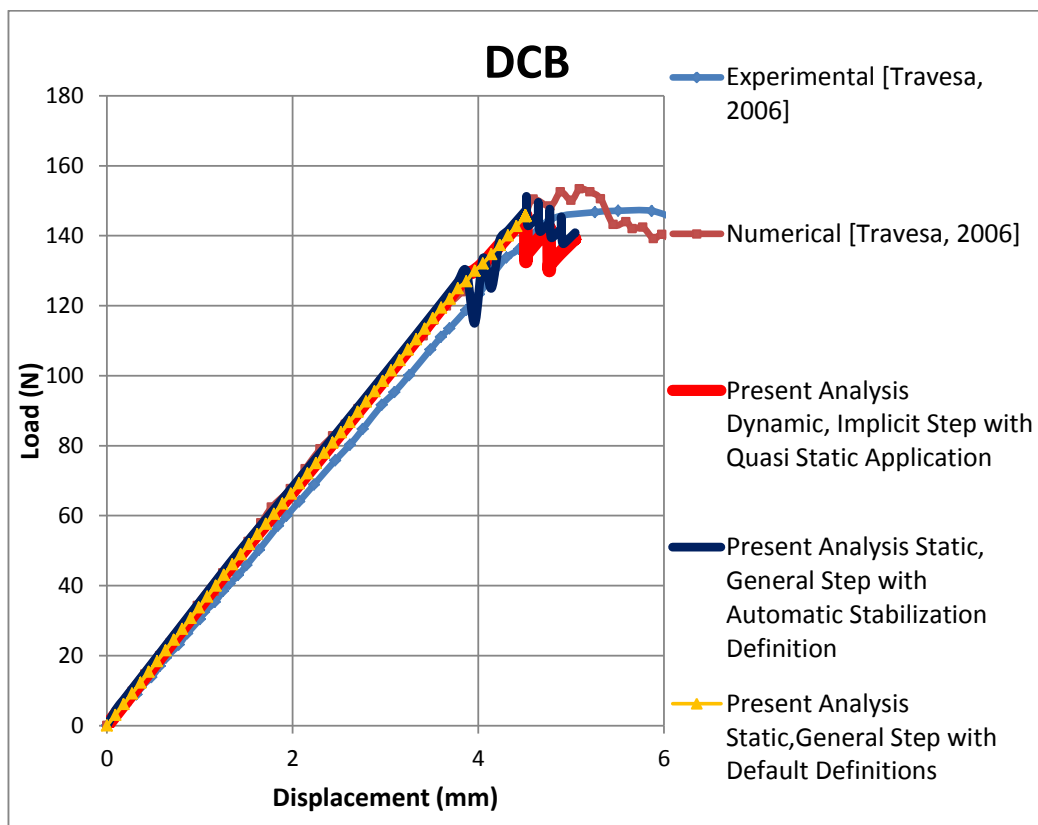
Figure 13: Experimental, numerical and analysis results with different step procedures for pure mode I loading

25

The experimental data and numerical predictions of Travesa's study [16] and the present analysis results are shown in Figure 14 and Figure 15 for the DCB and the ENF specimens. In both figures load-displacement curves are plotted. It is seen that present analysis results are compatible with the experimental and numerical results of the paper [16].
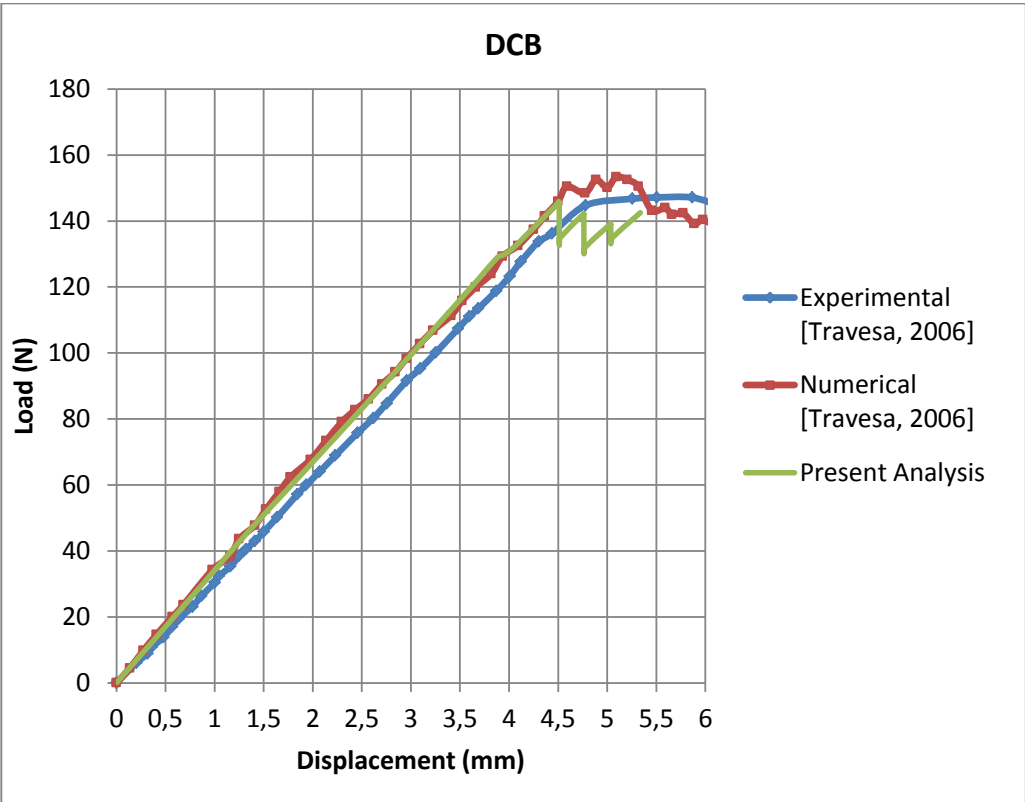
Figure 14: Experimental, numerical and analysis results –pure mode I loading
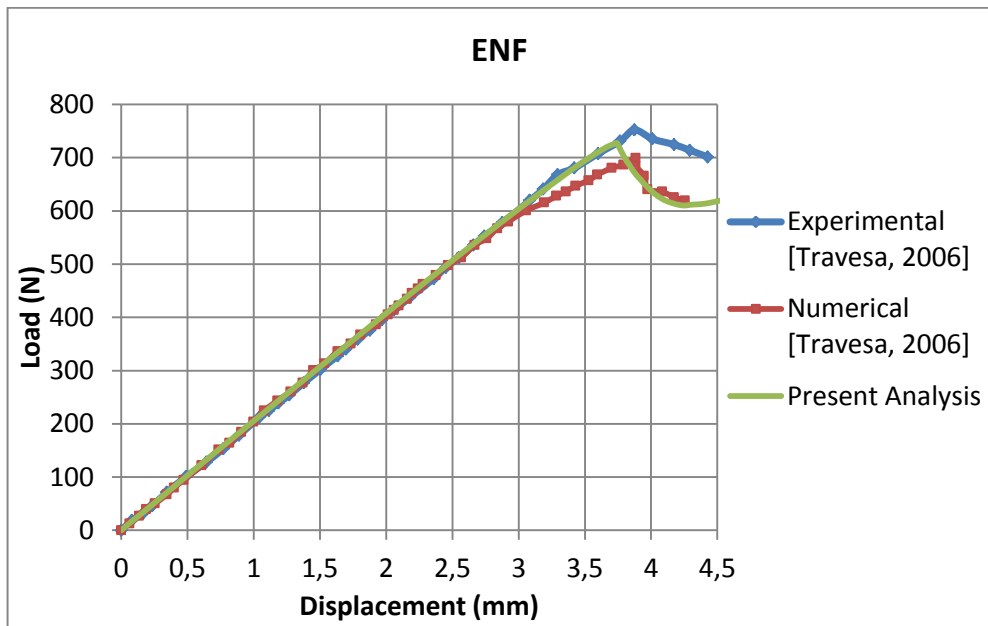
Figure 15: Experimental, numerical and analysis results –pure mode II loading

Damage initiation and propagation for the DCB and the ENF specimens are shown in Figure 16-Figure 19 which show the scalar stiffness degradation plots at the delamination interface which is at the mid plane. In these plots, if scalar stiffness degradation is equal to 1, it means that the cohesive element is not active and layers are fully separated and if scalar stiffness degradation is equal to 0, the cohesive element is fully active. In the analysis simulation of the ENF, the delamination starts and propagates as expected. From Figure 19. it can be seen that the cohesive elements at the start of the crack are not deleted and they still show up. The reason for this could be due to a bug in the post-processing in ABAQUS or the cohesive elements at the start of the crack might be highly distorted and because of the highly distorted elements, in the post-processing these elements may still show up.
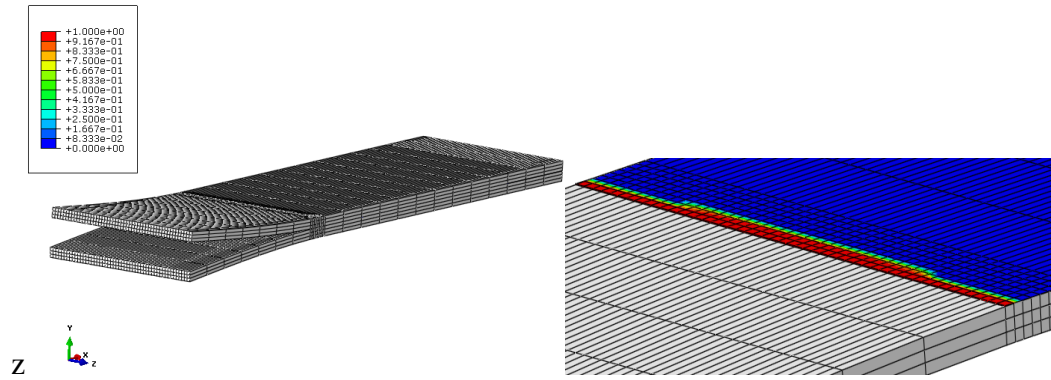
Figure 16: Delamination initiation in the DCB specimen
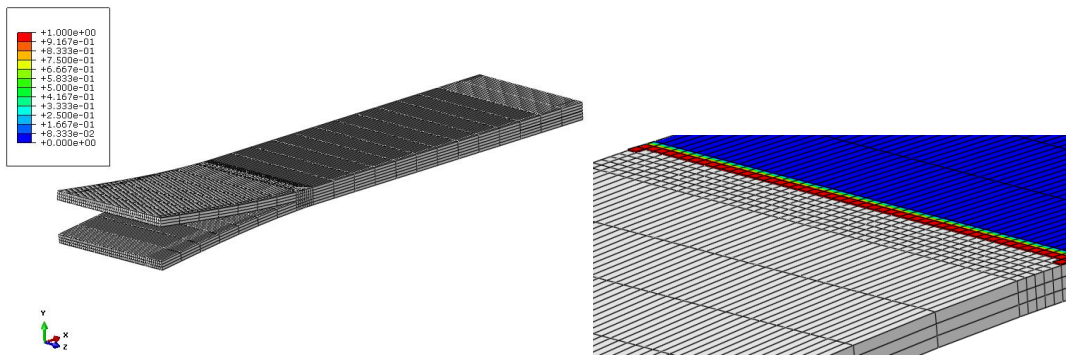
Figure 17: Delamination propagation in the DCB specimen
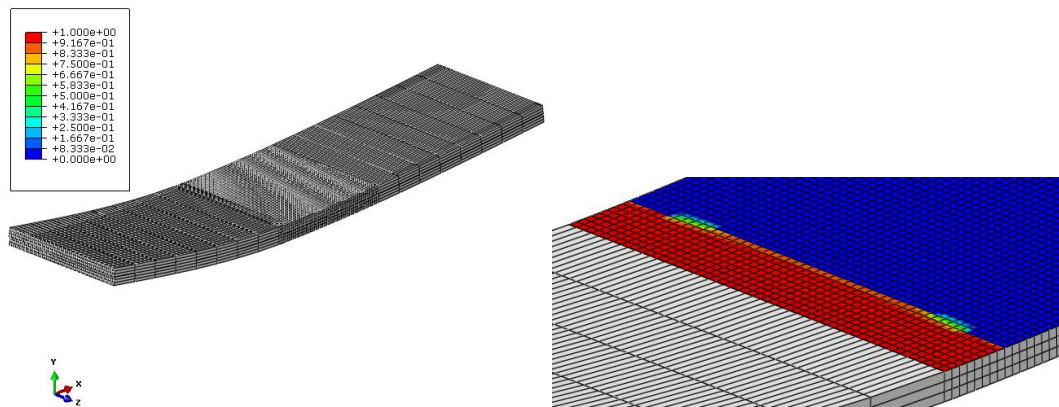
Figure 18: Delamination initiation in the ENF specimen

28
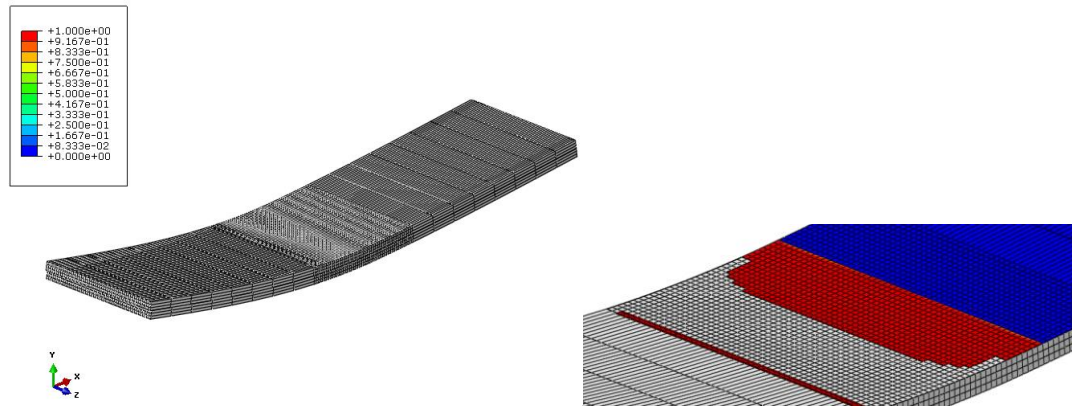
Figure 19: Delamination propagation in the ENF specimen

3.2. Effective Parameters for CZM

In this section parametric study is conducted to investigate the effect of certain parameters involved in the delamination analysis on the damage behavior. These parameters are selected as the normal mode fracture energy (G_{IC}) and the shear mode fracture energy (G_{IIC}), stiffness of cohesive elements (K) and element sizes (global element size-GES and cohesive element size-CES). In the literature, the effect of interfacial parameters, such as the initial interface stiffness and strength, the viscosity of cohesive elements and the number of cohesive elements (mesh size) in the cohesive zone on the delamination behavior in DCB and ENF specimens are discussed [35] [36]. A parametric study is required because stiffness of cohesive elements and element size must be chosen properly for correct finite element analysis. On the other hand, critical strain energy release rates G_{IC} and G_{IIC} are usually measured by DCB and ENF tests. In DCB and ENF tests, wide scatter of the test data is very common. Therefore, the effect of variation of the critical strain energy release rate about the nominal values on the delamination initiation and progression has to be investigated. Critical fracture energy or critical strain energy release rate, G_{IC} (normal mode fracture energy) and G_{IIC} (shear mode fracture energy) are two most important parameters which have to be correctly estimated or measured. Strain energy release rate governs the amount of the energy release if a crack growth occurs in surface-bonded structures [37]. The nominal values of G_{IC} and G_{IIC} are taken as 0.969 kJ/m^2 and 1.719 kJ/m^2 in Travesa [16]. Additionally, a

higher and a lower value for the critical strain energy release rates are used in the following analyses to see their effect on delamination initiation and progression.

Figure 20 and Figure 21 show the effect of critical strain energy release rates on the delamination initiation and progression for DCB and ENF specimens. These figures show that the delamination starts at higher loads if the values of G_{IC} and G_{IIC} are higher than the nominal values and delamination starts at lower loads if the values of G_{IC} and G_{IIC} are lower than the nominal values, as expected.
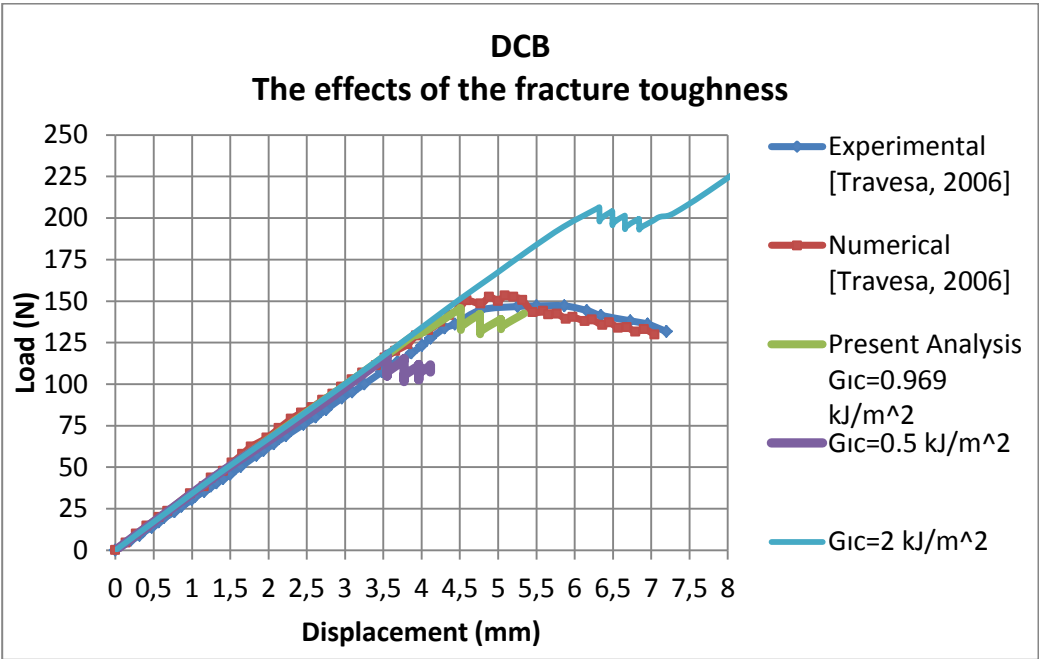
Figure 20: Experimental, numerical and analysis results for the DCB specimen– the effect of the critical energy release rate, G_{IC} on the delamination behavior
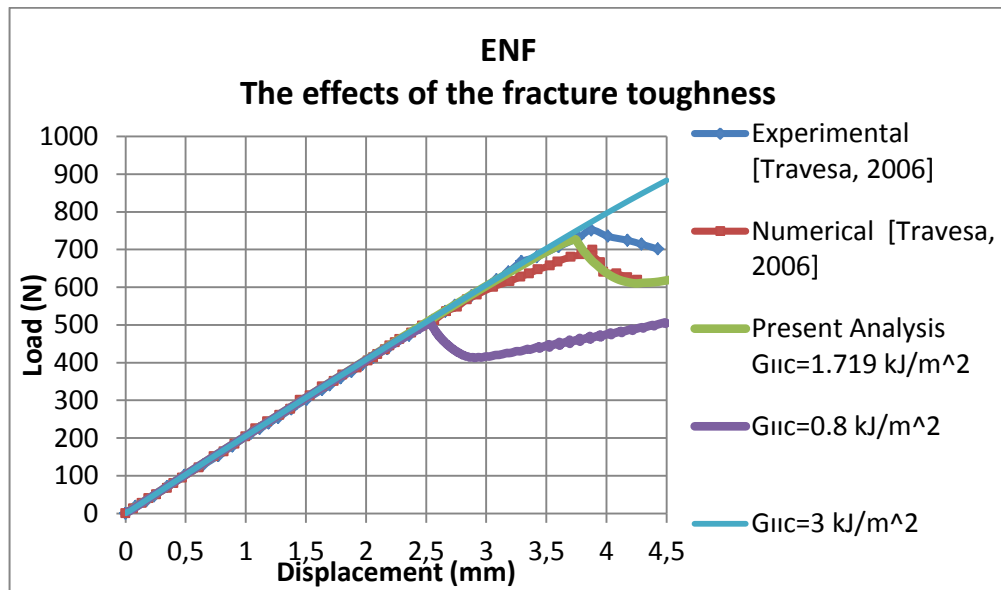
Figure 21: Experimental, numerical and analysis results for the ENF specimen – the effect of the critical energy release rate, G_{IIC} on the delamination behavior

The other important parameter in the delamination analysis is the stiffness of cohesive elements or the penalty stiffness, K. The initial stiffness of the cohesive elements should be high enough to provide the general compliance before the damage starts [38].

The stiffness of cohesive elements or the interface stiffness or the penalty stiffness, K, is the slope of the initial linear region of the constitutive equation before damage initiation as shown in Figure 22. The effective elastic properties of the composite are affected by the cohesive surface whenever $E_{33} << K\,t$ [36].

$$K \geq \alpha E_{33} / t \qquad\qquad\qquad (3.1)$$

where t is the thickness of composite layups (adjacent sub-laminates) and α is a parameter much larger than 1 and it is recommended that α should be chosen as 50 [36]. In this study, the penalty stiffness is determined as $K \approx 300000$ N/mm^3 utilizing Equation 4.1. Therefore, the values higher than 300000 should be used for the

31

penalty stiffness K. Travesa, in his study, took the stiffness of cohesive elements is as 10^6 N/mm^3 [16].
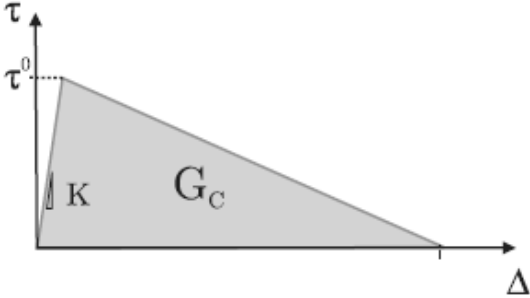
Figure 22: Bilinear constitutive equation [36]

Figure 23 and Figure 24 show the effect of penalty stiffness on the delamination initiation and progression for the DCB and the ENF specimens. As it is noted before, in the literature, penalty stiffness is generally chosen as 10^5 or 10^6 kJ/m. As long as the penalty stiffness is taken in the 10^5 - 10^6 kJ/m^2 range, the load–displacement curves are relatively insensitive to the penalty stiffness and interfacial strength, but very sensitive to the mesh size. If the value of penalty stiffness is chosen as an overly high value, numerical problems occur in analysis and damage starts early. On the other hand, damage cannot be observed thoroughly with an overly low value of penalty stiffness, as seen in Figure 23 and Figure 24.
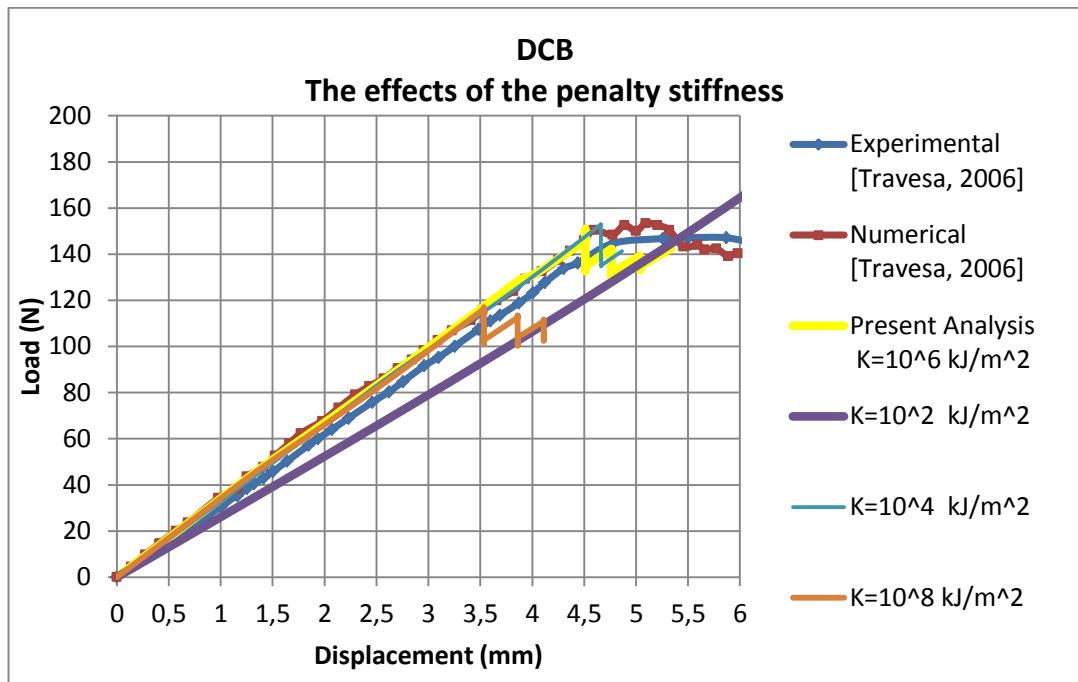
Figure 23: Experimental and numerical analysis results for the DCB specimen– the effect of stiffness of cohesive elements or the penalty stiffness, K on the delamination behavior
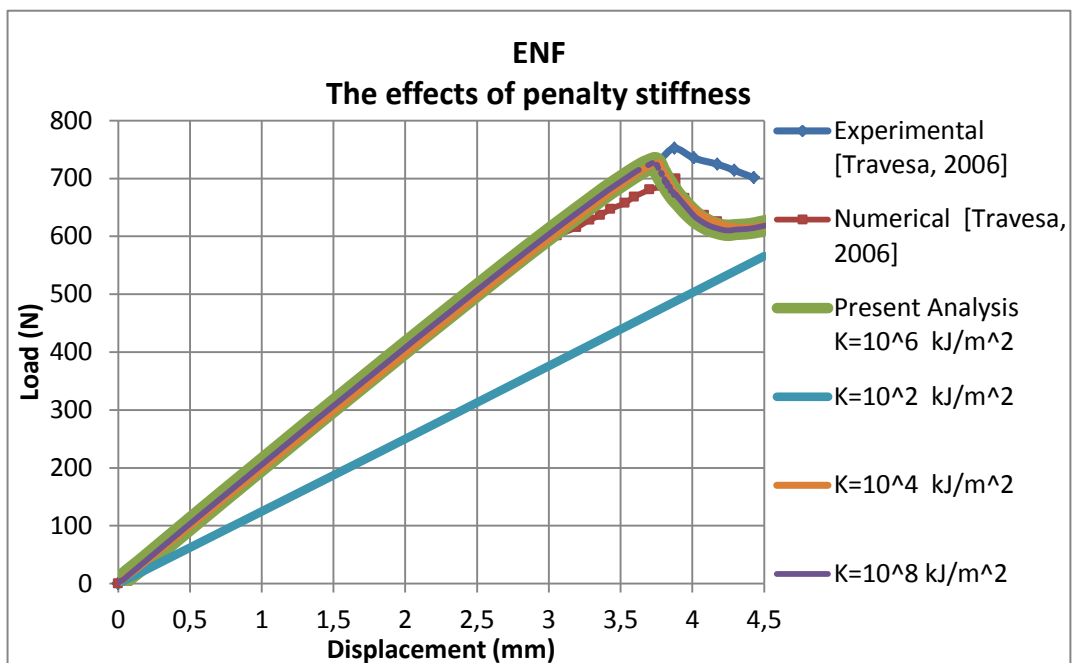
Figure 24: Experimental, numerical and analysis results for the ENF specimen– the effect of stiffness of cohesive elements or the penalty stiffness, K on the delamination behavior

One of the most critical parameter in the delamination analysis is the effect of global and cohesive element size on the delamination initiation and progression.

The experience in the literature is to use a cohesive element size of 0.5 mm or less for standard DCB and ENF specimens in order to predict the delamination initiation and progression accurately [39] [36]. In the literature analyses performed, with element sizes ranging between 0.125 mm and 5 mm, show that mesh size of cohesive elements must be lower or at least equal to 0.5 mm in order to get converged solutions [36] [40] [41] [42]. If the element size increases, the damage initiation starts at higher loads than expected damage initiation loads.

Figure 25 shows the effect of cohesive element size on the delamination initiation and progression for DCB specimens. Global element size-GES and cohesive element size-CES should have optimum values in order to have convergence in the finite element analysis of DCB specimens. If CES is chosen as a high value such as 1 mm, damage starts at higher loads. If CES is chosen as a very high value such as 5 mm, damage starts at lower loads and there is no damage progression until end of the loading, as show in Figure 25.
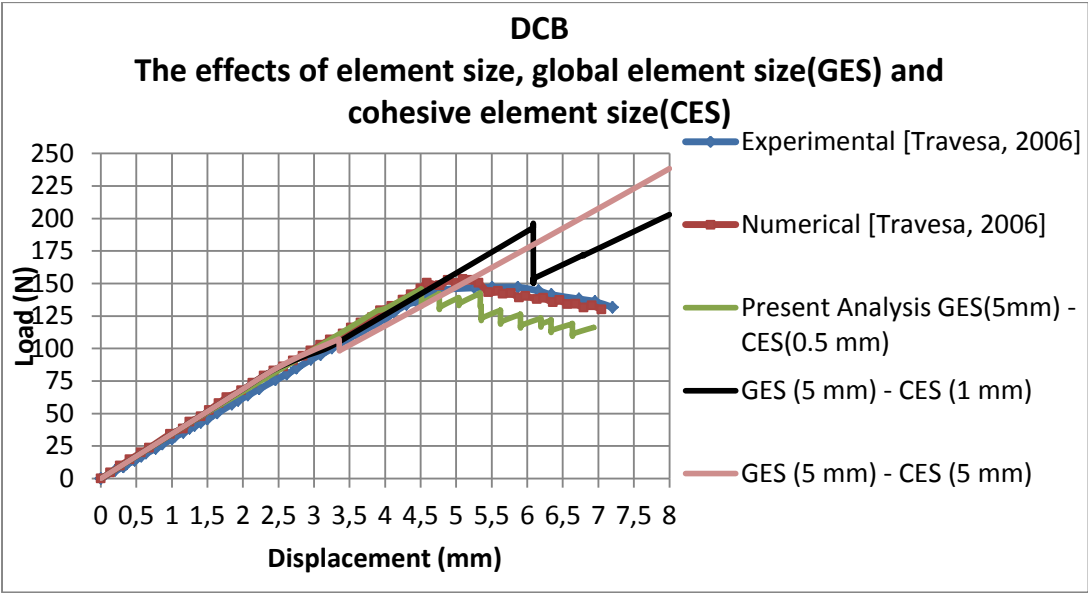
Figure 25: The effect of cohesive element size on the damage behavior for DCB specimens

34

Figure 26 shows the effect of global element size on the delamination initiation and progression for DCB specimens. As it is seen in Figure 26, if GES is chosen as low value such as 1 mm or 0.5 mm, damage initiation and propagation has correct behavior. However, it is not necessary to use very low GES because of the substantial increase in the computation time for the analysis. In addition, GES should not be very high because of good mesh quality and aspect ratio requirement in finite element analysis. In conclusion, global element size-GES and cohesive element size-CES should have optimum values in order to have convergence in finite element analysis of DCB specimens.
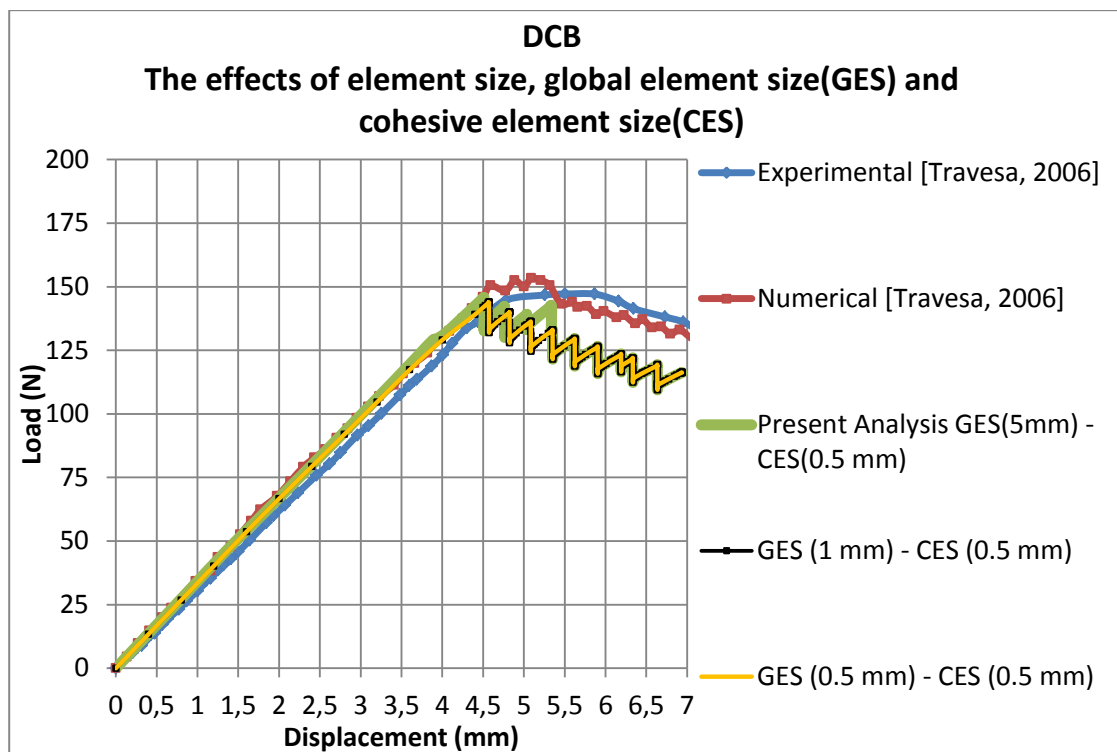
Figure 26: The effect of global element size on the damage behavior for DCB specimens

Figure 27 shows the effect of cohesive element size on the delamination initiation and progression for ENF specimens. Global element size-GES and cohesive element size-CES should have optimum values in order to have convergence in finite element

analysis of ENF specimens. If CES is chosen as a high value such as 1 mm, damage starts correctly but damage propagates with oscillations. If CES is chosen as a very high value such as 5 mm, damage starts at higher loads, as seen in Figure 27.
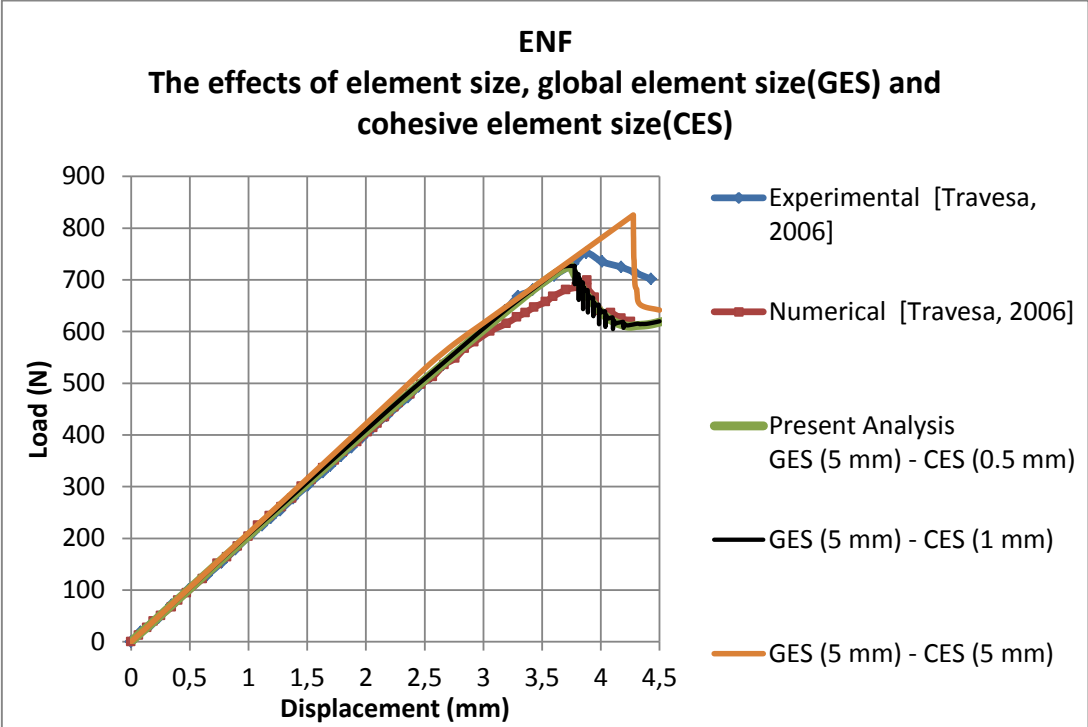
Figure 27: The effect of cohesive element size on the damage behavior for ENF specimens

Figure 28 shows the effect of global element size on the delamination initiation and progression for ENF specimens. Results of analysis of ENF specimens are similar with the results of DCB specimens on the effect of global element size on the delamination behavior. If GES is chosen as a low value such as 1 mm or 0.5 mm, damage initiation and propagation has correct behavior. However, as in the DCB specimens, it is not necessary to use very low GES because of the substantial increase in the computation time for the analysis. Otherwise, GES should not be very high because of good mesh quality and aspect ratio requirement in finite element analysis. In conclusion, global element size-GES and cohesive element size-CES

36

should have optimum values in order to have convergence in finite element analysis of ENF specimens.
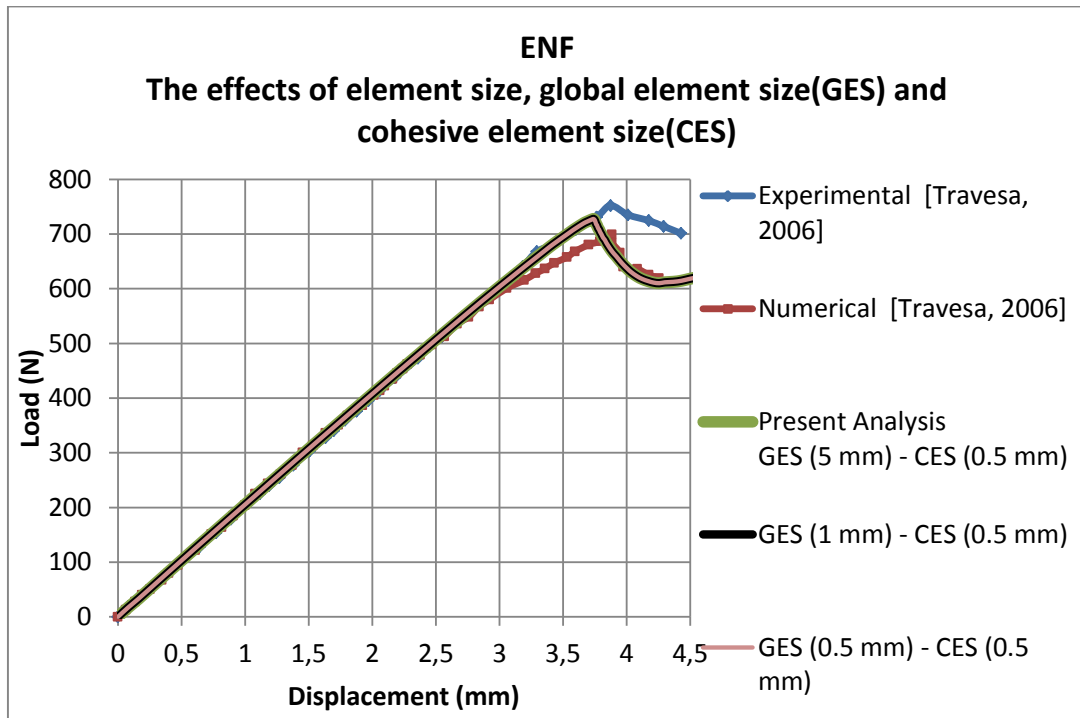
Figure 28: The effect of global element size on the damage behavior for ENF specimens

In summary, in this section parametric study is performed for Double Cantilever Beam (DCB) and End Notch Flexure (ENF) specimens with cohesive zone method (CZM) to model the delamination initiation and propagation. For verification purposes, results of the delamination analyses for Double Cantilever Beam (DCB) and End Notch Flexure (ENF) specimens are compared with the experimental and numerical results available in the literature. In this study, dynamic-implicit step with quasi-static application step procedure is used in conjunction with 3D global and cohesive finite elements in order to perform the delamination analysis by implicit finite element analysis. The analysis results are seen to be compatible with the available experimental and the numerical results in the literature. The results of parametric study for the DCB and the ENF specimens are presented for variations in

the normal and shear mode fracture energy (G_{IC}, G_{IIC}), stiffness of cohesive elements (K) and global and cohesive element sizes. It is noted that fracture energies (G_{IC} and G_{IIC}) are generally determined by Mode I and Mode II tests. The present analysis showed that the use of lower or higher fracture energy than the nominal value caused under and over estimation of delamination initiation, respectively. It is also concluded that the penalty stiffness should not be low because with low penalty stiffness value delamination initiation cannot be predicted. In the literature, the recommended value of the penalty stiffness is in the range of 10^5 or 10^6 kJ/m^2. The analyses performed in the present study also confirm the suitability of this range. Finally, the size of cohesive elements must be 0.5 mm or less in order to predict the delamination onset and progression accurately for standard DCB and ENF specimens.

CHAPTER 4

4. ANALYSIS VERIFICATION of MODE I and MODE II TESTS

This chapter describes the test and analysis verification of the DCB and ENF tests performed to determine the fracture toughness data of the twill composite. The fracture toughness data of the carbon-epoxy twill composite material obtained from tests is then used in open hole tensile test simulations in Chapter 5 and wing bending analysis in Chapter 6.

4.1. Test and Analysis Results of Double Cantilever Beam (DCB) Specimens (Mode I) and End Notched Flexure (ENF) Specimens (Mode II)

In the present study, the architecture of the composite fabric is twill and its fracture toughness data is obtained from tests to be used in open hole tensile and wing bending analysis [43]. DCB and ENF specimens are manufactured by CES Advanced Composite & Defence Technologies Inc.. DCB and ENF specimens are tested with Mode I and Mode II loading in order to obtain interlaminar fracture toughnesses, G_{Ic} and G_{IIc}. In Figure 29, pictures taken during Mode I and Mode II tests are shown. Mode I test is performed based on ASTM D5528-13 "Standard Test Method for Mode I Interlaminar Fracture Toughness of Unidirectional Fiber-Reinforced Polymer Matrix Composites" and Mode II test is performed based on DIN-EN 6034 "Determination of interlaminar fracture toughness energy - Mode II - G[IIC]" [44] [45]. Detailed calculation procedure of G_{Ic} and G_{IIc} is explained in APPENDIX A.
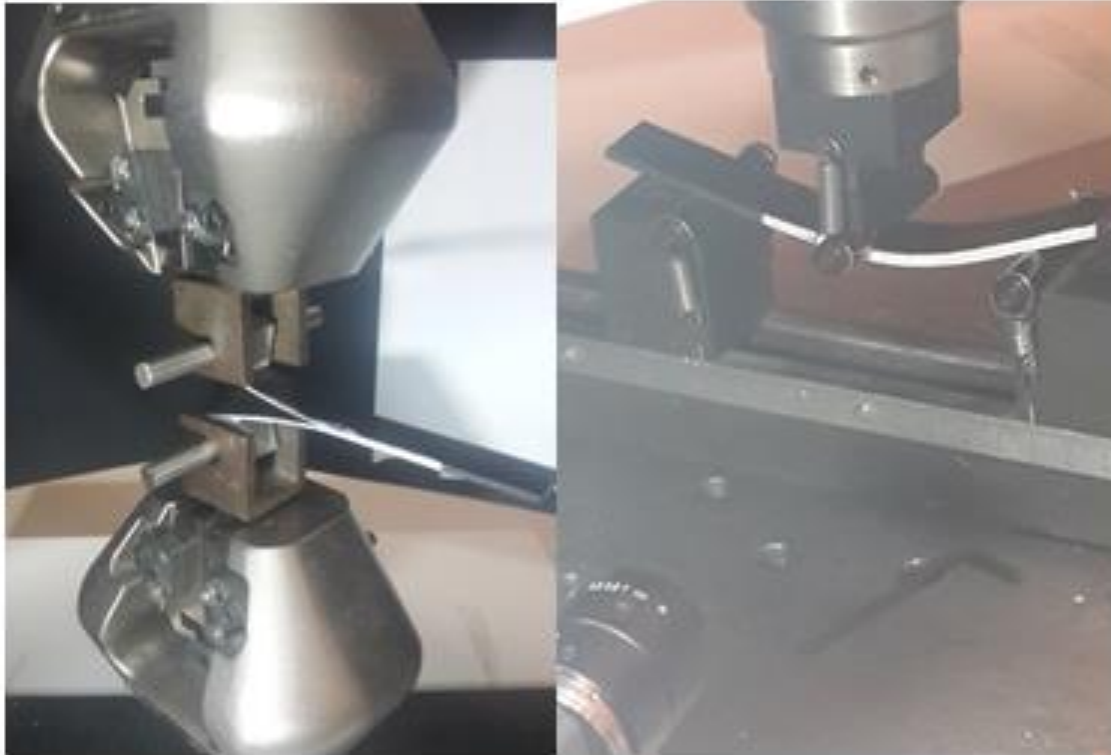
Figure 29: Mode I and Mode II tests

The DCB and ENF specimens are modelled in ABAQUS by using cohesive elements in the delamination interface to inspect the delamination initiation and propagation. The ply properties of deltapreg STE-DT121H-2 epoxy resin/T300-3K-2x2 twill prepreg composite is given in Table 1. The laminates contain an even number of plies and align in 0° degree throughout the length. In this study, the penalty stiffness is determined as K≈440000 N/(mm)^3 using Equation 4.1. Therefore, the values higher than 440000 should be used for the penalty stiffness K. Stiffness of cohesive elements is selected as 10^6 N/mm^3 considering the values used in the literature. In APPENDIX A, Mode I interlaminar fracture toughness is calculated as 0.469 kJ/m^2, and Mode II interlaminar fracture toughness is obtained as 1.516 kJ/m^2. Normal strength of cohesive elements is calculated as 55 MPa and shear strength of cohesive elements is calculated 50 MPa by verification of test and analysis results. Normal and shear strength of material is related with the start of the damage for DCB and ENF specimens. First, in the finite element results, load-displacement curves for DCB and ENF specimens are plotted. Then, normal and shear strength of material

are changed in analysis until this start point is same with the test results. Therefore, the normal and shear strengths used in FEA are changed until the maximum load at the analysis matches with the peak load at the present test. B-K parameter is selected as 2.284 in this study from Travesa [16] and this parameter is changed in some different values but the results of the analyses did not change.

The specimens modeled are 150-mm-long, 20-mm-wide, with two 1.45-mm-thick arms. In the finite element models, global element size is taken as 5 mm and the cohesive element size is taken as 0.5 mm for DCB and ENF specimens. Composite layups are modelled with 8-node linear brick, incompatible mode elements (C3D8I) and the cohesive layer is modelled with 8-node three-dimensional cohesive elements (COH3D8). The step procedure of the delamination analysis is selected as dynamic-implicit step because of the convergence that it provides in 3D implicit analyses. The twill material properties of the composite ply are given in Table 2.

The elastic moduli in wrap and fill directions ($E_{11} = E_{22}$) for twill material are obtained by tensile test. This test is based on ASTM D3039M - 14 "Standard Test Method for Tensile Properties of Polymer Matrix Composite Materials" [46]. The elastic moduli of the six specimens are obtained as 65525 MPa, 63043 MPa, 65484 MPa, 67218 MPa, 65150 MPa and 66463 MPa. The average value is given in Table 2.

Table 2: Ply properties of deltapreg STE-DT121H-2 epoxy resin/T300-3K-2x2 twill prepreg composite

$E_{11} = E_{22}$	E_{33}	G_{12}	$G_{13} = G_{23}$	v_{12}	$v_{13} = v_{23}$	G_{Ic} *	G_{IIc} *
65.3 GPa	12.8 GPa	6.065 GPa	2.8 GPa	0.03	0.45	0.469 kJ/m^2	1.516 kJ/m^2

*Fracture toughness values are obtained by experiments. Experimental results are presented in APPENDIX A.

DCB specimen is exposed to pure Mode I loading in opening mode. The location of the one loading block in DCB specimen is fixed in 3 displacement directions (Ux, Uy, Uz) and 2 rotation directions (URx, URy) in the region of the initial

delamination, as shown in Figure 30. The location of other loading block in DCB specimen is fixed in 3 displacement directions (Ux, Uz) and 2 rotation directions (URx, URy) at the initial delamination. The applied displacement at this location of the DCB specimen is 40 mm in +y direction in Figure 30. The reference points of the load and boundary conditions are coupled with the loading block surface in order to simulate the test condition as shown in Figure 30. The bending effect of the loading point at finite element model is explained in APPENDIX B.

ENF specimen is exposed to pure Mode II loading in sliding-shear mode. Rigid surfaces are defined at the ends and middle of the ENF specimen so as to simulate the test condition as shown in Figure 31. Rigid surfaces contact the ENF specimen at three locations as seen in Figure 31. Rigid surfaces at the ends of the specimen are fixed in 3 displacement directions (Ux, Uy, Uz) and 3 rotation directions (URx, URy, URz). The applied displacement to the ENF specimen is 14 mm at the middle rigid surface in the −y direction in Figure 31. Therefore, three point bending simulation is performed.

In this chapter, the boundary and load conditions are exactly similar with the test conditions. Therefore, the boundary and load conditions in the finite element models of these DCB and ENF specimens are different from the conditions in Chapter 3.
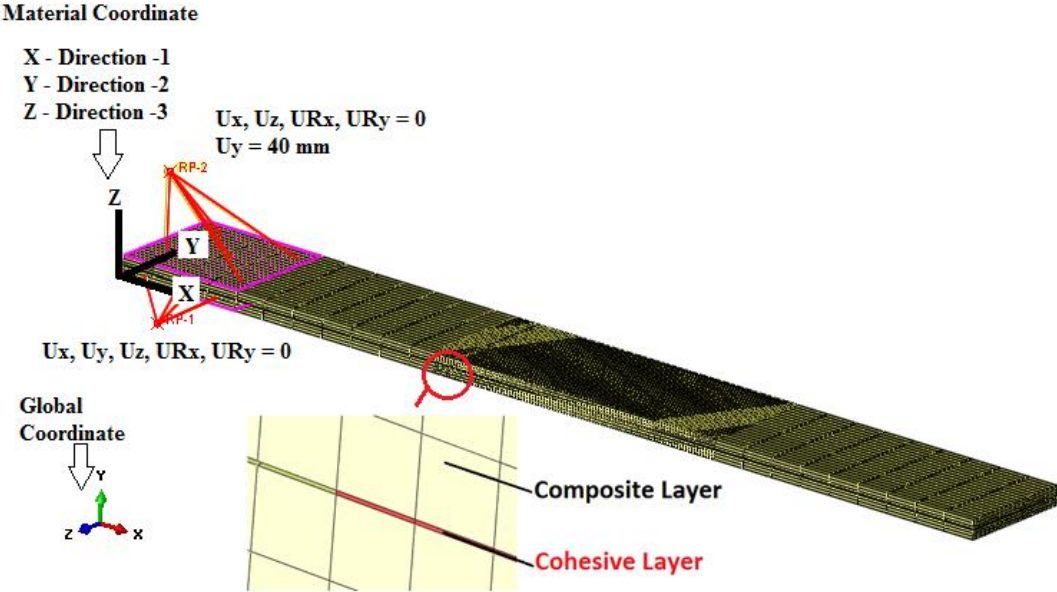
Figure 30: Finite element model of the DCB specimen

42
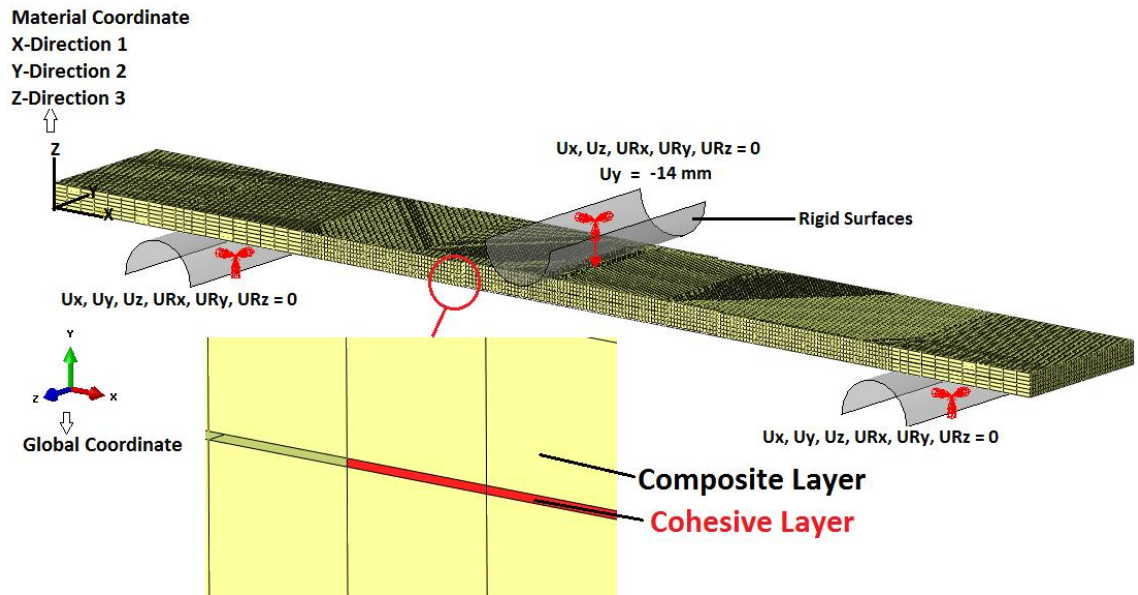
Figure 31: Finite element model of the ENF specimen

Figure 32 and Figure 33 show the comparison of experimental and analysis results for Mode I and Mode II loading simulation for the delamination initiation and progression. In Figure 32 and Figure 33, it can be seen that present analysis results are compatible with present experimental results for both Mode I and Mode II loading conditions.

The elastic moduli in wrap and fill directions ($E_{11}= E_{22}$) for the twill material are obtained as 65313 MPa (the twill material used by ODAK Composite Technologies Inc.) and 56700 MPa (the twill material used by CES Advanced Composite & Defence Technologies Inc.) by tensile test. In Figure 32, the results of the analyses with $E_{11}= E_{22}= 57600$ MPa is more compatible with the results of the present test of DCB specimen. The same elastic modulus is used for ENF specimens in FEAs. Also, $E_{11}= E_{22}= 57600$ MPa is used in order to obtain normal and shear strength of material is related with the start of the damage for DCB and ENF specimens.
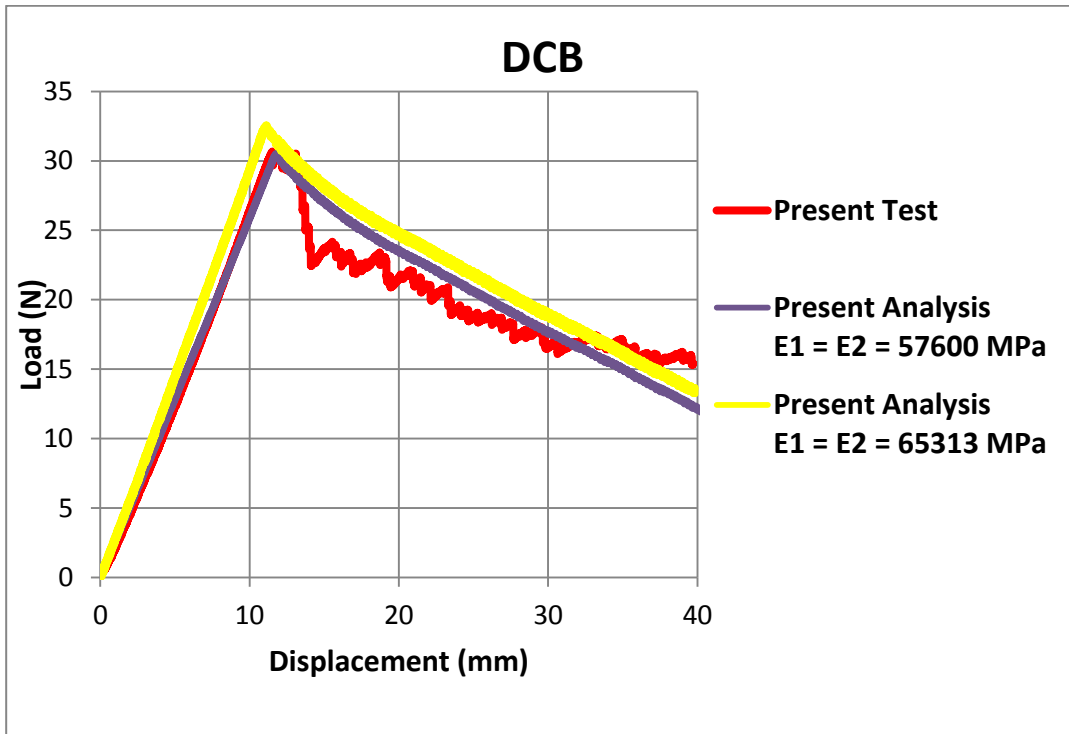
Figure 32: Experimental and analysis results –pure mode I loading
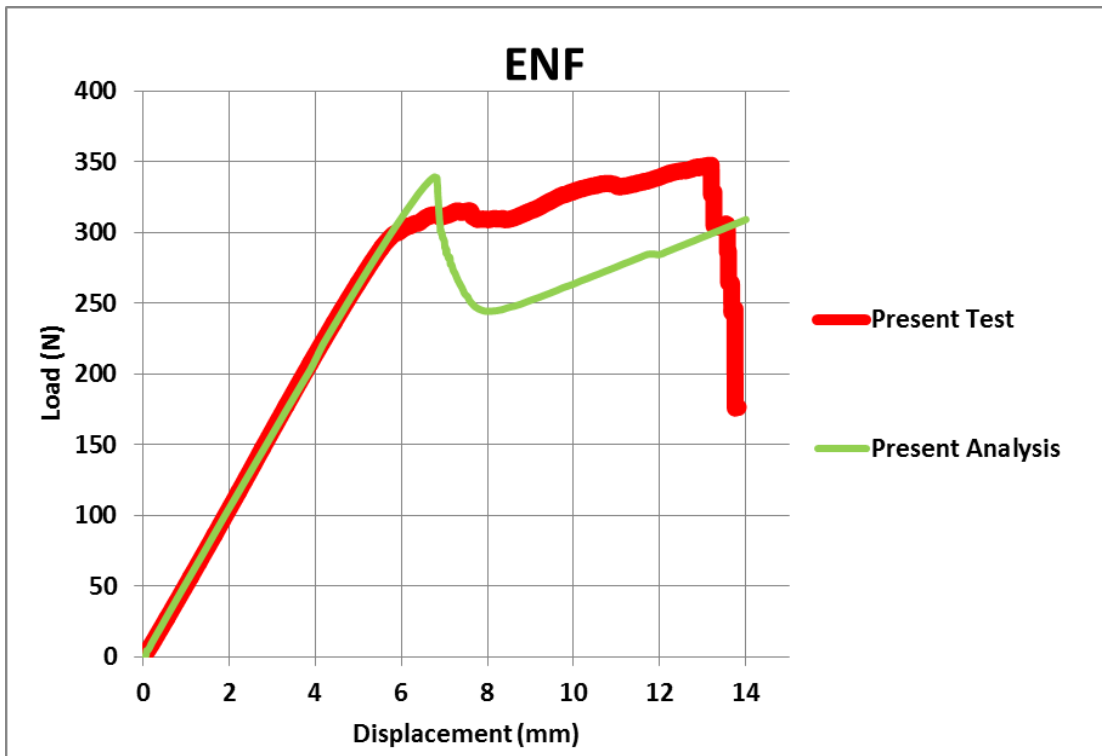
Figure 33: Experimental and analysis results –pure mode II loading

CHAPTER 5

5. ANALYSIS VERIFICATION of OPEN HOLE TESTS

In this chapter, after the completion of delamination initiation and propagation study for the DCB and the ENF specimens by finite element analysis, open hole tensile specimens which are manufactured by the same twill composite is tested in tensile loading condition. Intact (OHT) and delaminated (DOHT) open hole tensile specimens are tested in tensile loading and comparisons are made with the experimental results. Delamination progression test and analysis study is presented.

5.1. Test and Analysis Results of Open Hole Tension (OHT) and Delaminated Open Hole Tension (DOHT) Specimens

After the completion of delamination initiation and propagation study for the DCB and the ENF specimens by finite element analysis, open hole tensile specimens which are manufactured by the same twill composite is tested in tensile loading condition. The tensile strength of the open hole specimens is very important feature because the load carrying capacity is limited and the failure mechanics of plies are controlled by it for the composite structures [47]. In the literature, tensile strength of open-hole composites is studied by many researchers both numerically and experimentally [47] [48] [49] [11]. As in the present study, the tensile tests of open hole specimens manufactured by twill weave textile composite are used in order to verify the capability of a cohesive zone model for predicting the composite's strength in Xu's study [48].

In this study, Intact (OHT) and delaminated (DOHT) open hole tensile specimens are tested in tensile loading and comparisons are made with the experimental results. Both intact (OHT) and delaminated (DOHT) open hole tensile specimens are

manufactured by ODAK Composite Technologies Inc. so as to predict the delamination progression experimentally and to compare with the finite element analysis. Delaminated open hole tensile specimens are manufactured with the thin teflon film made of PTFE inserted in the pre-selected location. First, tests and analyses results of the OHT specimens are described in this chapter. The determination of the location of the PTFE film, tests and analyses results of the DOHT specimens are explained in detail later. The geometric dimensions and general view of OHT and DOHT specimens are given in Figure 34.
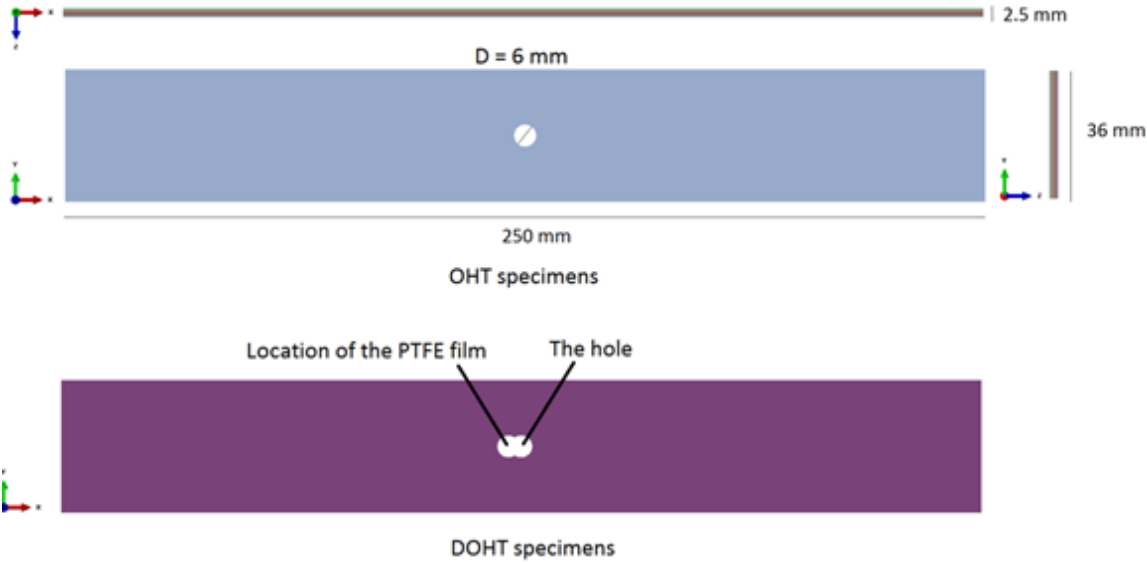
Figure 34: OHT and DOHT specimens

Tensile tests are performed based on "ASTM D5766/D5766M − 11- Standard Test Method for Open-Hole Tensile Strength of Polymer Matrix Composite Laminates" [50]. Tensile tests of open hole tensile specimens without the teflon film (OHT) and open hole tensile specimens with the film (DOHT) are performed. In addition to the load-displacement data, strain gauge and extensometer data are also obtained from the tests. Test machine (INSTRON electromechanical testing machine with 100 kN load cell capacity) used in the tensile tests of OHT and DOHT specimen is shown in Figure 35.
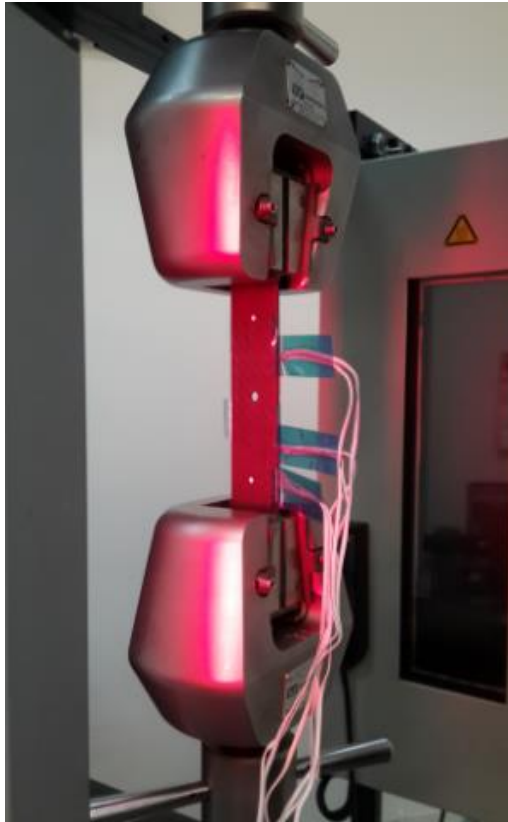
Figure 35: Tensile test of OHT and DOHT specimens

Intact open hole tension (OHT) specimens are 250-mm in length, 36-mm in width, 2.5-mm in thickness with 6mm diameter hole at the center of the plate. Tabs are 50-mm long and 2-mm in thickness. Laminate is symmetric and quasi-isotropic and stacking sequence is arranged as $[0^o/45^o]_{3s}$. The elastic moduli in wrap and fill directions ($E_{11}= E_{22}$) for twill material is taken as 65313 MPa for OHT and DOHT specimens Three strain gauges are placed on the specimen in order to obtain the strain data in the axial and transverse directions. Strain Gauge 1 and Strain Gauge 3 are biaxial gauges and Strain Gauge 2 is dual-axis gauge. Strain results in the transverse direction are not discussed in the chapter because of the discrepancy between the test and the finite element analysis results. It should also be noted that in the tensile test of open-hole composites, critical direction is the axial direction since the load is applied in the axial direction. Therefore, in the present study it is not tried to resolve the reason for the discrepancy between the transverse direction strains obtained by the tests and the finite element analysis. Figure 36 shows the OHT specimens with the strain gauges installed.
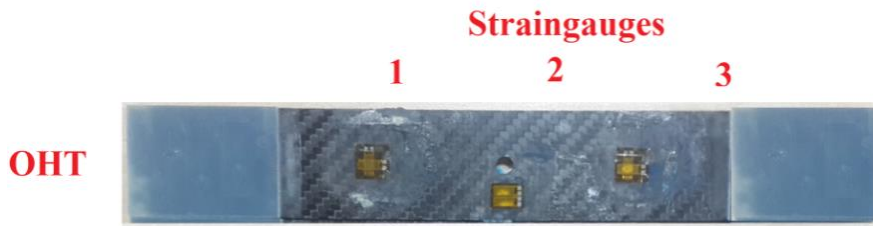
Figure 36: OHT specimens with strain gauges

5 OHT specimens are loaded in tensile tests and the maximum applied loads for the OHT specimens are given in Table 3. Considering the test results of five specimens, maximum failure load for the OHT specimens is obtained as 30330N.

Table 3: Maximum applied load for the OHT specimens

Specimen	Maximum Applied Load (N)
OHT-1	28613
OHT-2	29013
OHT-3	29014
OHT-4	29588
OHT-5	30330

Experimental and analysis results for the OHT specimens are plotted as load-displacement plot in Figure 37. It can be seen that present analysis results are compatible in the initial linear region with present experimental results for the OHT specimens. In the load-displacement curve of the present analysis for the OHT specimens, there is no sudden drop when the load reaches 30000 N, as shown in Figure 37. Because, in the results presented in Figure 37, failure criterion is not included in the finite element analysis of the OHT specimens, so there is no load drop. Present analysis is only performed to compare the stiffness of the OHT specimens in tests and analysis. Moreover, there is a slight difference between the load-displacement curves of the present analysis and tests for the OHT specimens. The slight difference between the test and analysis results is mainly attributed to the

slight error in the experimentally determined material constants which are supplied as input in the finite element analysis.
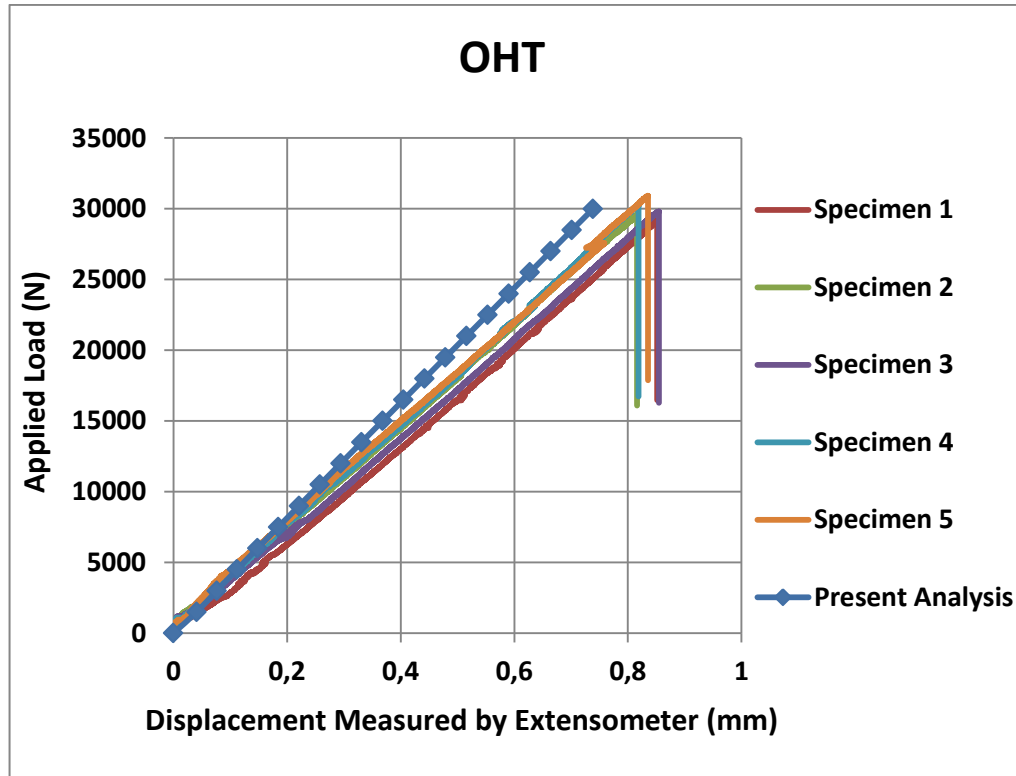
Figure 37: Experimental and analysis results/ Displacement vs Load / OHT

Load-strain data are given in Figure 38 and Figure 39 for the OHT specimens. It can be seen that present load-strain analysis and test results are compatible with present load-displacement analysis and test results for the OHT specimens. At the same load level, test displacement and strains are slightly higher than the displacement and strains determined by the finite element analysis of the OHT specimen.

In Figure 38, curves named as "s_NumberA_sg_NumberB" represent the experimental results. Five OHT specimens are tested and "NumberA" is the specimen number. Figure 36 shows the OHT specimens with the three strain gauges installed and "NumberB" is the strain gauge number. For example, "s_1_sg_3" represents the axial strain results of the Strain Gauge 3 on the Specimen 1. It should also be noted that the Strain Gauge 1 data for the Specimen 3 could not be collected during the experiments.
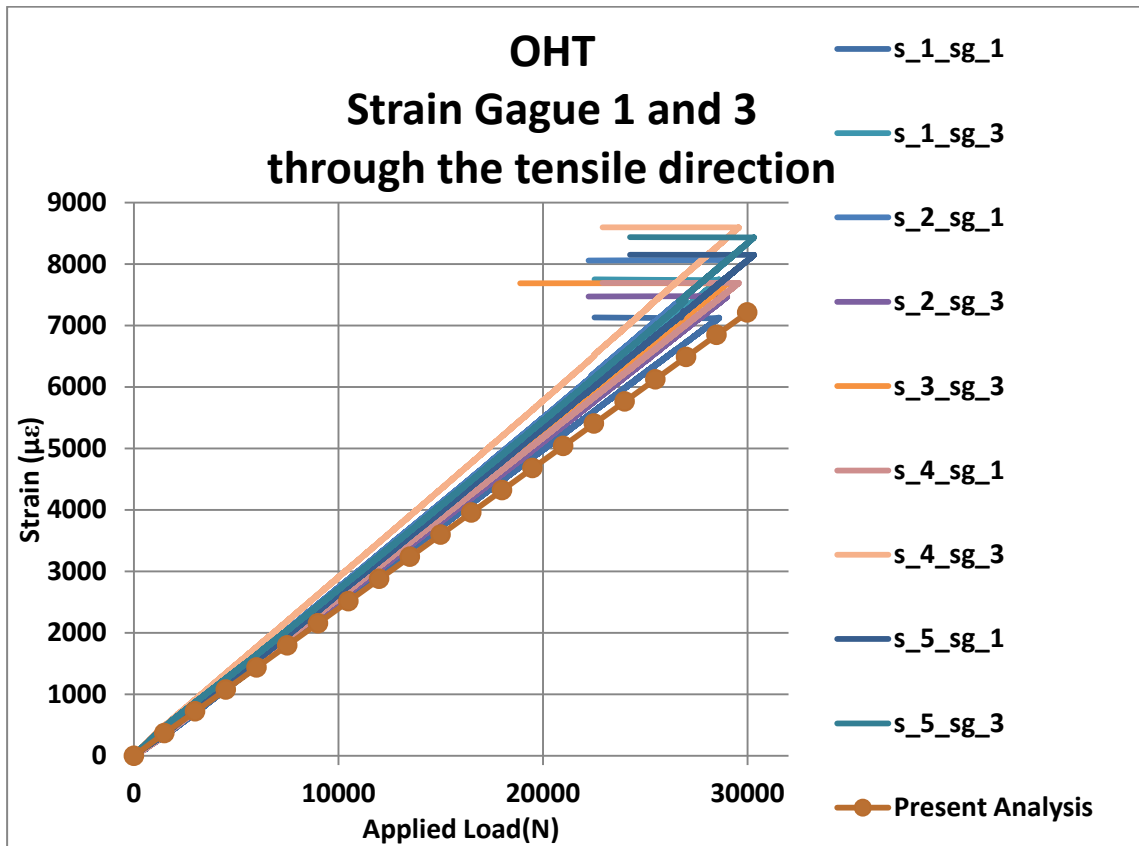
Figure 38: Experimental and analysis results – Load-Strain– OHT

Strain Gauge 1 and 3 in the axial tensile load direction.

In Figure 39, curves named as "s_NumberA_sg_NumberB_a" and "s_NumberA_sg_NumberB_b" represent the experimental results. "NumberA" and the "NumberB" have the same explanations as in Figure 38. Strain Gauge 2 is a dual gauge so there are two strain gauges in the same direction and they are denoted as "a" and "b" in Figure 39. Therefore, "s_1_sg_2_a" represents the axial strain results of the Strain Gauge 2 on the Specimen 1 and "s_1_sg_2_b" represents the other axial strain results of the Strain Gauge 2 on the Specimen 1. It should be noted that since the difference between strains in the dual strain gauge is very small, in the finite element analysis strain is calculated at the middle point of the dual strain gauge. It should also be noted that the strain gauge data for the Specimen 2 (a) and Specimen 3 (a and b) could not be collected during the experiments.
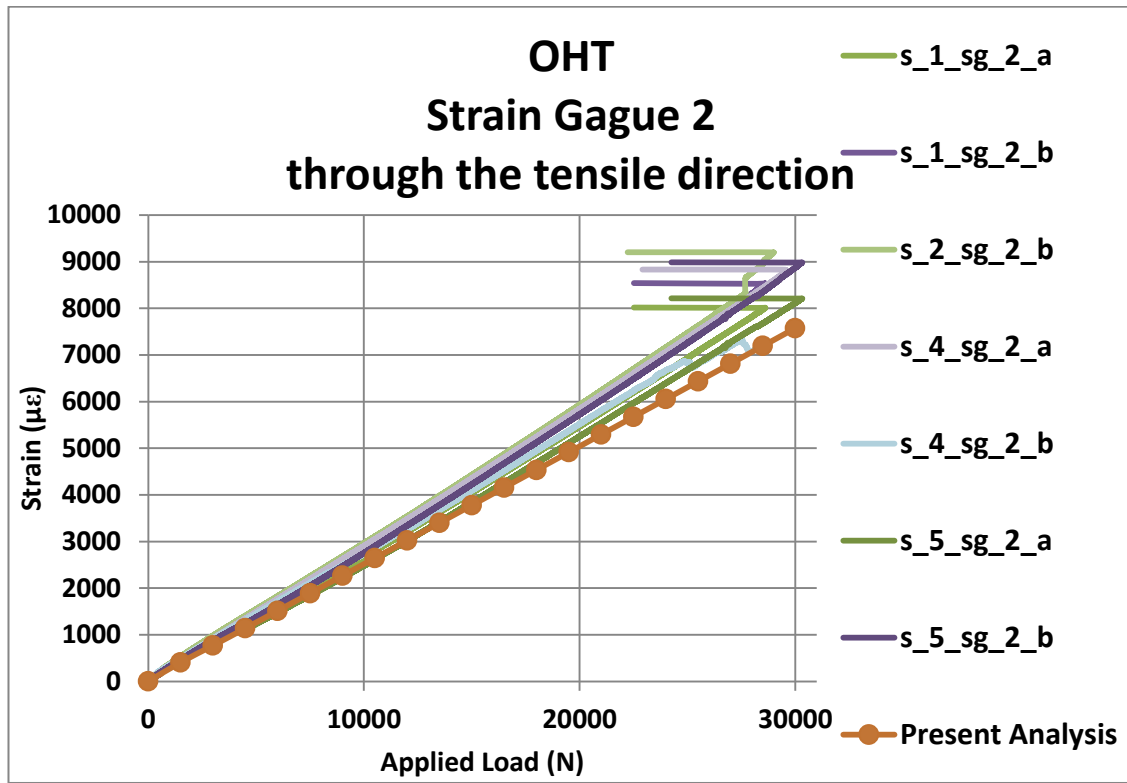
Figure 39: Experimental and analysis results / Load vs Strain gauge / OHT

Strain Gauge 2 in the axial tensile load direction

In the second set of analyses, finite element analyses of open hole tensile specimens without the film are performed for the tensile loading condition by including the ply failure criterion. The intralaminar failure region is predicted utilizing the failure criteria available in the literature. According to failure criteria, the location of the failure is predicted and analysis results are verified with tests for the OHT specimens. For this purpose, failure analysis results obtained with the Tsai-Wu, Tsai-Hill, maximum stress and Hashin failure criteria are compared in order to find the most appropriate criterion for the failure of the twill composite. Failure indices plots of all failure criteria at 30000N are shown in Figure 40-Figure 43.
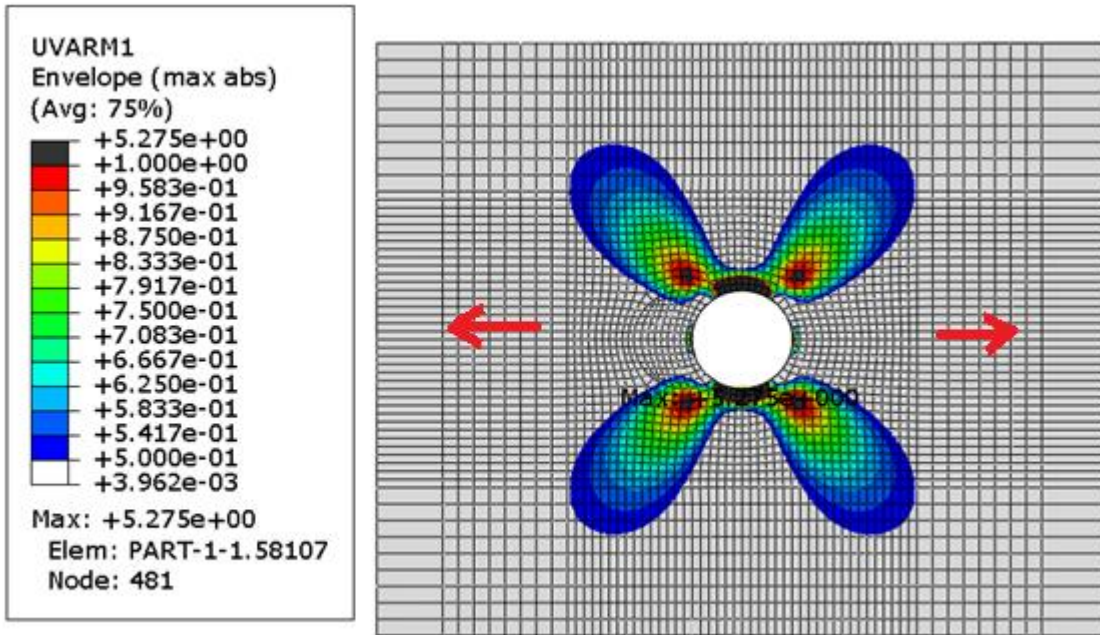
Figure 40: Failure Index Plot for the Tsai-Wu (UVARM1) failure criterion for the OHT specimen
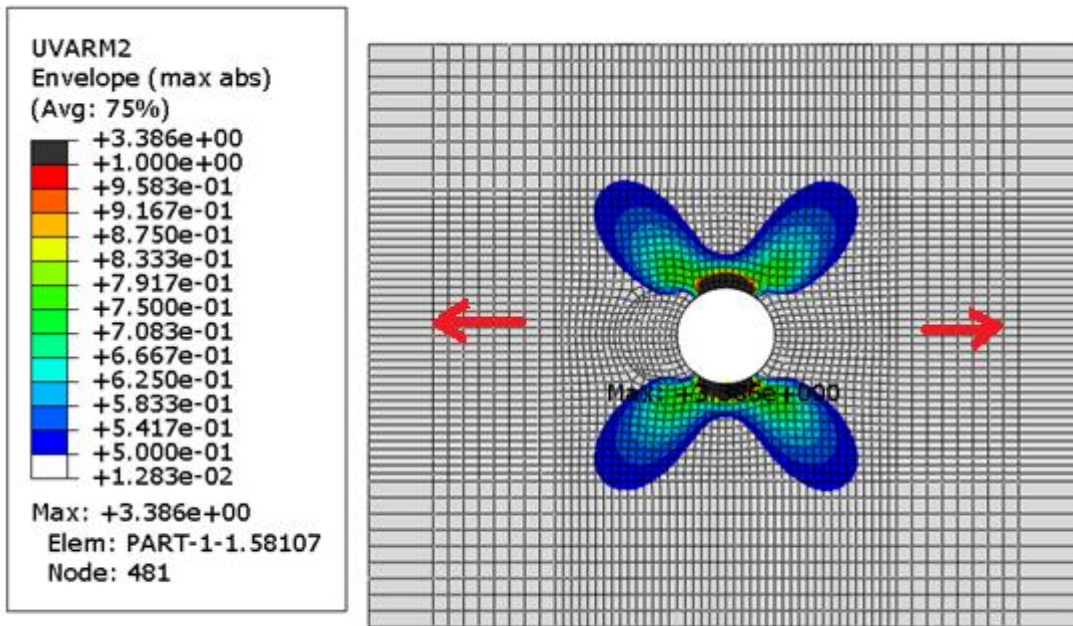
Figure 41: Failure Index Plot for the Tsai-Hill (UVARM2) failure criterion for the OHT specimen
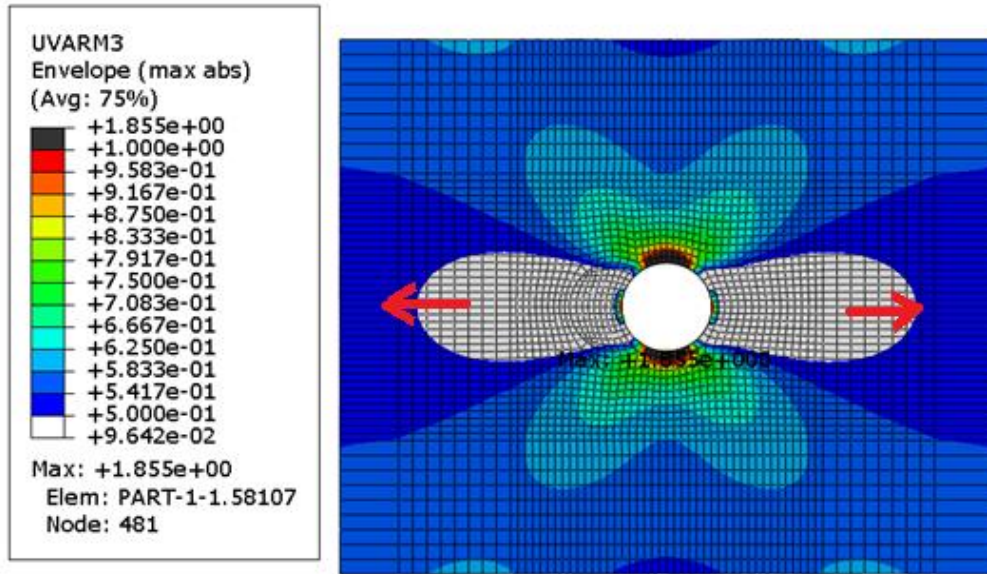
Figure 42: Failure Index Plot for the Max Stress (UVARM3) failure criterion for the
OHT specimen
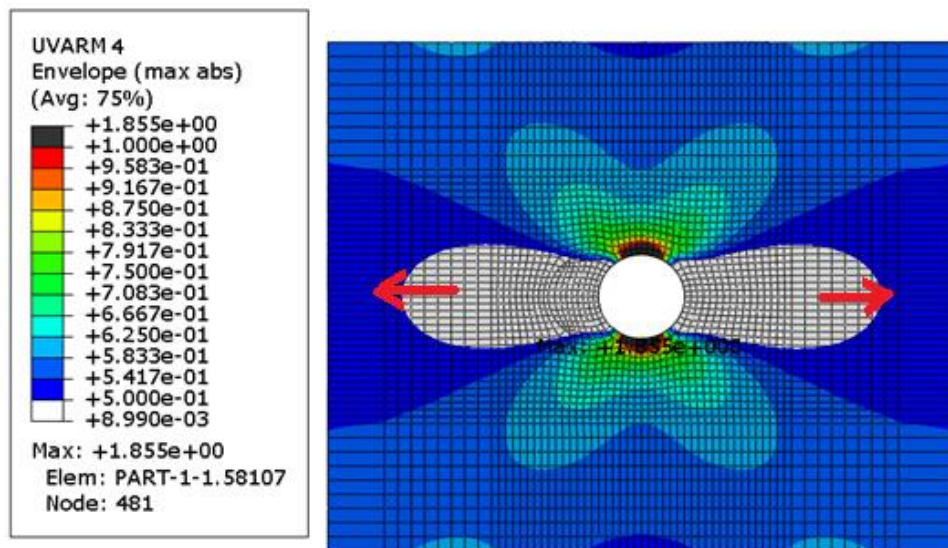
Figure 43: Failure Index Plot for the Hashin tensile fiber mode (UVARM4) failure
criterion for the OHT specimen

After the prediction of ply failure initiation location, finite element analyses of open
hole tensile specimens without the film are performed again at the same load
condition (30000 N) by degrading the stiffness of failed elements. Material property

degradation is performed such that failed elements lost all their load carrying capacity. Failure indices plots obtained by degrading the stiffness of failed elements for all failure criteria are shown in Figure 44-Figure 47. According to Tsai-Wu and Tsai-Hill failure indices plots, damage proceeds in 60^0 with respect to axis of the tensile loading for the OHT specimen. In the tensile tests of the OHT specimens, failure also occurs in 60^0 with respect to axis of tensile loading, as shown in Figure 48. Therefore, the most appropriate criterion for the failure of twill material is considered to as Tsai-Wu and/or Tsai-Hill failure criterion, as shown in Figure 49.
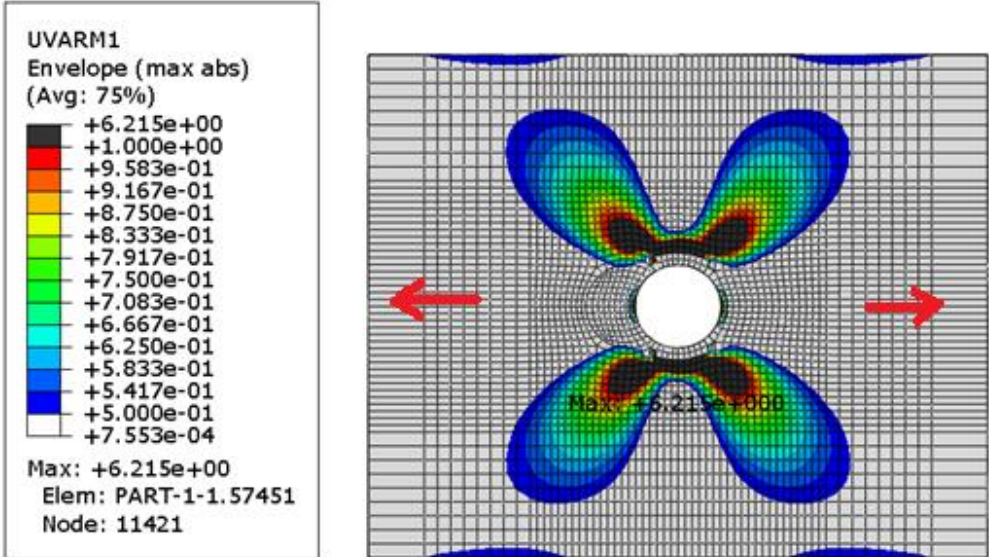
Figure 44: Failure Index Plot for the Tsai-Wu (UVARM1) failure criterion for the degraded OHT specimen
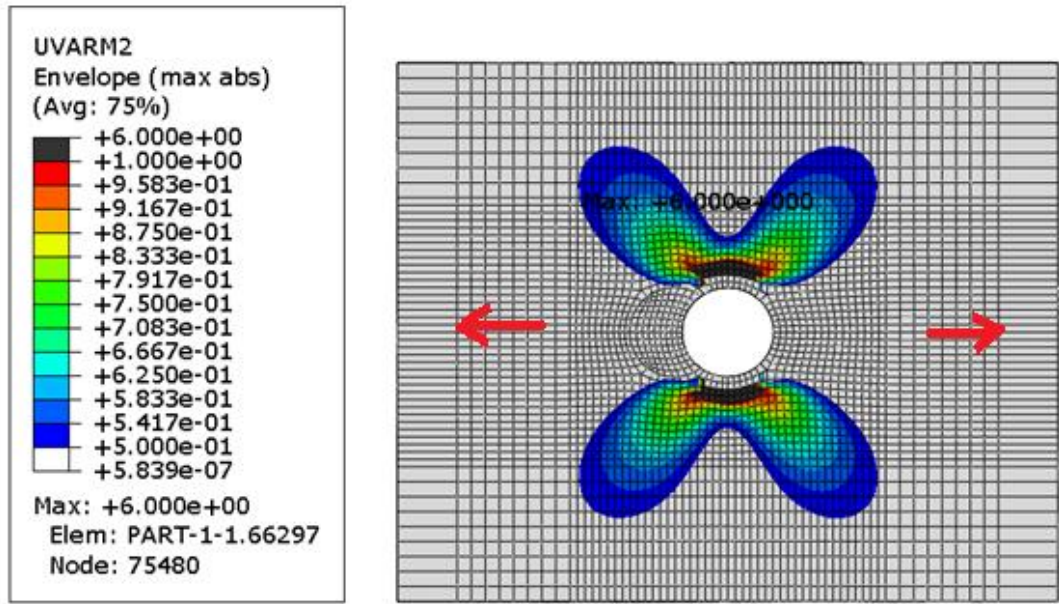
Figure 45: Failure Index Plot for the Tsai-Hill (UVARM2) failure criterion for the degraded OHT specimen
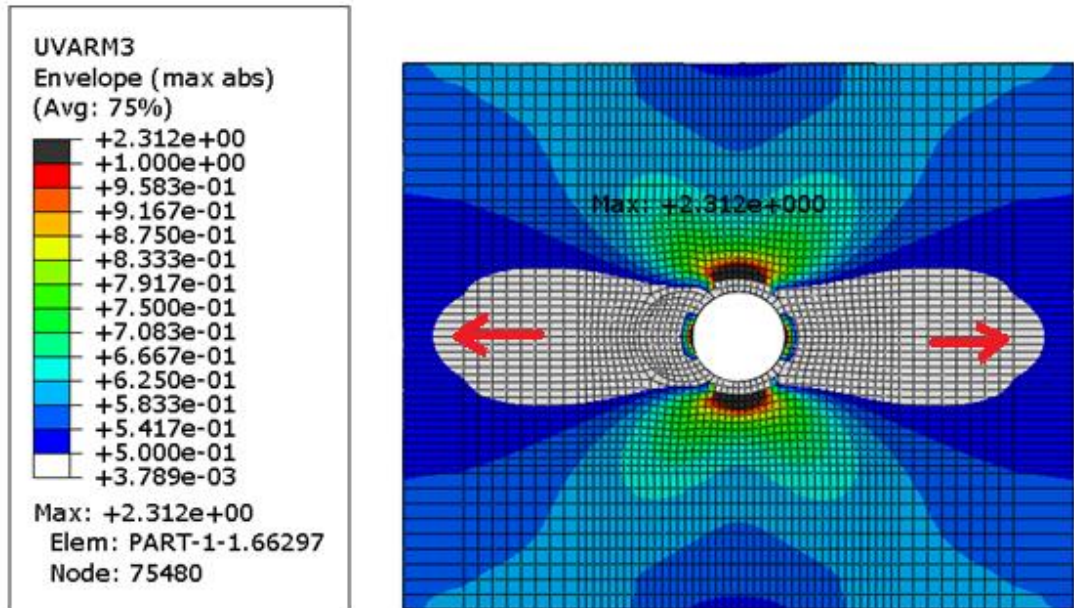
Figure 46: Failure Index Plot for the Max Stress (UVARM3) failure criterion for the degraded OHT specimen
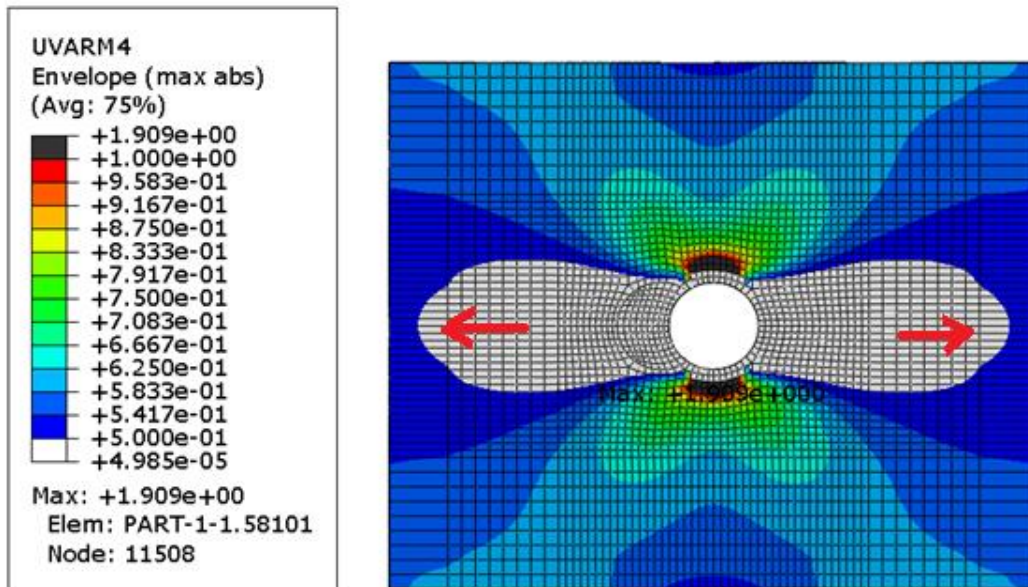
Figure 47: Failure Index Plot for the Hashin tensile fiber mode (UVARM4) failure criterion for the degraded OHT specimen
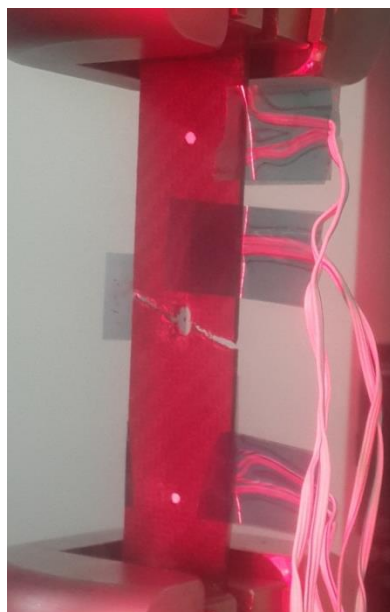
Figure 48: Failure of the OHT specimen during the tests
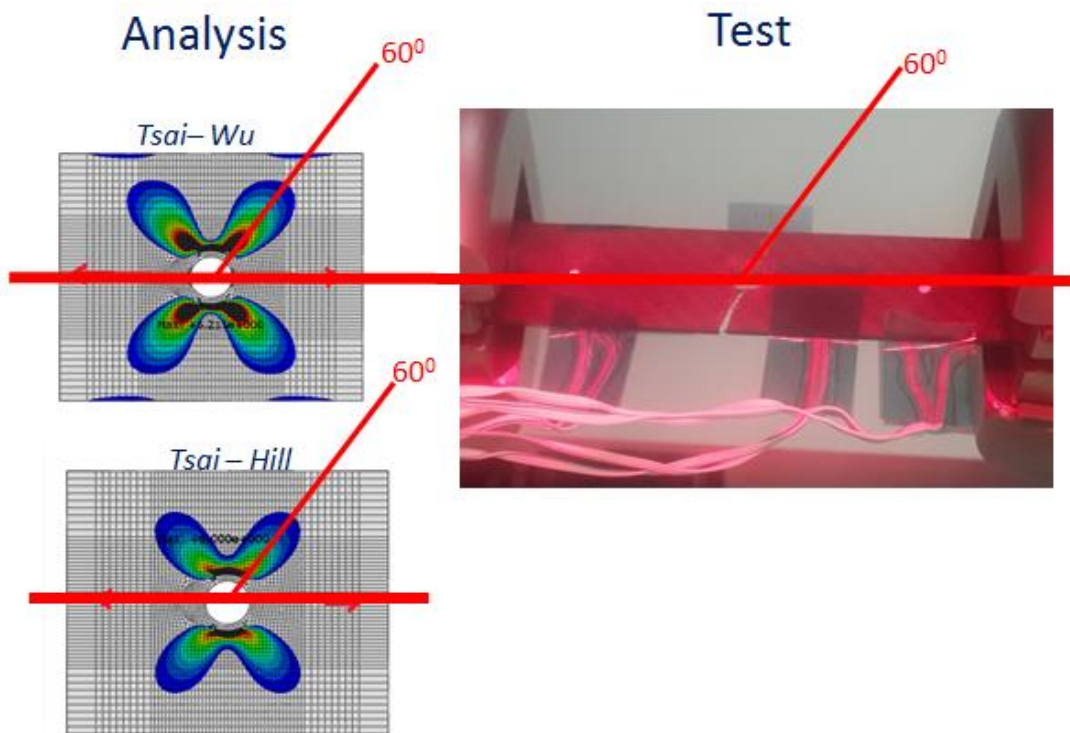
Figure 49: Failure of the OHT specimen during the analyses and the tests

Delaminated (DOHT) open hole tensile specimens have same dimensions with the intact OHT specimens. The diameter of the PTFE film is 6 mm and it is inserted between first and second ply in the DOHT specimens. Three strain gauges are placed on the specimen so as to obtain the strain data in the axial and transverse directions on the DOHT specimens. Figure 50 shows the DOHT specimens with strain gauges installed. The strain results of the transverse direction (strain gauge 3) are not discussed in this chapter because there is no acceptable difference between the analysis and the test results.
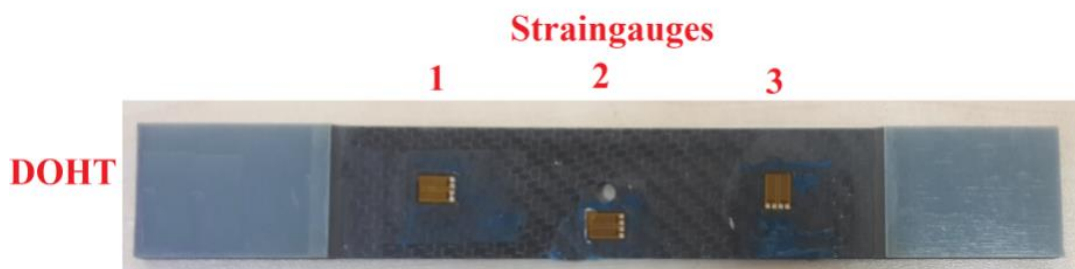
Figure 50: DOHT specimen with strain gauges

After performing finite element analysis of intact open hole test specimens without the film, pre-delamination analysis of the DOHT specimens without the teflon film is performed to predict the location of the delamination weak location. In the pre-delamination analysis, cohesive elements are modeled between all plies and ply failure is not considered. As shown in Figure 51, the maximum scalar stiffness degradation value is determined in a region which is approximately at 50°-60° with respect to the axis of tensile. In the composite wing test, presented the next chapter, PTFE film is decided to be inserted between the first and the second ply due to the higher stress caused by the bending load applied on the wing. To promote the delamination growth more easily, teflon film is inserted between the uppermost interface. To get prepared for the composite wing test and because of the ease of placing the teflon film between the first two plies, in the DOHT specimens, the PTFE film is also inserted between the first and the second ply.
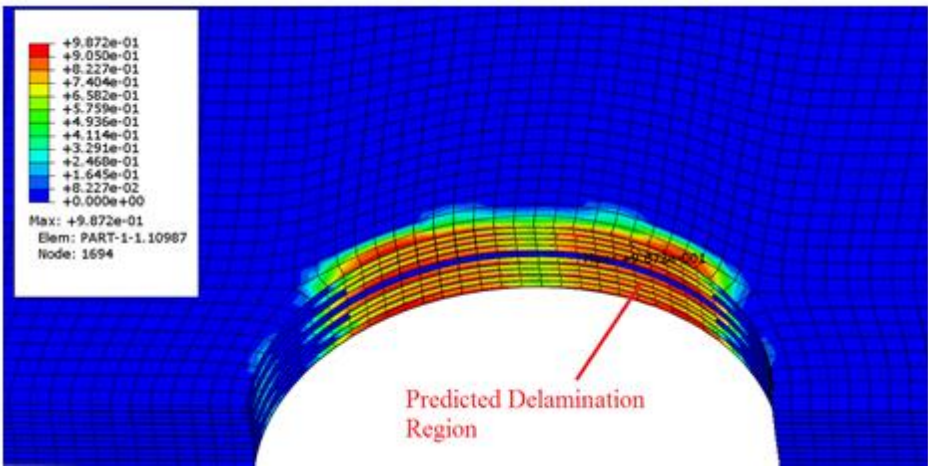
Figure 51: Damaged cohesive elements in the open hole tensile specimens without the film

After determining the region of delamination initiation location in the pre-analysis for the DOHT specimens, teflon film is planned to be placed in the critical location to further investigate the delamination progression. In the DOHT specimens, the thickness of the teflon film is 30μm and the diameter is 6 mm.. It should be noted that although the critical location is determined to be at approximately 60° with

58

respect to the loading direction, thin films are located at 180° with respect to the axis of tensile loading because of the misalignment of the Teflon film during the manufacturing of the DOHT specimens. In the finite element analysis, DOHT specimens are modeled with 3D cohesive elements and the cohesive elements are modeled between the first and the second ply in the whole FEM, as shown in Figure 52.
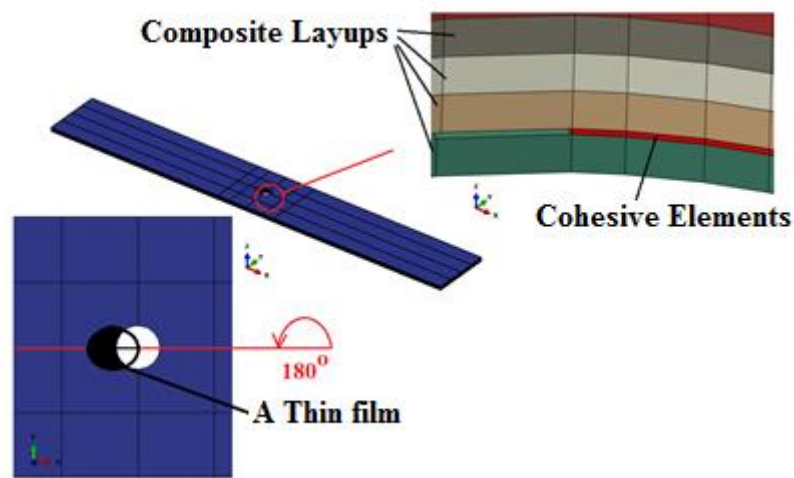
Figure 52: Finite element model of DOHT specimens with cohesive elements

In the finite element analysis of DOHT specimens, 3D solid cohesive elements are used and implicit solver is chosen. The cohesive elements are modeled between the first and the second ply. The step procedure of the delamination analysis is selected as dynamic-implicit step with quasi-static application because of the convergence that it provides in 3D implicit analysis. In the tension test simulation, one end of the DOHT specimen is fixed and maximum failure load for the DOHT specimen is applied at the other end of the specimen to simulate the test condition.

Three DOHT specimens are loaded in tensile tests. In the tests, maximum failure load for the OHT specimens is obtained as 30330N. After the validation of experimental and analysis results for the OHT specimens, the DOHT specimens are loaded in a range so as to follow the delamination progress. The maximum value of

this range is decided by ultimate failure of one DOHT specimen (DOHT-1) and the maximum failure load for this DOHT specimen is obtained as 24750N. Figure 53 shows the load-displacement plot of the DOHT specimens obtained by the test. As shown in Figure 53, the first ply failure load is determined as 20000N by identifying the first load drop in the test. Therefore, applied loads for other DOHT specimens are taken as 18000N (DOHT-2) and 19000N (DOHT-3). The sequential values for the applied loads are chosen in order to observe the progression of the delamination and maximum applied loads for the DOHT specimens are given in Table 4.

Table 4: Maximum applied load for the DOHT specimens

Specimen	Maximum Applied Load (N)
DOHT-1	24754
DOHT-2	18000
DOHT-3	19000

In the load-displacement curve of the present analysis for the DOHT specimens, there is no sudden drop when the load reaches 24750 N, as shown in Figure 53. This could be due to the fact that in the finite element model ply failure is not considered and only interlaminar failure is considered by modeling the cohesive elements. However, in the load –displacement plot given in Figure 53, it can be seen that damage in cohesive elements induces fluctuations in the load-displacement plot. It should also be noted that there is no significant damage in the cohesive elements, as shown in Figure 53 and Figure 58.
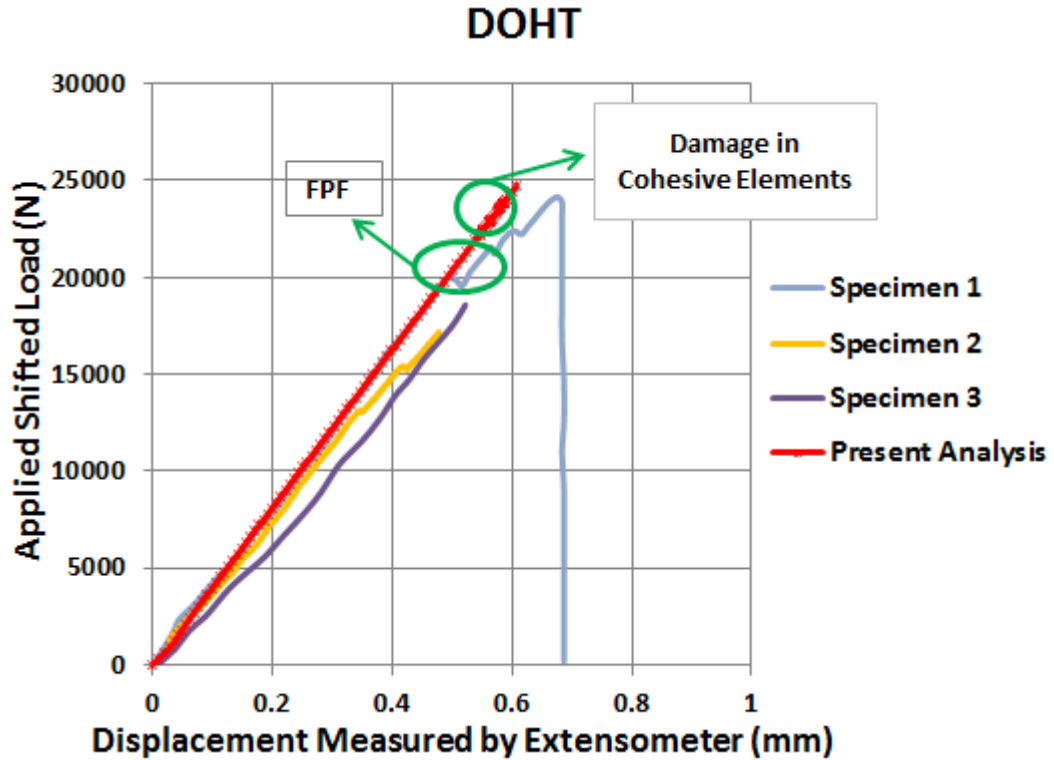
Figure 53: Experimental and analysis results / Displacement vs Load / DOHT

Load-strain data are given in Figure 54-Figure 55 for the DOHT specimens. It can be seen that present analysis results are compatible in the initial linear region with present experimental results for the DOHT specimens.

In Figure 54-Figure 55, curves named as "s_NumberA_sg_NumberB_a" and "s_NumberA_sg_NumberB_b" represent the experimental results. "NumberA" and the "NumberB" have the same explanations as in Figure 38. All strain gauges are dual gauge so there are two strain gauges in the same direction and they are denoted as "a" and "b" in Figure 50 and . Therefore, "s_2_sg_1_a" represents the axial strain results of the Strain Gauge 1 on the Specimen 2 and "s_2_sg_1_b" represents the other axial strain results of the Strain Gauge 1 on the Specimen 2. It should be noted that since the difference between strains in the dual strain gauge is very small, in the finite element analysis strain is calculated at the middle point of the dual strain gauge. It should also be noted that the strain gauge data for the Specimen 1 could not be collected during the experiments.
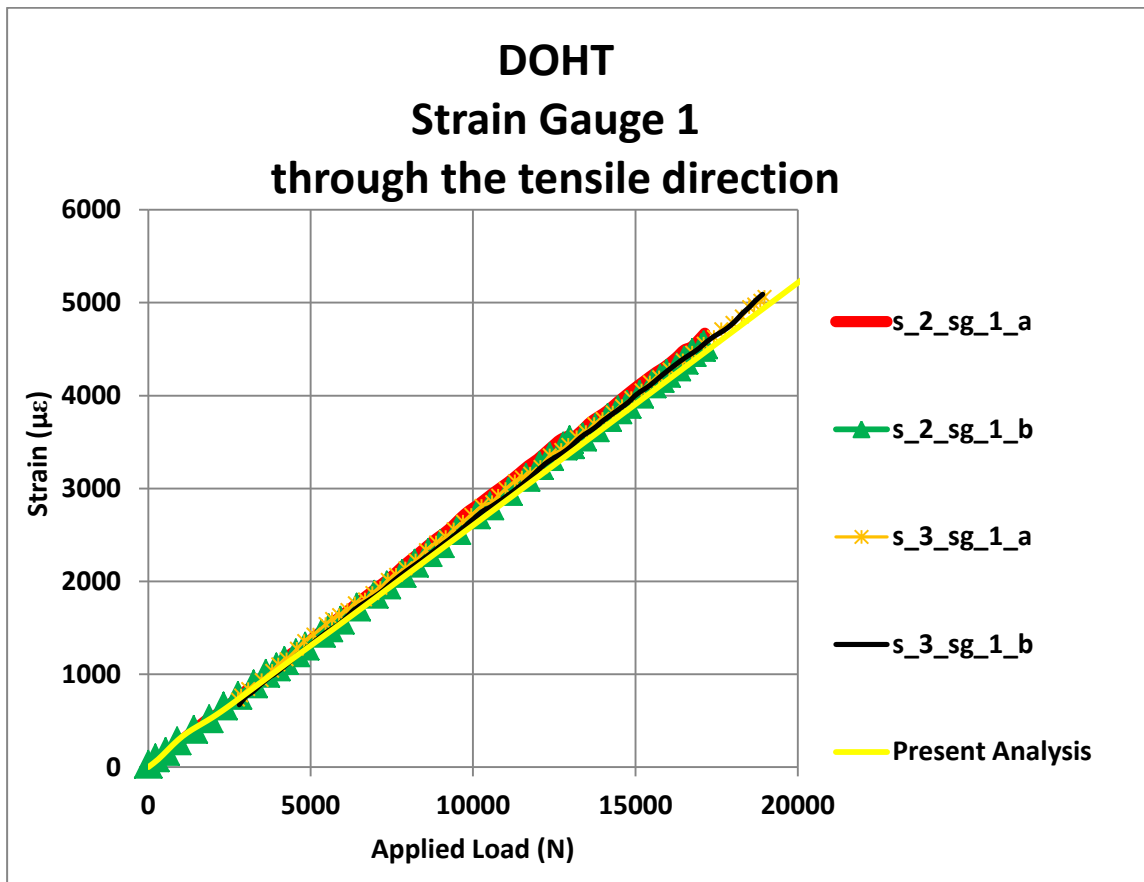
Figure 54: Experimental and analysis results / Load vs Strain gauge / DOHT

Strain gauge 1 in the axial tensile load direction.
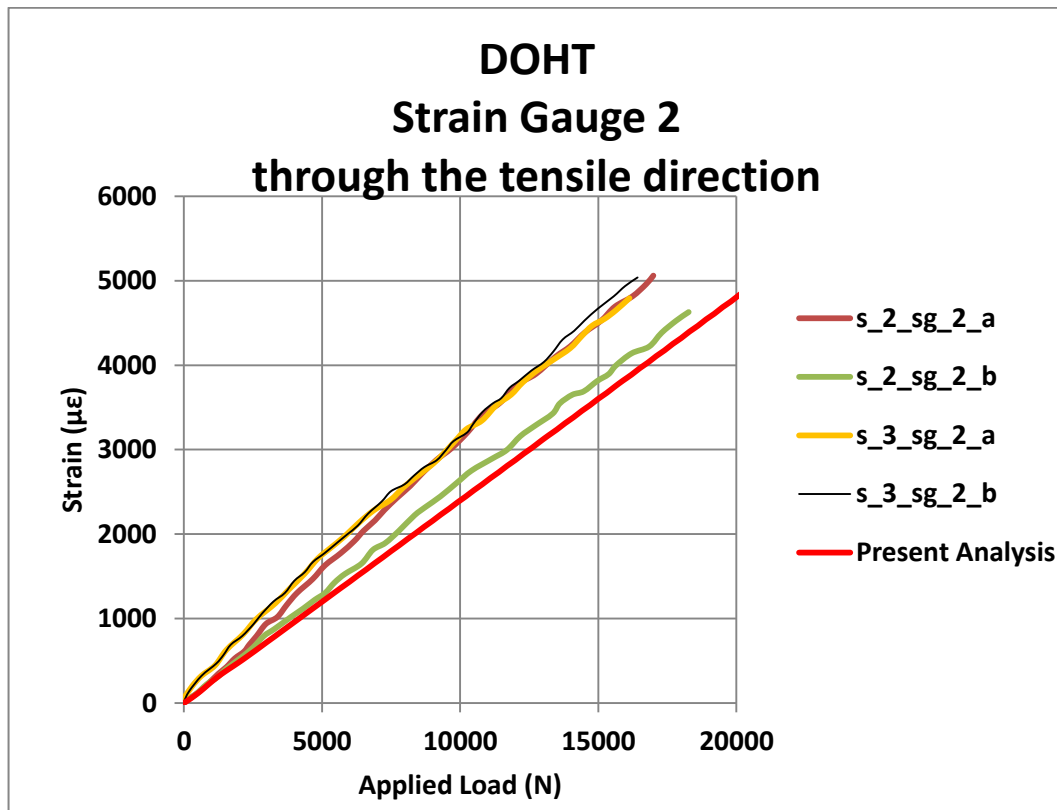
Figure 55: Experimental and analysis results – Load-Strain – DOHT

Strain Gauge 2 in the axial tensile load direction.

Damage detection in composite structures is studied by many researchers. Nondestructive damage detection is highly desirable in order to determine the shape, size, location and the propagation of delamination. The X-ray radiography technique can be used to investigate the subcritical damage in the composite structure laminate loading and unloading but the quality of the published X- ray image is generally restricted [51] [52] [53]. Hosur used Ultrasonic C-Scan technique to detect damages in composite structures that may be caused during the manufacturing and the loading [54]. C-Scan is the most common nondestructive technique that is used in delamination evaluation [55]. In the present study, all DOHT specimens are scanned by the ultrasonic C-Scan before and after the tensile tests to observe the delamination. C-Scans are performed by the company EPSILON Composite. Ultrasonic C-Scan detects damages in laminated composite materials with different shape and size. In this ultrasonic inspection method, test machine catches echoes

generated when an ultrasonic pulse is reflected from an interface, a break or a gap inside the specimen. However, the evaluation of delamination progression in composite structures by the C-Scan technique is very difficult. Determination of delamination size and shape with ultrasonic C-Scan requires experience and good knowledge on composite structures. The difficulties of the evaluation are caused by the selection of the proper probe, frequency of the scan, pulse width, pulse amplitude, pulse repetition rate, delay, blanking, gain, and data processing [56]. The anisotropic effects of the composite material must be considered very well in order to obtain an accurate ultrasonic C-scan image [57]. Therefore, the evaluations and the results of the C-Scan in this study are not exact ones; they are approximate evaluations and results.

Figure 56and Figure 57 show a C-scan image taken before and after the tensile test for the specimen DOHT-3. Their resolutions are different from each other because of the frequency of the scans are different; the scans taken before the tests have low resolution. According the experimental results, increase in the defect area is % 11 for DOHT3, % 7.7 for DOHT2, and % 26.5 for DOHT1. Applied loads and delamination areas are given in Table 5. The size of the initial delaminated area (the area of the teflon film) and the progressive delaminated area obtained from C-scan is less compared to analysis inspection as shown in Table 5. According to a similar study from the literature [58], the damage area of the C-Scan inspection is always significantly smaller than the damage area of the visual inspection. It should be noted that in the C-Scan taken for the DOHT-3, no delamination progression is seen around the hole perpendicular to the loading direction. This is not an expected outcome and it is considered that there might some error in the C-Scan image taken or in the interpretation of the C-Scan image.
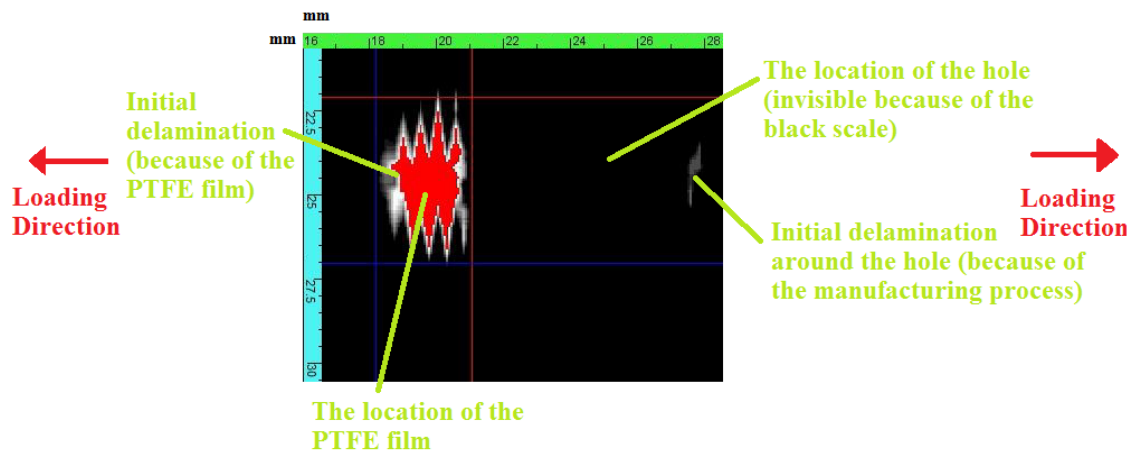
Figure 56: C-Scan before test for DOHT-3
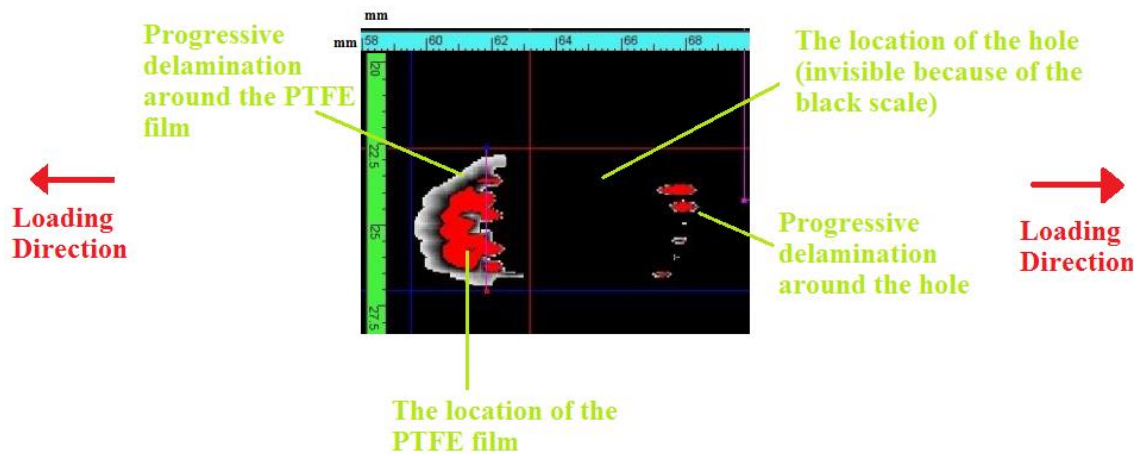
Figure 57: C-Scan after test for DOHT-3

Table 5: The delamination area of DOHT specimens

Specimen	TEST & ANALYSIS	TEST			ANALYSIS			DIFFERENCE BETWEEN TEST & ANALYSIS (%)
	Applied Load (N)	Defect Area (mm²)		Difference (%)	Defect Area (mm²)		Difference (%)	
		Before	After	Increase in Defect Area at Test	Before	After	Increase in Defect Area at Analysis	
DOHT-1	24754	15.7	19.8	26.5	19.7	25.8	30.9	16.6
DOHT-2	18000	13.1	14.1	7.7	19.7	20.7	5.3	31.4
DOHT-3	19000	13.4	14.9	11.0	19.7	21.2	7.5	31.5

Figure 58 shows the damaged cohesive elements determined in the finite element analysis. As it is seen in the finite element analysis delamination progression also occurs perpendicular to the load direction around the hole unlike what is observed in the C-Scan image in Figure 57. From Figure 58, it is also seen that delamination also progresses around the thin film insert in the direction of the tensile loading. This behavior is also observed in the C-Scan image given in Figure 58.

In the finite element analysis, damage initiation and propagation for the DOHT-3 is shown in Figure 58. It should be noted that if the damage indicator has a zero value for a cohesive element, it means that the cohesive element is intact. If the indicator has a value between 0-1, it means that cohesive element is damaged and damage has propagated. However, in this case cohesive elements are not deleted in the analysis model because they still have load carrying capacity. If the indicator is equal to 1, it means that cohesive element is damaged completely and it has no load carrying capacity, therefore cohesive elements are deleted in the analysis model.
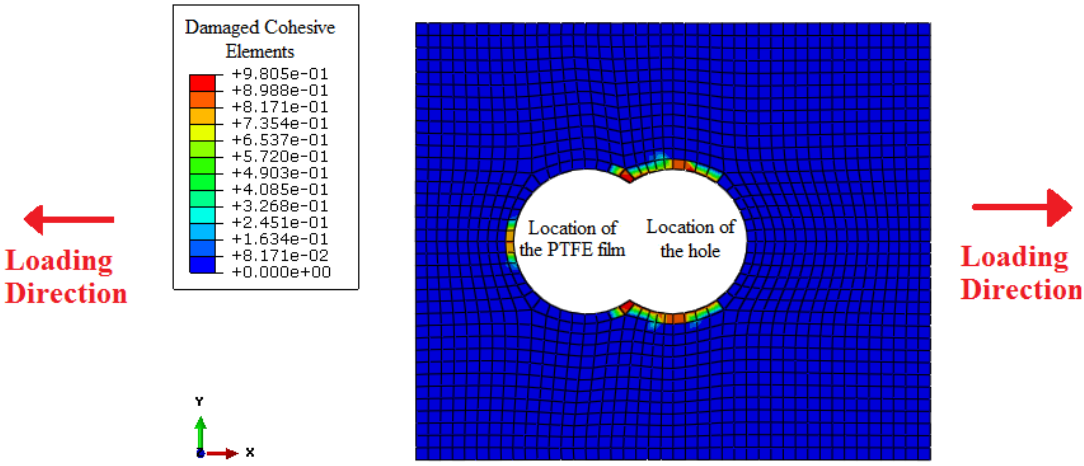
Figure 58: Damaged cohesive elements in the DOHT specimen

Before the finite element analysis, initial delamination area is approximately calculated as 19.7 mm^2. From Table 5, it can be seen that the initial defect areas before the tests of the DOHT specimens measured by C-Scan and calculated in the analysis are different from each other. It should be noted that the current position of the PTFE film is not known at the end of manufacturing process due to the possible sliding of the film during the manufacturing of the specimen. After the finite element

analysis, area of damaged cohesive elements is approximately 1.49 mm^2 for DOHT-3, 1.04 mm^2 for DOHT-2, and 6.09 mm^2 for DOHT-1. Therefore, according to the finite element analysis results, damage progression is approximately % 7.5 for DOHT-3, % 5.3 for DOHT-2, and % 30.9 for DOHT-1.

Based on the results given in Table 5, it can be said that increase in the defect area in the tests and in the finite element analysis are compatible. The progression of the delaminated area can be clearly seen from the increase of the defect size as the tensile load is increased from 18000 N to 24750 N in three separate tests.

It is concluded that both the load-displacement and load-strain curves obtained by the finite element analysis are compatible with present experimental results for both the OHT and the DOHT specimens. Delamination is modelled with 3D solid cohesive elements in the simulation of the DOHT tests. It is seen that increase in the defect area measured by the C-Scan performed after the tests and calculated by the finite element analysis including the cohesive zone modelling are compatible. At the maximum load of 24750 N, the difference in the delaminated areas measured in the test and calculated by the finite element analysis is approximately %17. The preliminary analysis performed on the open hole specimens showed that with the cohesive zone modeling, the progression of delamination can be predicted fairly accurately. It should be noted that in the present study in order to measure the defect area by the C-Scan, tensile tests are performed at three different load levels in separate specimens. The load levels are selected carefully so as to allow progression of delamination starting from the initial defect zone created by the film insert. Open hole tests and analysis provided necessary preparation for the delamination progression test and analysis study on composite missile wings which is the main objective of the thesis. Delamination progression test and analysis study is reported in Chapter 6.

CHAPTER 6

6. ANALYSIS VERIFICATION of COMPOSITE MISSILE WING TESTS

In this chapter, after the completion of delamination initiation and propagation study for the DCB, ENF, OHT and DOHT specimens by finite element analysis, delamination progression in composite missile wings is studied. In this respect, composite missile wings manufactured by the same twill composite are tested in bending loading. Delamination progression test and analysis study performed for the composite missile wing is presented.

6.1. Test and Analysis Results of Wings (W) and Delaminated Wings (DW)

After the completion of delamination initiation and propagation study for the DCB, the ENF, the OHT and the DOHT specimens by FEA, composite missile wings manufactured by the same twill composite are tested in bending loading. Composite missile wings are produced both with teflon film made of PTFE and without it by ODAK Composite Technologies Inc.. Tests of composite missile wings without the teflon film (W) and composite missile wings with the film (DW) are performed by bending loading condition. In addition to the load-displacement data, strain gauge data is also obtained from tests.

Delaminated wings are manufactured with the thin teflon film made of PTFE which is inserted in the pre-selected location. First, test and analysis results of the W wings are studied in this chapter. Tests and analyses results of the DW wings are examined in detail later.

Displacement measurement and load application piston have rubber noses in order not to damage the composite wings. Moreover, necessary adjustments on the displacement measurement and the load application piston are made before experiments, so they do not apply preload to the composite wings. Bending tests for composite wings (Ws and DWs) are made load-control mode. Test equipment, which is designed and made by the composite wing specimen manufacturer and the wing specimen are shown in Figure 59 and Figure 60.
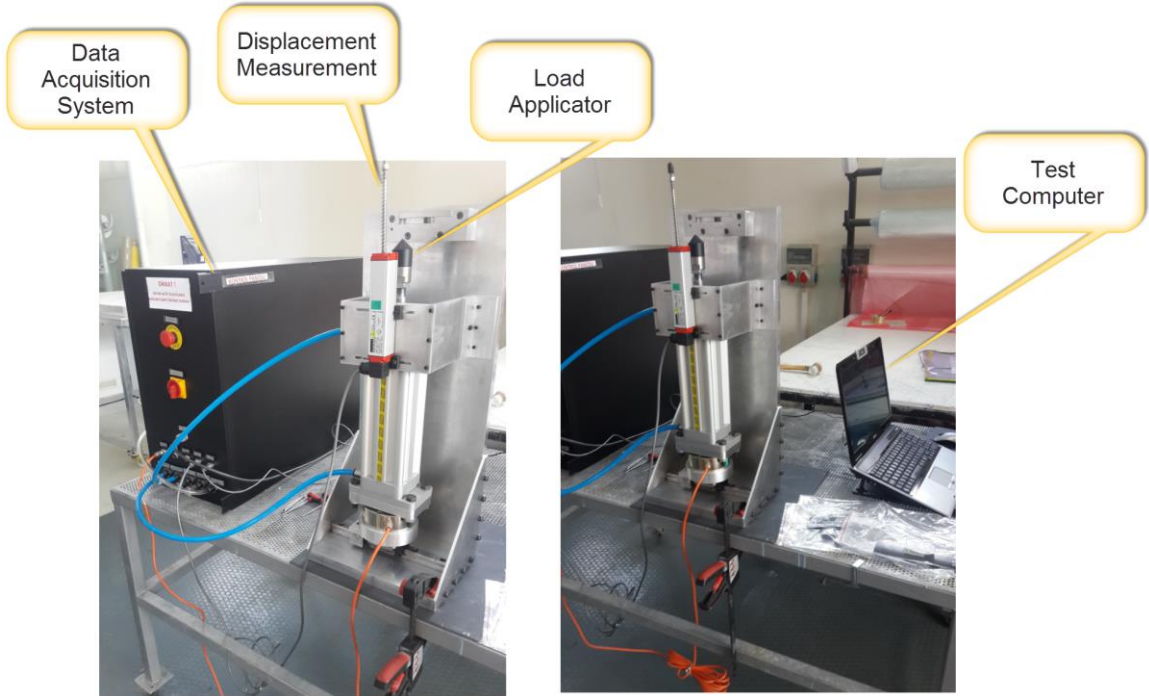
Figure 59: Bending test set-up for wings
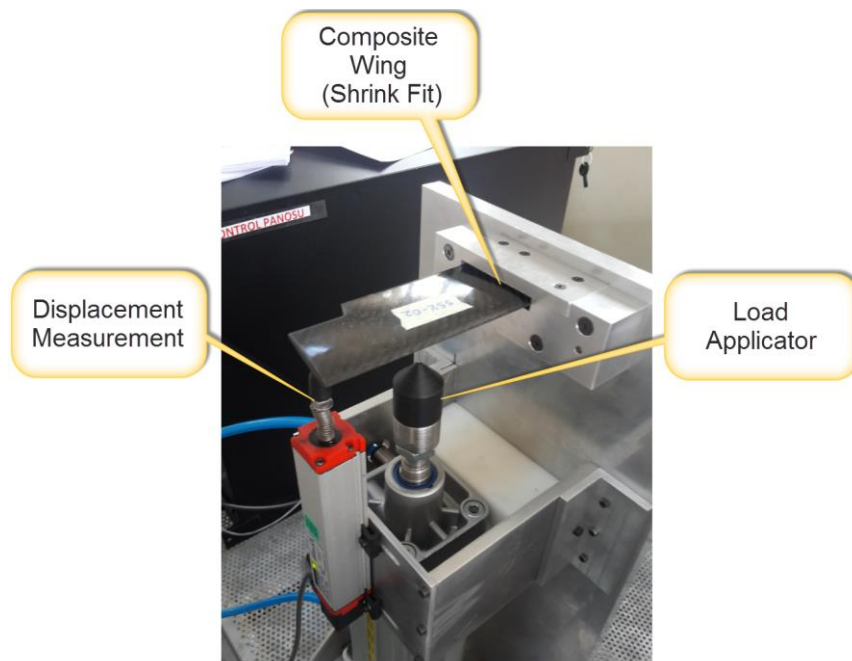
Figure 60: Composite missile wing mounted to the bending test set-up

As shown in Figure 61, one strain gauge is placed on the W and the DW wings so as to obtain strain data along the wing axis directions. The biaxial strain gauge is near the root of the W and DW wings and concentric with the film inserted between the first and the second ply for DW wings.
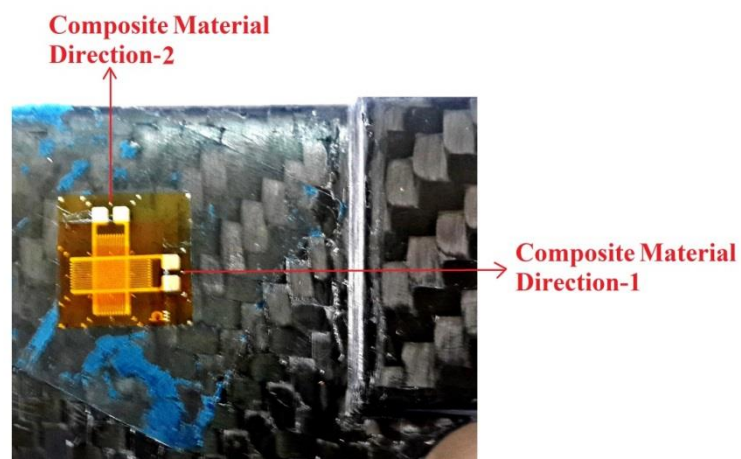
Figure 61: Strain gauge location on the composite wing

The maximum thickness at tip of the composite wings is 6 mm and the thickness of the root is 10 mm. The diameter of the PTFE film is 9 mm and thickness of the film is 60μm. It is inserted between first and second ply in the DW wings because these plies are closest to the outer surface and exposed to tensile loading and the maximum stress occurs in this interface. Plies are oriented as $[0^o/45^o]_{8s}$ for the airfoil portion and $[0^o/45^o]_{13s}$ for the root portion of the wing. Each layer of the composite wings has 0.2 mm thickness. The elastic moduli in wrap and fill directions ($E_{11}= E_{22}$) for twill material are taken as 65313 MPa for W and DW wings. In the thesis study, modal test and subsequent modal analysis of the composite missile wing are also performed in order to obtain natural frequency and verify the elastic moduli in the wrap and fill directions of composite wings without film (W). This study is explained in APPENDIX C. In the finite element analysis of the composite wing for the static loading and modal analysis, composite layups are initially modelled with 8-node linear brick, incompatible mode elements C3D8I in ABAQUS, just like the finite element models used for the DCB/ENF and open hole specimens. But this time, with the C3D8I elements convergence problem is encountered in the finite element analyses. To overcome the convergence problem, composite layups are then modelled with 3D solid linear elements C3D8 and 3D solid cohesive elements COH3D8 in ABAQUS. The step procedure of the delamination analysis is selected as dynamic-implicit step with quasi-static application because of the convergence that it provides in 3D implicit analyses. The total number of elements is 528814 (89432 COH3D8, 439382 C3D8) and the total number of nodes is 606162. Global element size in finite element model changes between from 0.5 mm to 5 mm. Mesh details of finite element model for the W wings and the DW wings are shown in Figure 62. Different colors in Figure 62 represent different plies named as material sections in ABAQUS. The cohesive elements are modeled between the first and the second plies of the composite missile wing. First and second plies of the composite missile wing are exposed to maximum tension load in bending tests. The PTFE film is modeled as space in FEM of the DW wings. The space of the PTFE film and the cohesive elements can be seen in Figure 63.
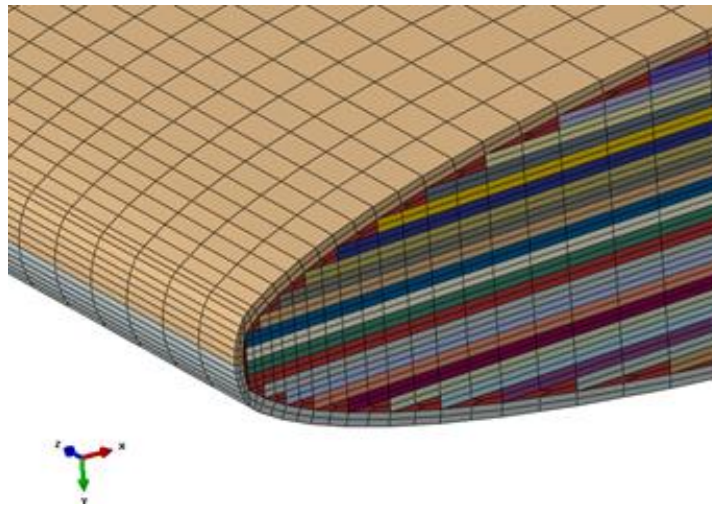
Figure 62: Finite element model of composite missile wing
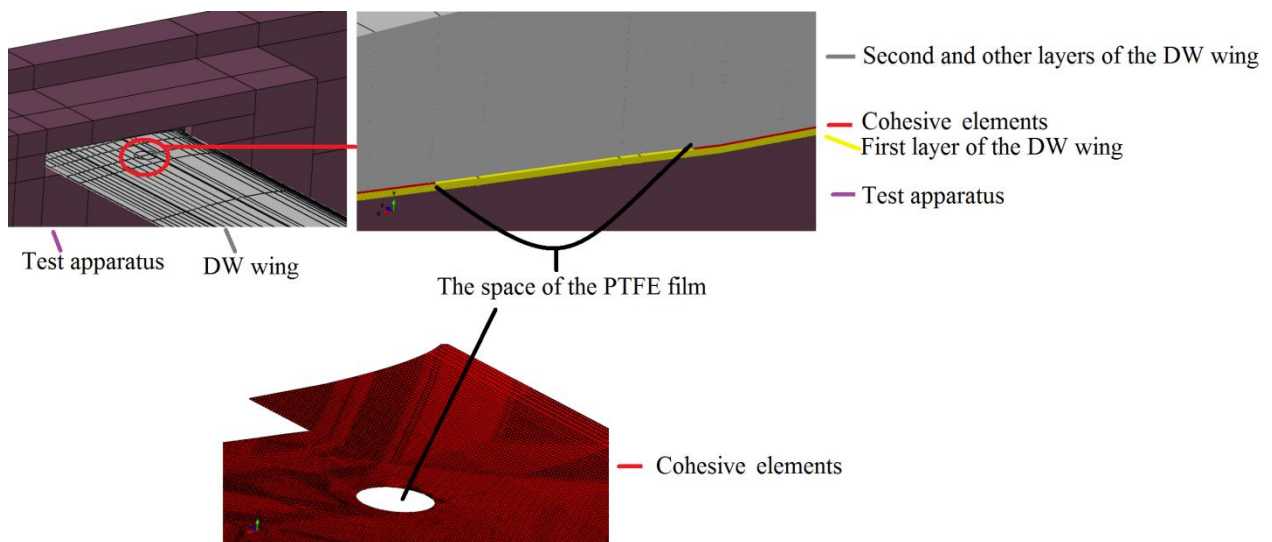
Figure 63: Location of the film and cohesive elements for the DW wings in FEM

Wings are exposed to the bending load conditions. Test apparatus is also modeled as a deformable body in the finite element model and surface-to-surface interaction is defined between the apparatus and wings to represent the shrink fit. Test apparatus is clamped at the bottom surface. Boundary conditions for the W wings and the DW wings are displayed in Figure 64.
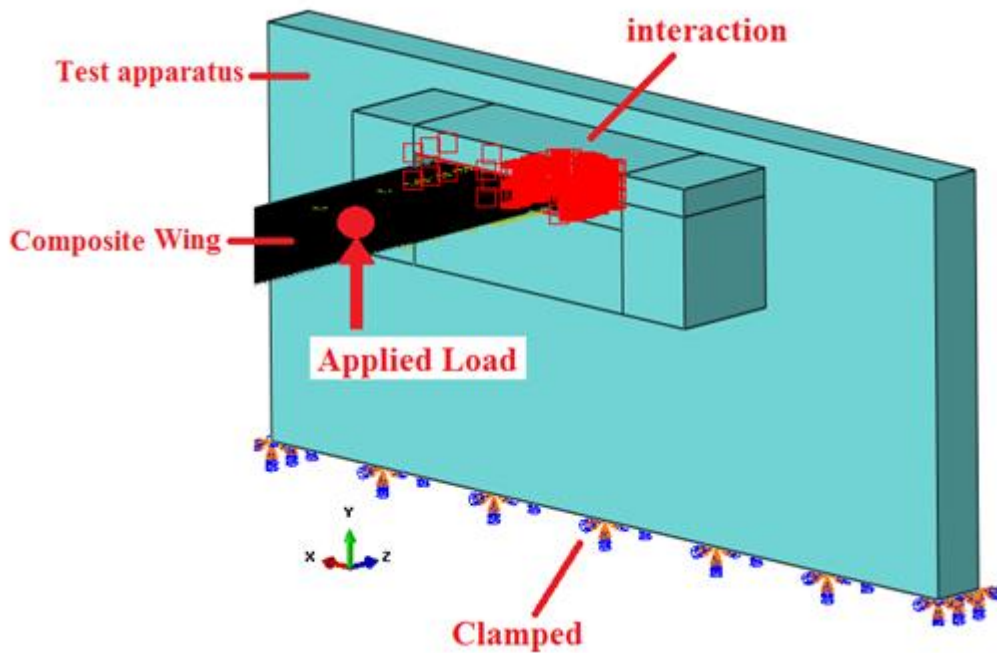
Figure 64: Boundary conditions of the composite missile wing

Two W wings (W-1 and W-2) are held at the root and the applied load at the center of pressure of the wings is 1000N in the top direction, as shown in Figure 64. Experimental and analysis results are plotted as load-displacement plots in Figure 65 and as load-strain plots in Figure 66 and Figure 67 for the W wings.

Figure 65, Figure 66 and Figure 67 show that in the linear range, both the load-displacement and load-strain curves obtained by the finite element analysis match with the experimentally determined curves. Test results show some non-linearity which cannot be captured by the linear elastic model of the composite material of the missile wing. In the literature, such non-linear behavior is also observed in testing of composite structures and reasons for the non-linear behavior is discussed in detail [59] [60]. The possible sources for the non-linear behavior are attributed to material, geometrical nonlinearity and progressive failure that occur during the loading. Nonlinear constitutive behavior of the matrix of the composite structure, progressive failure of delamination, stiffness reduction in the composite structure, and geometrical nonlinearity such as wavy tows under tensile loading are stated as possible reasons for the non-linear behavior [59]. In the present study, the effect of

geometric nonlinearity is studied on a simple finite element model which is very similar to the of the geometry missile wing in APPENDIX D.

In the load-strain curves of the W wings, the transverse direction and the span wise direction strains can be predicted correctly by finite element analysis. In the load-displacement curve of the present analysis for the W wings, there is no sudden drop when the load reaches at 1000N, as shown in Figure 65, because in the initial analysis, intralaminar failure criterion is not included in the analysis. In the present study, the main aim was to study the delamination progression by finite element analysis and verify the test results. In the test specimens and analysis models thin film inserts are used to initiate delamination. Both interlaminar and intralaminar failures are not considered together within the scope of the thesis. This study is recommended as the future work. Intralaminar failure criterion is only considered in the finite element analysis of DOHT specimens to decide on the proper location for the placement of the thin film insert to initiate delamination.
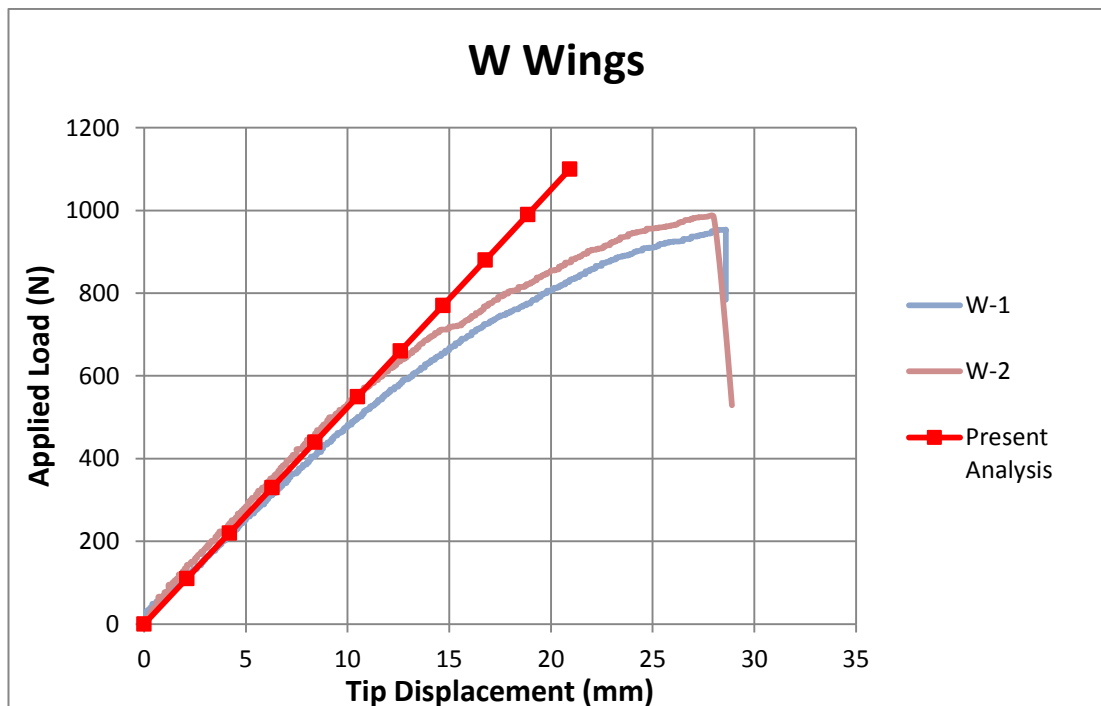
Figure 65: Load-displacement curve for W wings
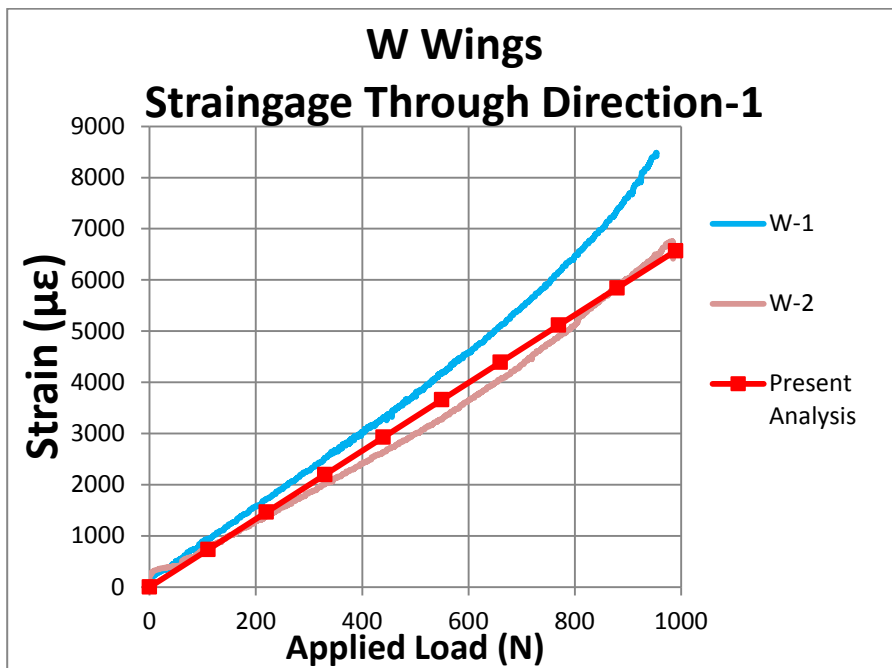
Figure 66: Load-strain curve for W wings in direction-1 (span wise direction)
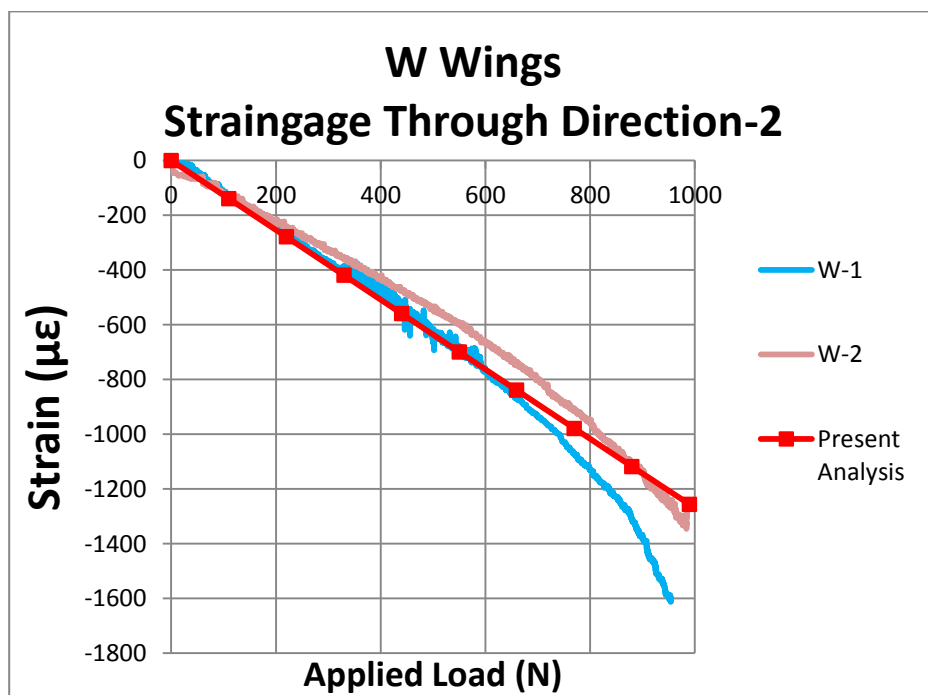
Figure 67: Load-strain curve for W wings in direction-2 (transverse direction)

Three DW wings (DW-1, DW-2 and DW-3) are held at the root and the load at the surface point through the center of pressure of the wings is applied in the top direction just like the W wings. DW wings are loaded in a range so as to follow the delamination progress. The maximum value of this range is decided by the ultimate failure of one of the DW wings (DW-2) and based on the test result of DW-2, the maximum failure load for DW wings is obtained as 1030N. Therefore applied loads for other DW wings are taken as 1000N (DW-1) and 950N (DW-3). The sequential values for applied loads are chosen to observe the progression of the delamination. FEM of the DW wings are similar with FEM of the W wings and the maximum applied loads for the DW wings are given in Table 6.

Table 6: Maximum applied load for the DW wings

Specimen	Maximum Applied Load (N)
DW-1	1000
DW-2	1030
DW-3	950

Experimental and analysis results are plotted as load-displacement plots in Figure 68 and as load-strain data are given in Figure 69 and Figure 70 for the DW wings.

Load-displacement and load-strain curves of the DW wings obtained by the finite element analysis match closely with the experimental results, especially in the linear region. Test results show some non-linearity which cannot be captured by the linear elastic model of the composite material of the missile wing. This non-linearity can be caused by material and geometrical nonlinearity and progressive failure.

In the load-displacement curve of the finite element analysis for the DW wings, no sudden load drop is observed as the sign of damage. It should be noted that cohesive elements is modeled in the finite element analysis of the DW wings, but there is no

significant damage in the wing, but there are only small damages with enforcement at that loads.
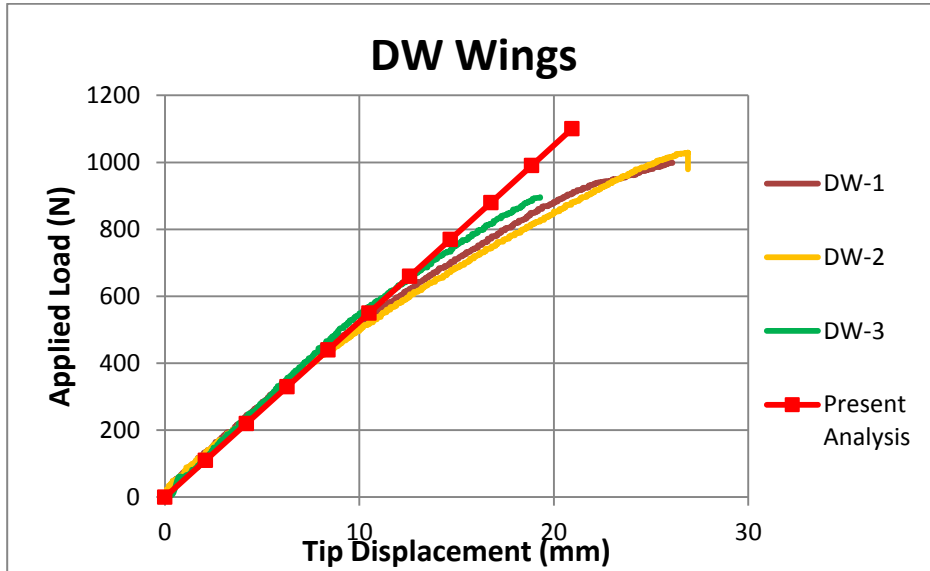
Figure 68: Load-displacement curve for DW wings
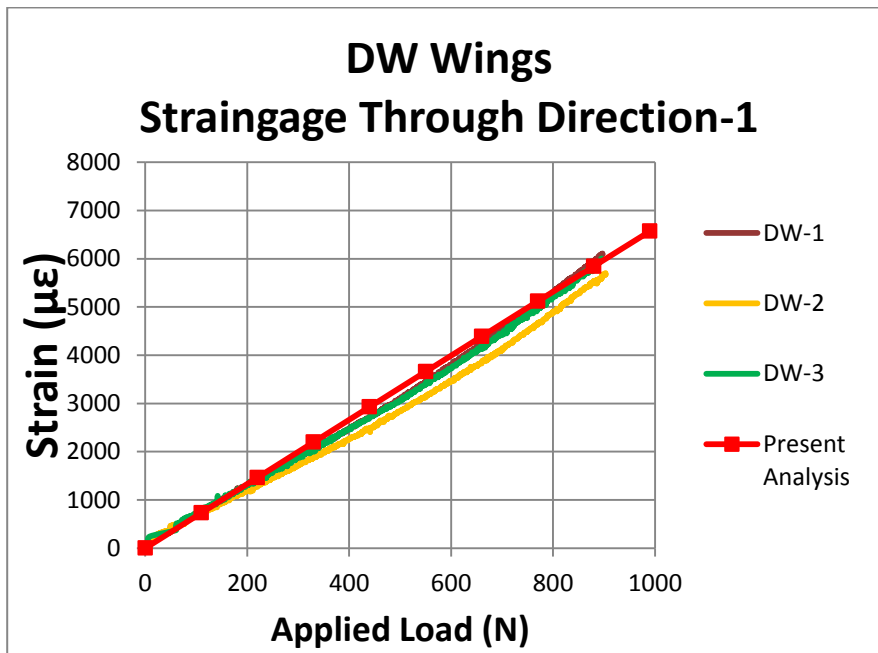
Figure 69: Load-strain curve for W and DW wings in direction-1 (span wise direction)
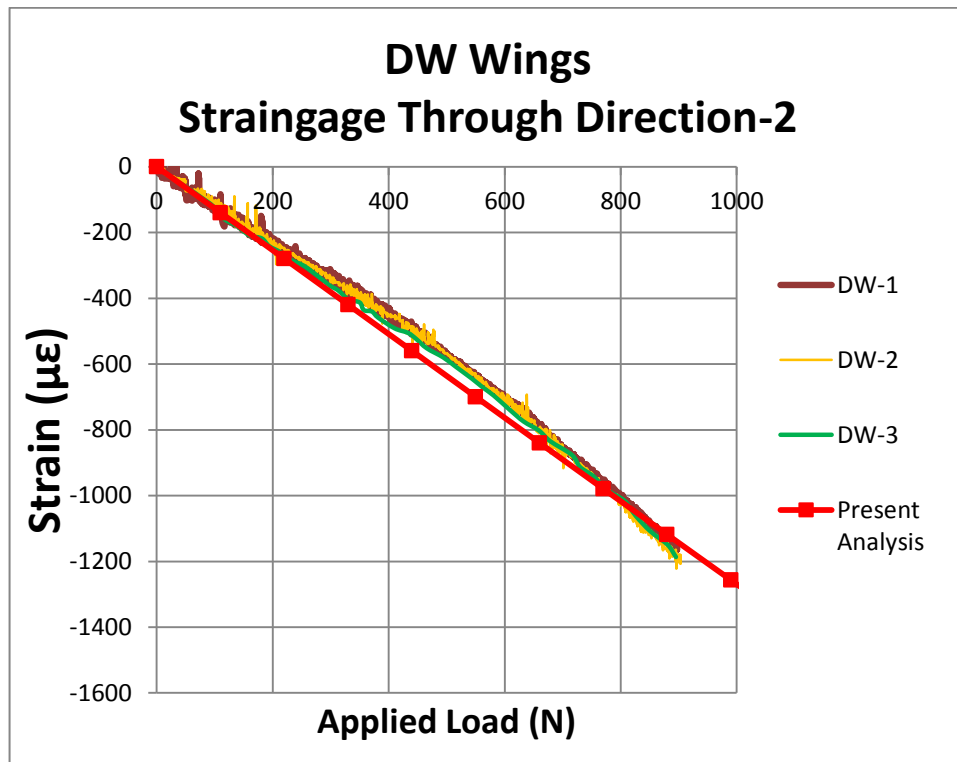
Figure 70: Load-strain curve for W and DW wings in direction-2 (transverse direction)

All the DW wings are also scanned by ultrasonic C-Scan before and after the bending tests to observe the delamination by EPSILON Composite. Figure 71 shows the C-Scan operation. Figure 72-Figure 74 show C-scan images taken before and after the bending test for DW-1, DW-2 and DW-3. The scans are shown in two colors as black-red and orange-green. The measurements are not different for both color scales; the resolution of the scan is only change so the orange-green scale is preferred for after in Figure 72. They are exposed to 1000N, 1030 N and 950N respectively. Applied loads for the DW wings are in a range so as to follow the delamination progress. According the experimental results and C-scan images, increment of defect area is %9.25 for DW-1, % 11.18 for DW-2, and %1.25 for DW-3.

NDT: Ultrasonic Inspection (C-Scan)   Composite Wing
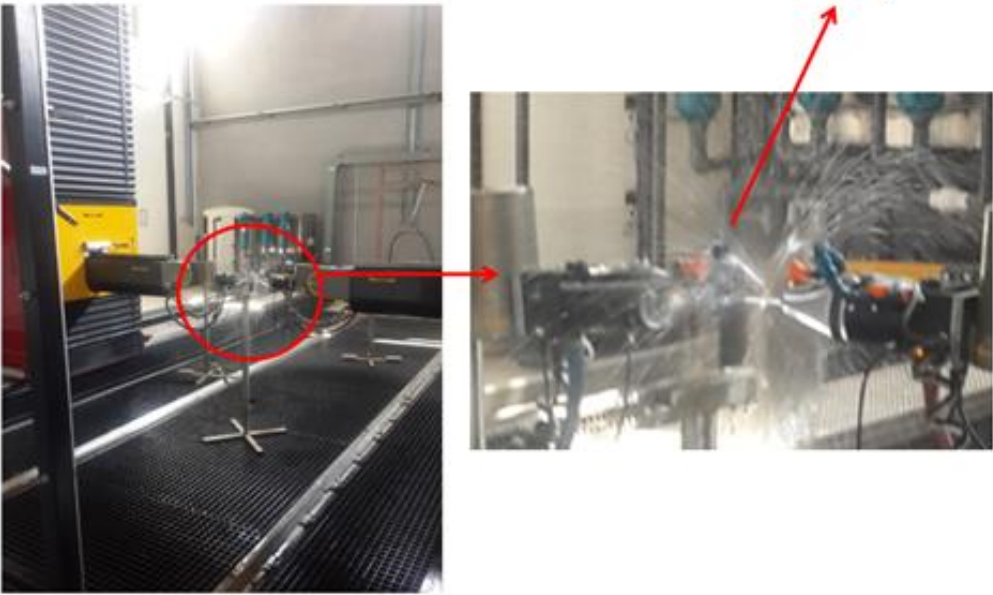
Figure 71: C-Scan for DW wings

Before
46.5 mm^2

After
50.8 mm^2

mm

mm
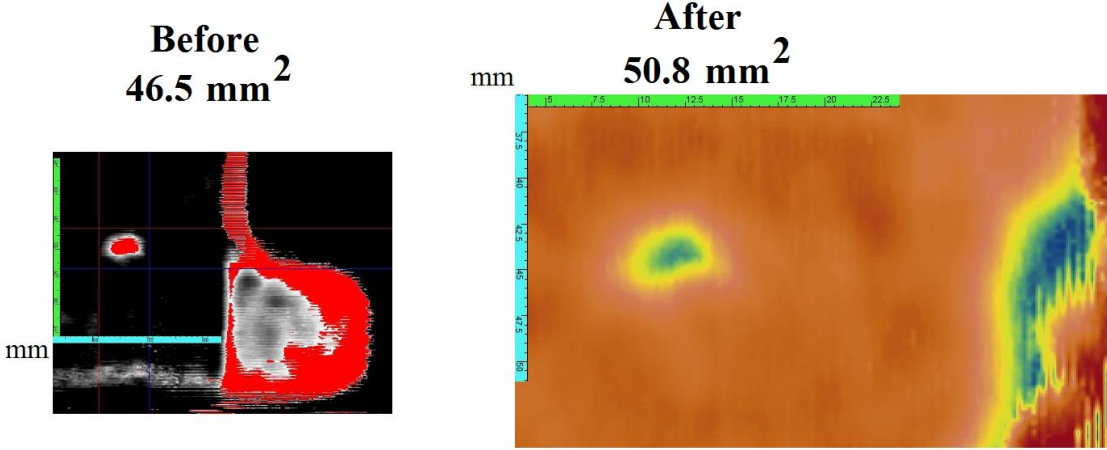
Figure 72: Images of C-Scan before and after the bending test for DW-1 / Load
=1000N

Before
63.5 mm^2

After
70.6 mm^2

mm

mm
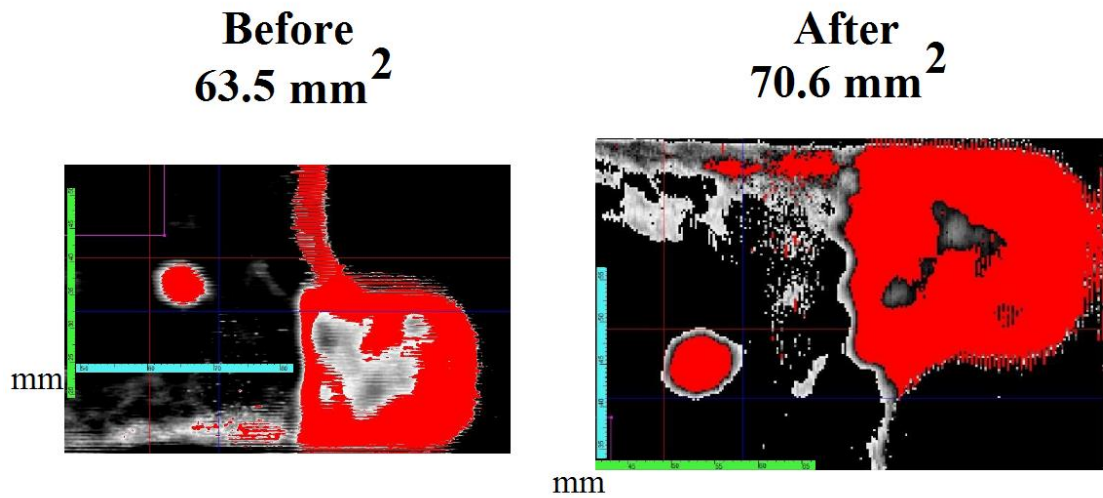
Figure 73: Images of C-Scan before and after the bending test for DW-2 / Load=1030 N

Before
84 mm^2

After
85.05 mm^2

mm

mm
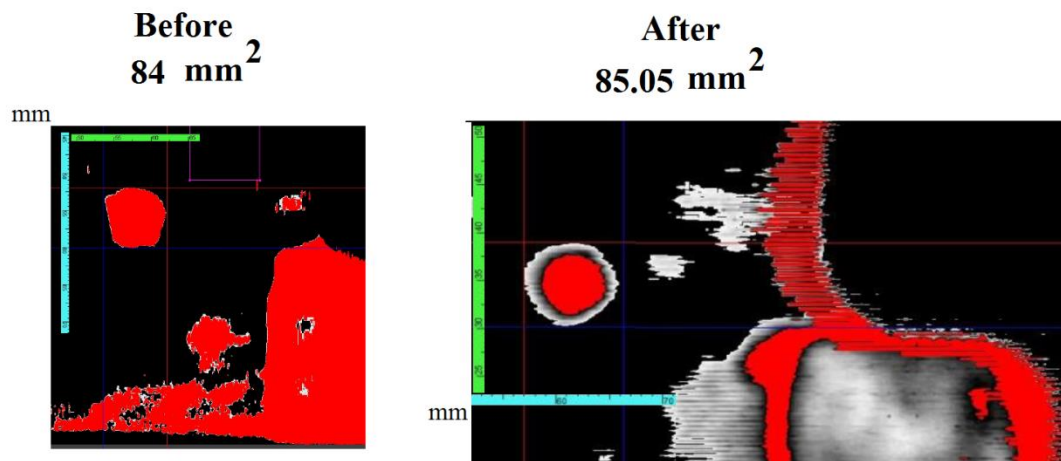
Figure 74: Images of C-Scan before and after the bending test for DW-3 / Load=950 N

In the finite element analysis of wings, the cohesive elements are modeled between the first and the second ply as they are exposed to tension loading. Before the finite element analysis, initial delamination is approximately calculated as 63 mm^2. It should be noted that the difference between the film areas in analysis model and the specimen is probably caused due to the crimping of the film in the interface during the manufacturing process. After the finite element analysis, damaged cohesive

81

elements area is calculated as approximately 4 mm^2 for DW-1, 5.6 mm^2 for DW-2, and 2 mm^2 for DW-3. Therefore, damage progression is approximately %7.5 for DW-1, %10 for DW-2, and %3.7 for DW-3 according to the finite element analysis results. In the finite element analysis results, damage initiation and propagation for the DW-1, DW-2, and DW-3 are shown in Figure 75-Figure 77. It should be noted that the damage indicator of the cohesive elements is such that if the indicator has a zero value for a cohesive element, it means that the cohesive element is intact. If the indicator has a value between 0-1, it means that cohesive element is damaged and damage has propagated. However, in this case cohesive elements are not deleted in the analysis model because they still have load carrying capacity. If the indicator is equal to 1, it means that cohesive element is damaged completely and it has no load carrying capacity, therefore cohesive elements are deleted in the analysis model. In Figure 75-Figure 77, it is noted that failure indicator has a value between 0.5 and higher at the right hand side. A value of 0.5 or higher means that at least half of the cohesive element is damaged.
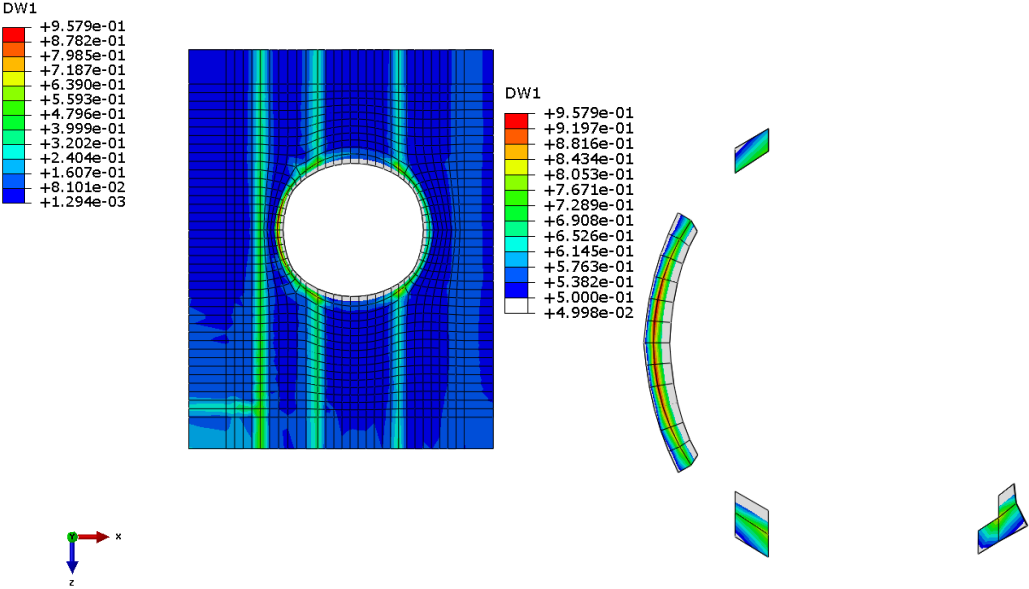
Figure 75: Damaged cohesive elements in the DW-1
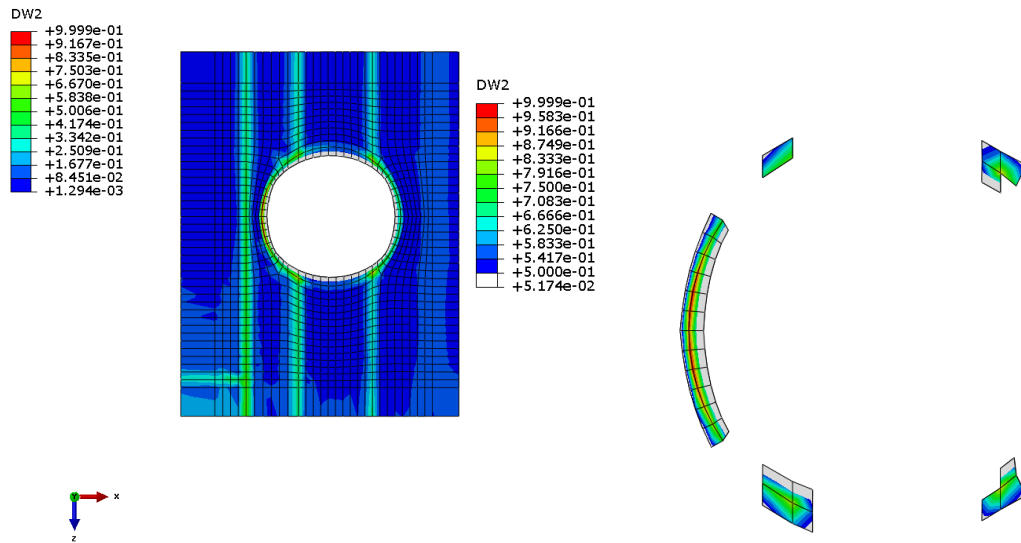
Figure 76: Damaged cohesive elements in the DW-2
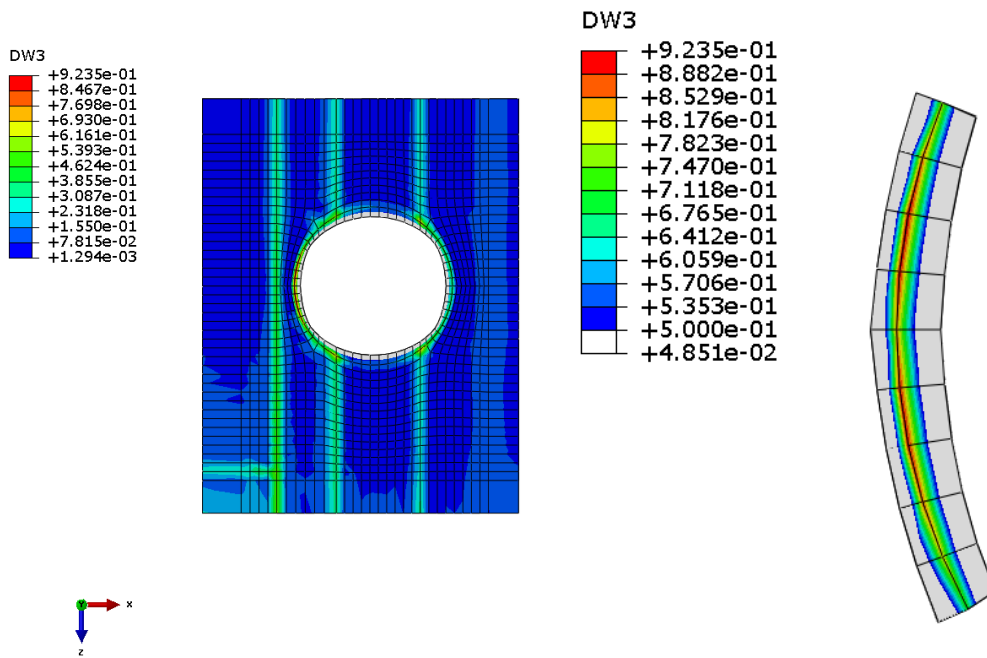
Figure 77: Damaged cohesive elements in the DW-3

Table 7 compares the initial and final defect area obtained in the finite element analysis and bending tests of the wings. In Table 7, it can be seen that the initial defect area before the tests of the DW wings measured by C-Scan for the test wings

and calculated in the analysis are different from each other. This is because the current position of the PTFE film is not known at the end of manufacturing process due to the possible sliding of the film during the manufacturing of the wing. In the finite element analysis, the PTFE film is modelled as an optimum size.

Based on the results given in Table 7, it can be said that increase in the defect area in the tests and in the finite element analysis are compatible. The progression of the delaminated area can be clearly seen from the increase of the defect size as the bending load is increased from 950 N to 1030 N in three separate tests.

Table 7: The delamination area of the DW wings

Specimen	TEST & ANALYSIS Applied Load (N)	TEST Defect Area (mm^2)		Difference (%) Increase in Defect Area at Test	ANALYSIS Defect Area (mm^2)		Difference (%) Increase in Defect Area at Analysis	DIFFERENCE BETWEEN TEST & ANALYSIS (%)
		Before	After		Before	After		
DW-1	1000	46.5	50.8	9.2	63.0	68.0	7.9	14.6
DW-2	1030	63.5	70.6	11.2	63.0	69.5	10.4	7.3
DW-3	950	84.0	85.1	1.3	63.0	65.0	3.2	154.0

It should be noted that the delaminated wing seems to be stiffer than the intact wing. The reason for this could be due to the different manufacturing times of the W and the DW wings. In the present study, W and DW wings are manufactured in different molds and at different times so the properties of the W and the DW wings can differ from each other. In the bending response of the wings in the tests, the non-linear behavior could not be captured by the finite element analysis due to the fact that the material model used in the finite element analysis is linearly elastic. Both the load-displacement and load-strain curves obtained by the finite element analysis are compatible with present experimental results for both the W and the DW wings.

Delamination is modelled with 3D solid cohesive elements in the simulation of the DW tests. It is seen that increase in the defect area measured by the C-Scan performed after the tests and calculated by the finite element analysis including the

cohesive zone modelling are compatible. At the maximum load of 1030 N, the difference in the delaminated areas measured in the test and calculated by the finite element analysis is approximately %7.3 which is a quite acceptable difference. The preliminary analysis performed on a real structure such as a composite missile wing showed that with the cohesive zone modeling, the progression of delamination can be predicted fairly accurately. It should be noted that in the present study in order to measure the defect area by the C-Scan, bending tests are performed at three different load levels in separate missile wings. The load levels are selected carefully so as to allow progression of delamination starting from the initial defect zone created by the film insert.

CHAPTER 7

7. CONCLUSION

Objective of the thesis is to investigate the interlaminar progressive failure behavior of the composite wing of a missile manufactured by twill composite by finite element analyses and tests. In this study, Cohesive Zone Method (CZM) is used as an approach to Fracture Mechanics. In CZM, delamination between the layers is represented by cohesive elements in composite structures. Delamination initiation and propagation in the structure is predicted with the behavior of these interface elements. In CZM, damage mechanism is modeled by traction-displacement constitutive relationships.

Finite element analyses (FEA) are conducted for delamination analysis in composites using three dimensional (3D) solid cohesive elements. Finite element analyses are performed by ABAQUS [9].

For the verification study on the cohesive zone modeling, three dimensional models of Double Cantilever Beam (DCB) and End Notch Flexure (ENF) specimens are generated in ABAQUS with 3D cohesive elements in the delamination interface. In the literature, for the delamination analysis in 3D, generally explicit finite element analysis is performed for better convergence characteristics. In the present study, implicit finite element analysis is used in the 3D models of the DCB and ENF specimens with 3D cohesive elements in the delamination interface. For the verification study, delamination analysis results of the present study are compared with the DCB and ENF analysis and test data of Travesa [16]. In ABAQUS, the step procedure of the delamination analysis is selected as dynamic-implicit step because of the convergence that it provides in 3D implicit analyses. The other step procedures are static general step with default definition and static general step with automatic

stabilization definition. It is noted that the analysis results do not match the results of Travesa [16] if static general steps are used.

Parametric study is performed for the Double Cantilever Beam (DCB) and the End Notch Flexure (ENF) specimens with cohesive zone method (CZM) to model the delamination initiation and propagation using the material data of Travesa [16]. The results of parametric study for the DCB and the ENF specimens are presented for variations in the normal and shear mode fracture energy (G_{IC}, G_{IIC}), stiffness of cohesive elements (K) and global and cohesive element sizes. It is noted that fracture energies (G_{IC} and G_{IIC}) are generally determined by Mode I and Mode II tests. The present analysis showed that the use of lower or higher fracture energy than the nominal value caused under and over estimation of delamination initiation, respectively. It is also concluded that the penalty stiffness should not be low because with low penalty stiffness value delamination initiation cannot be predicted. In the literature, the recommended value of the penalty stiffness is in the range of 10^5 or 10^6 kJ/m^2. The analyses performed in the present study also confirm the suitability of this range. Finally, the size of cohesive elements must be 0.5 mm or less in order to predict the delamination onset and progression accurately for standard DCB and ENF specimens.

In order to perform finite element based delamination analysis, fracture toughness data of the carbon-epoxy twill composite is obtained from tests to be used in open hole tensile and wing bending analysis. DCB and ENF specimens are tested with Mode I and Mode II loading in order to obtain interlaminar fracture toughnesses, G_{Ic} and G_{IIc}. Mode I test is based on ASTM D5528-13 and Mode II test is based on DIN-EN 6034. DCB and ENF specimens are also modelled in ABAQUS by using cohesive elements in the delamination interface to inspect the delamination initiation and propagation. The ply properties of deltapreg STE-DT121H-2 epoxy resin/T300-3K-2x2 twill prepreg composite are obtained by material tests. Composite layups are modelled with 8-node linear brick, incompatible mode elements (C3D8I) and the cohesive layer is modelled with 8-node three-dimensional cohesive elements (COH3D8). It is concluded that results of finite element analysis with cohesive zone

modeling approach are compatible with present experimental results for both Mode I and Mode II loading conditions.

After the completion of delamination initiation and propagation study for the DCB and the ENF specimens by FEA, open hole tensile specimens are manufactured by the same twill composite is tested in tensile loading. Open hole tensile specimen test and analysis study is the transition step between the DCB and the ENF specimens and missile wing which is the ultimate goal of the thesis study.

Before the analyses and tests of the missile wing are performed, a simpler structure is modelled and tested to investigate the delamination behavior in the twill composite. In this study, simpler structure is selected as the open-hole plate. To initiate delamination, a thin film (i.e. polytetrafluoroethylene, PTFE) is inserted in a known location the composite plate in order to examine the delamination behavior. It is concluded that both the load-displacement and load-strain curves obtained by the finite element analysis are compatible with present experimental results for both the OHT and the DOHT specimens. Delamination is modelled with 3D solid cohesive elements in the simulation of the DOHT tests. It is seen that increase in the defect area measured by the C-Scan performed after the tests and calculated by the finite element analysis including the cohesive zone modelling are compatible. At the maximum load of 24750 N, the difference in the delaminated areas measured in the test and calculated by the finite element analysis is approximately %17. The preliminary analysis performed on the open hole specimens showed that with the cohesive zone modeling, the progression of delamination can be predicted fairly accurately. It should be noted that in the present study in order to measure the defect area by the C-Scan, tensile tests are performed at three different load levels in separate specimens. The load levels are selected carefully so as to allow progression of delamination starting from the initial defect zone created by the film insert. Open hole tests and analyses provided necessary preparation for the delamination progression test and analysis study on composite missile wings which is the main objective of the thesis.

In the last part of the thesis, tests and finite element analyses of composite missile wings are performed. It is concluded that global response of the both intact (W) and

delaminated (DW) wings obtained in the experiments and in the finite element analysis agree with each other considerably well. In the bending response of the wings in the tests, the non-linear behavior could not be captured by the finite element analysis due to the fact that the material model used in the finite element analysis is linearly elastic. This non-linearity can be caused by material and geometrical nonlinearity and progressive failure. Both the load-displacement and load-strain curves obtained by the finite element analysis are compatible with present experimental results for both the W and the DW wings.

In the missile wings, delamination is modelled with 3D solid cohesive elements in the simulation of the DW tests. It is seen that increase in the defect area measured by the C-Scan performed after the tests and calculated by the finite element analysis including the cohesive zone modelling are compatible. At the maximum load of 1030 N, the difference in the delaminated areas measured in the test and calculated by the finite element analysis is approximately %7.3 which is a quite acceptable difference. The preliminary analysis performed on a real structure such as a composite missile wing showed that with the cohesive zone modeling, the progression of delamination can be predicted fairly accurately. It should be noted that in the present study in order to measure the defect area by the C-Scan, bending tests are performed at three different load levels in separate missile wings. The load levels are selected carefully so as to allow progression of delamination starting from the initial defect zone created by the film insert.

In this study, delamination between plies (interlaminar) is studied instead of failure of individual plies (intralaminar). It seems like both interlaminar and intralaminar failure could be studied together to predicted the failure of the composite structures correctly. Therefore, it would be better to study on combining intralaminar and interlaminar failure analysis methods to study the failure behavior of open hole specimens and missile wings and comparison with tests. Moreover, in this thesis applied loads on the composite structures are quasi-static loads so the experience in this thesis might be continued with dynamic load case.

REFERENCES

[1] P. P. Camanho, C. G. Dávila, and D. R. Ambur, "Numerical Simulation of Delamination Composite Materials," *Natl. Aeronaut. Sp. Adm.*, no. NASA/TP-2001–211041, pp. 1–24, 2001.

[2] T. K. O'Brien, W. M. Johnston, and G. J. Toland, "Mode II Interlaminar Fracture Toughness and Fatigue Characterization of a Graphite Epoxy Composite Material," *Natl. Aeronaut. Sp. Adm.*, no. NASA/TM-2010–216838, pp. 1–32, 2010.

[3] H. Johnson, L. Louca, and S. Mouring, "Damage modelling of large and small scale composite panels subjected to a low velocity impact," *Heal. Saf. Exec. Res. ...*, no. RR520 Research Report, pp. 1–86, 2006.

[4] D. Xie and A. M. Waas, "Discrete cohesive zone model for mixed-mode fracture using finite element analysis," *Eng. Fract. Mech.*, vol. 73, no. 13, pp. 1783–1796, 2006.

[5] A. Satyanarayana, P. B. Bogert, and P. B. Chunchu, "The Effect of Delamination on Damage Path and Failure Load Prediction for Notched Composite Laminates," *48th AIAA/ASME/ASCE/AHS/ASC Struct. Struct. Dyn. Mater. Conf.*, pp. 1–16, 2007.

[6] K. Song, C. Davila, and C. Rose, "Guidelines and parameter selection for the simulation of progressive delamination," *Abaqus Users' Conf.*, pp. 1–15, 2008.

[7] P. Elisa, "Virtual Crack Closure Technique and Finite Element Method for Predicting the Delamination Growth Initiation in Composite Structures," *Adv. Compos. Mater. - Anal. Nat. Man- Made Mater.*, pp. 463–480, 2011.

[8] R. H. Lopez, M. A. Luersen, and E. S. Cursi, "Optimization of laminated composites considering different failure criteria," *Compos. Part B Eng.*, vol. 40, no. 8, pp. 731–740, 2009.

[9] Abaqus Documentation, "Abaqus 6.14," *Dassault Syst.*

[10]   C. M. Lewandowski, "Meso-scale and Multicontinuum Modeling of a Triaxial Braided Textile Composite," *Master Thesis*, p. 128, 2009.

[11]   S. P. Ng, P. C. Tse, and K. J. Lau, "Progressive failure analysis of 2/2 twill weave fabric composites with moulded-in circular hole," *Compos. Part B Eng.*, vol. 32, pp. 139–152, 2001.

[12]   X. Dai, Y. Wang, C. Tang, and X. Guo, "Mechanics analysis on the composite flywheel stacked from circular twill woven fabric rings," *Compos. Struct.*, vol. 155, pp. 19–28, 2016.

[13]   H. Hadavinia and H. Ghasemnejad, "Effects of Mode-I and Mode-II interlaminar fracture toughness on the energy absorption of CFRP twill/weave composite box sections," *Compos. Struct.*, vol. 89, no. 2, pp. 303–314, 2009.

[14]   K. Vallons, A. Behaeghe, S. V Lomov, and I. Verpoest, "Impact and post-impact properties of a carbon fibre non-crimp fabric and a twill weave composite," *Compos. Part A Appl. Sci. Manuf.*, vol. 41, no. 8, pp. 1019–1026, 2010.

[15]   S. Ng, K. J. Lau, and P. C. Tse, "3D finite element analysis of tensile notched strength of 2 / 2 twill weave fabric composites with drilled circular hole," *Compos. Part B Eng.*, vol. 31, pp. 113–132, 2000.

[16]   A. T. Travesa, "Simulation Of Delamination In Composites Under Quasi-Static And Fatigue Loading Using Cohesive Zone Models," *Dr. Thesis*, p. 218, 2006.

[17]   C. C. Liang, H. W. Chen, and C. H. Wang, "Optimum design of dome contour for filament-wound composite pressure vessels based on a shape factor," *Compos. Struct.*, vol. 58, no. 4, pp. 469–482, 2002.

[18]   P. Xu, J. Y. Zheng, and P. F. Liu, "Finite element analysis of burst pressure of composite hydrogen storage vessels," *Mater. Des.*, vol. 30, no. 7, pp. 2295–2301, 2009.

[19]   D. W. Sleight, "Progressive Failure Analysis Methodology for Laminated Composite Structures," no. 887554, p. 94, 1999.

[20]   D. S. Dugdale, "Yielding of steel sheets containing slits," *J. Mech. Phys. Solids*, vol. 8, no. 2, pp. 100–104, 1960.

[21]   G. N. Barenblatt, "The Mathematical Theory of Equilibrium Cracks Formed in

Brittle Fracture," *Zhurnal Prikl. Mekhaniki i Tec.*, no. 283881, pp. 1–109, 1962.

[22] A. Needleman, "A continuum model for void nucleation by inclusion debonding," *J. Appl. Mech.*, vol. 54, no. 3, pp. 525–531, 1987.

[23] C. G. Dávila, P. P. Camanho, and a. Turon, "Effective Simulation of Delamination in Aeronautical Structures Using Shells and Cohesive Elements," *J. Aircr.*, vol. 45, no. 2, pp. 663–672, 2008.

[24] C. Fan, P. Y. B. Jar, and J. J. R. Cheng, "Cohesive zone with continuum damage properties for simulation of delamination development in fibre composites and failure of adhesive joints," *Eng. Fract. Mech.*, vol. 75, no. 13, pp. 3866–3880, 2008.

[25] O. Al-Khudairi, H. Hadavinia, a. Waggott, E. Lewis, and C. Little, "Characterising mode I/mode II fatigue delamination growth in unidirectional fibre reinforced polymer laminates," *Mater. Des.*, vol. 66, pp. 93–102, 2015.

[26] J. R. Reeder and J. H. Crews, "Mixed-Mode Bending Method for Delamination Testing," *AIAA J.*, vol. 28, no. 7, pp. 1270–1276, 1990.

[27] B. Gözlüklü, "Delamination Analysis by Using Cohesive Interface Elements in Laminated Composite," *Master Thesis*, p. 149, 2009.

[28] Y. Xu and H. Yuan, "On damage accumulations in the cyclic cohesive zone model for XFEM analysis of mixed-mode fatigue crack growth," *Comput. Mater. Sci.*, vol. 46, no. 3, pp. 579–585, 2009.

[29] A. De Boer, A. H. Van Zuijlen, and H. Bijl, "Advanced Computational Methods in Science and Engineering," *Adv. Comput. Methods Sci. Eng.*, vol. 71, pp. 143–178, 2010.

[30] a. Turon, P. P. Camanho, J. Costa, and J. Renart, "Accurate simulation of delamination growth under mixed-mode loading using cohesive elements: Definition of interlaminar strengths and elastic stiffness," *Compos. Struct.*, vol. 92, no. 8, pp. 1857–1864, 2010.

[31] B. Gözlüklü and D. Coker, "Modeling of the dynamic delamination of L-shaped unidirectional laminated composites," *Compos. Struct.*, vol. 94, no. 4, pp. 1430–1442, 2012.

[32] M. F. S. F. de Moura and J. P. M. Gonçalves, "Cohesive zone model for high-

cycle fatigue of adhesively bonded joints under mode I loading," *Int. J. Solids Struct.*, vol. 51, no. 5, pp. 1123–1131, 2014.

[33] B. Gozluklu, I. Uyar, and D. Coker, "Intersonic delamination in curved thick composite laminates under quasi-static loading," *Mech. Mater.*, vol. 80, pp. 163–182, 2015.

[34] B. Bartan, A. Kayran, and B. Acar, "Parametric Study of Delamination Analysis in Composites with Cohesive Zone Method," *8th Ankara Int. Aerosp. Conf.*, pp. 1–13, 2015.

[35] L. Zhao, Y. Gong, J. Zhang, Y. Chen, and B. Fei, "Simulation of delamination growth in multidirectional laminates under mode I and mixed mode I / II loadings using cohesive elements," *Compos. Struct.*, vol. 116, pp. 509–522, 2014.

[36] A. Turon, C. G. Dávila, P. P. Camanho, and J. Costa, "An engineering solution for mesh size effects in the simulation of delamination using cohesive zone models," *Eng. Fract. Mech.*, vol. 74, no. 10, pp. 1665–1682, 2007.

[37] T. Diehl, "Modeling Surface-Bonded Structures with ABAQUS Cohesive Elements : Beam-Type Solutions," *2004 ABAQUS Users' Conf.*, pp. 1–27, 2004.

[38] H. Khoramishad, a. D. Crocombe, K. B. Katnam, and I. a. Ashcroft, "Predicting fatigue damage in adhesively bonded joints using a cohesive zone model," *Int. J. Fatigue*, vol. 32, no. 7, pp. 1146–1158, 2010.

[39] P. W. Harper and S. R. Hallett, "Cohesive zone length in numerical simulations of composite delamination," *Eng. Fract. Mech.*, vol. 75, no. 16, pp. 4774–4792, 2008.

[40] A. Turon, C. G. Davila, P. P. Camanho, and J. Costa, "An Engineering Solution for Using Coarse Meshes in the Simulation of Delamination with Cohesive Zone Models," no. March, 2005.

[41] A. Carpinteri, P. Cornetti, F. Barpi, and S. Valente, "Cohesive Crack Model Description of Ductile to Brittle Size - Scale Transition: Dimensional Analysis vs. Renormalization Group Theory," *Eng. Fract. Mech.*, vol. 70, pp. 1809–939, 2003.

[42] C. G. Davila, P. P. Camanho, and M. Moura, "Mixed-Mode Decohesion

Elements for Analyses of Progressive Delamination," *42nd AIAA/ASME/ASCE/AHS/ASC Struct. Struct. Dyn. Mater. Conf.*, 2001.

[43] B. Bartan Kumbasar, B. Acar, and A. Kayran, "Three - Dimensional Delamination Analysis in Composite Open Hole Tensile Specimens with Cohesive Zone Method," *57th AIAA/ASCE/AHS/ASC Struct. Struct. Dyn. Mater. Conf.*, pp. 1–14, 2016.

[44] Standard(ASTM), "D5528-01 2013. Standard Test Method for Mode I Interlaminar Fracture Toughness of Unidirectional Fiber-Reinforced Polymer Matrix Composites," *Am. Soc. Test. Mater.*, pp. 1–13, 2013.

[45] Standard(DIN-EN), "EN 6034 Determination of interlaminar fracture toughness energy - Mode II - G[IIC]," *Dtsch. Inst. Fur Normung*, pp. 1–11, 1996.

[46] Standard(ASTM), "D3039/D3039M − 14 Standard Test Method for Tensile Properties of Polymer Matrix Composite Materials," *Am. Soc. Test. Mater.*, pp. 1–13, 2015.

[47] G. Belingardi, E. G. Koricho, and A. T. Beyene, "Characterization and Damage Analysis of Notched Cross-Ply and Angle-Ply Fabric GFRP Composite Material," *Compos. Struct.*, vol. 102, pp. 237–249, 2013.

[48] W. Xu, S. I. Thorsson, and A. M. Waas, "Experimental and Numerical Study on Cross-Ply Woven Textile Composite with Notches and Cracks," vol. 132, pp. 816–824, 2015.

[49] M. A. Caminero, S. Pavlopoulou, M. Lopez-pedrosa, B. G. Nicolaisson, C. Pinna, and C. Soutis, "Analysis of adhesively bonded repairs in composites : Damage detection and prognosis," *Compos. Struct.*, vol. 95, pp. 500–517, 2013.

[50] Standard(ASTM), "D5766/D5766M-11 Standard Test Method for Open-Hole Tensile Strength of Polymer Matrix Composite," *Am. Soc. Test. Mater.*, pp. 1–7, 2011.

[51] M. Kortschot and P. Beaumont, "Damage Mechanics of Composite Materials: I. Measurement of Damage and Strength," *Compos. Sci. Technol.*, vol. 39, pp. 289–301, 1990.

[52] R. Vaidya and C. Sun, "Fracture Criterion for Notched Thin Composite

Laminates," *AIAA J.*, vol. 35, no. 2, 1997.

[53]   J. Masters and K. Reifsnider, "An Investigation of Cumulative Damage Development in Quasi-Isotropic Graphite/Epoxy Laminate," *Standard(ASTM)*, 1980.

[54]   M. V Hosur, T. S. Ramamurthy, and S. Anita, "Estimation of impact-induced damage in CFRP laminates through ultrasonic imaging," *NDT&E Int*, vol. 31, no. 5, pp. 59–374, 1998.

[55]   S. Long, X. Yao, and X. Zhang, "Delamination prediction in composite laminates under low-velocity impact," *Compos. Struct.*, vol. 132, pp. 290–298, 2015.

[56]   C. C. Tsao and H. Hocheng, "Computerized tomography and C-Scan for measuring delamination in the drilling of composite materials using various drills," *Mach. Tools Manuf.*, vol. 45, pp. 1282–1287, 2005.

[57]   S. Kolkoori, C. Hoehne, J. Prager, M. Rethmeier, and M. Kreutzbruck, "Quantitative evaluation of ultrasonic C-scan image in acoustically homogeneous and layered anisotropic materials using three dimensional ray tracing method," *Ultrasonics*, vol. 54, no. 2, pp. 551–562, 2014.

[58]   T. Lendze, R. Wojtyra, L. Guillaumat, C. Biateau, and K. Imielinska, "Low Velocity Impact Damage in Glass / Polyester Composite Sandwich Panels," *Adv. Mater. Sci.*, vol. 6, pp. 26–34, 2006.

[59]   A. Adumitroaie and E. J. Barbero, "Beyond plain weave fabrics – II . Mechanical properties," *Compos. Struct.*, vol. 93, no. 5, pp. 1449–1462, 2011.

[60]   X. Tang and J. D. Whitcomb, "Progressive Failure Behaviors of 2D Woven Composites," *J. Compos. Mater.*, vol. 37, no. 14, pp. 1239–59, 2003.

APPENDICIES

APPENDIX A

A.1 CALCULATION of INTERLAMINAR FRACTURE TOUGHNESS, G_{Ic} and G_{IIc}

A.1.1 Calculation Of Mode I Interlaminar Fracture Toughness , G_{Ic} [44]

Mode I test is based on ASTM D5528-13 "Standard Test Method for Mode I Interlaminar Fracture Toughness of Unidirectional Fiber-Reinforced Polymer Matrix Composites" [44]. Mode I interlaminar fracture toughness G_{Ic} is calculated using the double cantilever beam specimen (DCB), shown in Figure A. 1. The lamina of the DCB specimen lie in the 0° direction along the beam span L and delamination growth is permitted in this direction. DCB specimens have uniform thickness. A non-adhesive insert (a thin film) is located on the mid-plane which behaves as the delamination initiator.
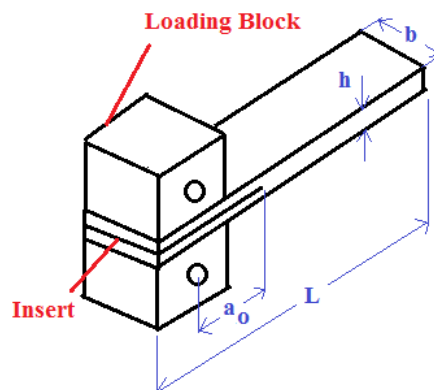
Figure A. 1: Double cantilever beam specimen[44]

G_{Ic} is the critical strain energy release rate for delamination growth caused by the opening load or displacement. Strain energy release rate, G, is the loss of total elastic energy in the test specimen, dU, per unit of specimen width for an infinitesimal increase in delamination length. Strain energy release rate G is given by [44]:

$$G = -\frac{1}{b}\frac{dU}{da} \qquad (A.1)$$

The width and thickness of the DCB specimens are measured and recorded before tests. Both edges of the specimens are painted by a typewriter so as to observe the progression of the delamination. The first 5 mm from the end of the inserted film is marked with thin vertical lines in every 1 mm and the remaining 20 mm is marked with thin vertical lines in every 5 mm, as shown in Figure A. 2. Therefore, the delamination length is sum of the delamination growth calculated from this marks and the distance from the loading line to the end of the film insert.
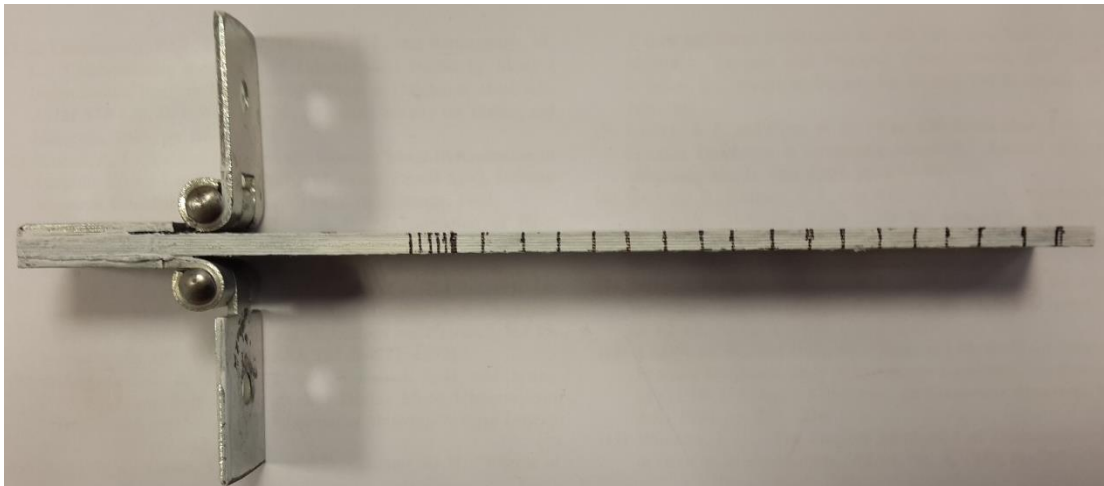
Figure A. 2: The painted DCB specimen for following the delamination

Mode I tests begin with initial loading to eliminate the adverse effects of the adhesive. Preload is also applied because the adhesive at the initial delamination should be eliminated and differences at the position on the two edges should be observed and an asymmetrical loading should be prevented. The specimen is loaded

at a constant rate between 1 and 5 mm/min. The delamination length is recorded and until the delamination growth is 5 mm. Then the specimen is unloaded at a constant rate of 25 mm/min.

The specimen is then reloaded at the same constant rate between 1 and 5 mm/min without stopping. The delamination growth is recorded again. Mode I test is ended when the delamination length becomes at least 45 mm from the tip of the pre-crack. Then the specimen is unloaded at a constant rate of 25 mm/min.

The test machine used in the experiments can be seen in Figure A. 3. The DCB specimen is mounted in the grips of the test machine from its loading blocks. The bottom loading block is clamped and the top loading block is loaded.

Figure A. 3: The test machine for Mode I test

Modified Beam Theory (MBT)

There are three calculation methods in order to obtain G_{Ic}. These are the modified beam theory (MBT), the compliance calibration method (CC) and the modified compliance calibration method (MCC) [44]. In this study, MBT is used for calculating G_{Ic} because in this method, the results are conservative for 80% of the DCB specimens[44].

In the beam theory, strain energy release rate G_I for a double cantilevered beam is given by [44]:

$$G_I = \frac{3P\delta}{2ba} \tag{A.2}$$

where P is the applied load, δ is the load point displacement, b is the specimen width, and a is the delamination length with a_o being the initial delamination length.

Beam theory gives higher G_I when Equation (A.2) is used, because the DCB specimen does not have a fixed-end boundary condition in Mode I tests. So, it is assumed that the DCB specimen contains a slightly longer delamination length given by $a + |\Delta|$ [44]. Δ can be calculated from tests by plotting the delamination length versus the cube root of the compliance $C^{1/3}$. The ratio of the load point displacement to the applied load, δ/P is equal to the compliance, C [44]. Figure A. 4 shows the variation of the cube root of the compliance ($C^{1/3}$) with the delamination length. Δ is the intercept of the leasts squares plot of the ($C^{1/3}$) versus delamination length data with the horizontal axis.
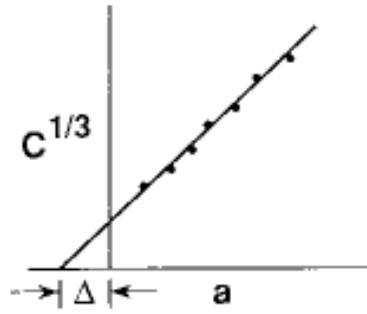

Figure A. 4: Modified beam theory [44]

In the modified beam theory, Mode I interlaminar fracture toughness, G_I is given by Equation (A.3) [44].

$$G_I = \frac{3P\delta}{2b(a+|\Delta|)} \tag{A.3}$$

Figure A. 5 shows the data recorded by the software of the test machine during the Mode I test. These data are collected from the top arm of the test machine (load is applied from the top loading block).

	Initial loading for specimen 2			Reloading for specimen 2		
	A	B	C	D	E	F
1	1_2_pre			1_2		
2	Time	Force	Stroke	Time	Force	Stroke
3	sec	N	mm	sec	N	mm
4	0	0.5	0	0	0.84375	0
5	0.01	0.4375	0	0.01	0.78125	0
6	0.1	0.78125	0.003	0.1	0.65625	0.003
7	0.2	0.78125	0.007	0.2	0.8125	0.008
8	0.3	0.46875	0.013	0.3	0.53125	0.013
9	0.4	0.75	0.018	0.4	0.375	0.019
10	0.5	0.78125	0.023	0.5	0.53125	0.024
11	0.6	1.03125	0.028	0.6	0.71875	0.029
12	0.7	1.125	0.033	0.7	0.6875	0.034
13	0.8	0.5625	0.038	0.8	0.625	0.039
14	0.9	0.625	0.043	0.9	1	0.044
15	1	0.75	0.048	1	0.65625	0.049
16	1.1	1.09375	0.053	1.1	0.9375	0.054
17	1.2	0.90625	0.058	1.2	0.78125	0.059
18	1.3	0.65625	0.063	1.3	0.59375	0.064
19	1.4	0.59375	0.068	1.4	0.625	0.069
20	1.5	0.84375	0.073	1.5	0.71875	0.074

Data continue

Figure A. 5: Load and displacement data recorded by the software of the test equipment-Mode I test

Figure A. 6 shows the basic parameters on the sample calculation page of the fracture toughness for Mode I. [44]. Figure A. 7 shows the variation of the cube root of the compliance ($C^{1/3}$) with the delamination length as in Figure A. 4. Δ is the intercept of the leasts squares plot of the ($C^{1/3}$) versus delamination length data with the horizontal axis. All parameters Figure A. 6 are explained in Table A.1.

Specimen #	2	$a_{present}$	a	Stroke (mm)	Force (N)	C(Stroke/Force)	C^1/3	Stroke-R Stroke (mm)
a_0	45	12	57	13.71	35.59	0.385220568	0.727617533	12.826
width	20.36	15	60	18.6	26.719	0.696133837	0.886266325	17.716
R Stroke	0.884	20	65	19.22	24.438	0.786480072	0.923058532	18.336
R Force	0.75	35	80	25.669	24.25	1.058515464	1.019136609	24.785
		40	85	33.894	19.9	1.70321608	1.194235333	33.01
		45	90	39.394	19.656	2.004171754	1.260796455	38.51
		60	105	48.404	18.875	2.564450331	1.368773003	47.52

Stroke-R Stroke (mm)	Force - R Force (N)	C(Stroke-R Stroke/Force-R Force)	C^1/3 (-Residuals)
12.826	34.84	0.368140069	0.716700482
17.716	25.969	0.682198005	0.880312391
18.336	23.688	0.774062817	0.91817487
24.785	23.5	1.054680851	1.017904467
33.01	19.15	1.723759791	1.199017666
38.51	18.906	2.036919496	1.267626438
47.52	18.125	2.621793103	1.378900108

C^1/3 (-Residuals)	Δ	G_{IC} BT	G_{IC} (-Residuals) BT	G_{IC} (-Residuals, -Preloading)	G_{IC} (-Residuals) MBT	Info
0.716700482	2.0000	0.6307	0.5776		0.5580	preloading
0.880312391	2.0000	0.6102	0.5649	0.5649	0.5467	reloading
0.91817487	2.0000	0.5324	0.4923	0.4923	0.4776	reloading
1.017904467	2.0000	0.5733	0.5364	0.5364	0.5233	reloading
1.199017666	2.0000	0.5846	0.5479	0.5479	0.5353	reloading
1.267626438	2.0000	0.6339	0.5960	0.5960	0.5830	reloading
1.378900108	2.0000	0.6411	0.6043	0.6043	0.5930	reloading
	avg	0.6009	0.5599	0.5570	0.5453	
	std	0.0396	0.0385	0.0413	0.0388	

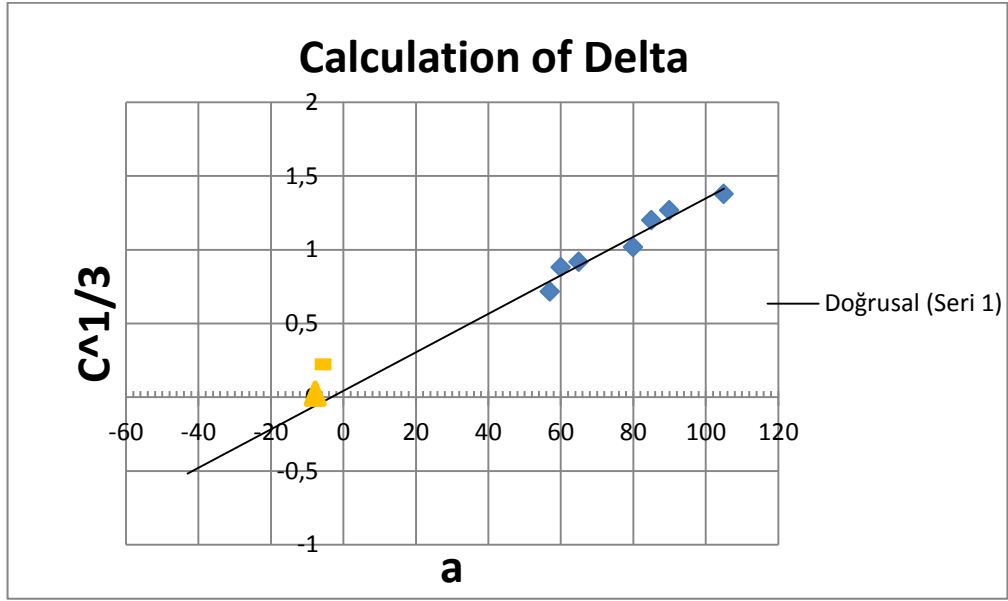Figure A. 6: Sample calculation page of fracture toughness-Mode I

Figure A. 7: Calculation of delta (Δ)

Table A.1: The explanations of the values in sample calculation page

1	Specimen #	Specimen number
2	a_o	Initial delamination length
3	width	Width of the DCB specimen
4	R Stroke	Residual displacement is the displacement on the test machine before the test is performed
5	R Force	Residual applied load is force on the test machine before the test is performed
6	$a_{present}$	Progressive delamination length
7	a	Delamination length ($a_o + a_{present}$)
8	Stroke (mm)	Displacement (load point deflection)
9	Force (N)	Applied load
10	C(Stroke/Force)	Compliance of DCB specimen
11	C^1/3	Cube root of the compliance
12	Stroke-R Stroke (mm)	Displacement without residual displacement
13	Force - R Force (N)	Force without residual force
14	C(Stroke-R Stroke/Force-R Force)	Compliance without residual displacement and force
15	C^1/3 (-Residuals)	The cube roots of compliance without residual displacement and force

16	Δ		Delta, determined experimentally from the curve of the delamination-compliance
17	G_{IC} BT		Opening Mode I interlaminar fracture toughness calculated with Beam Theory
18	G_{IC} (- Residuals) BT		Opening Mode I interlaminar fracture toughness calculated with Beam Theory without residual displacement and force
19	G_{IC} (-Residuals, -Preloading) BT		Opening Mode I interlaminar fracture toughness calculated with Modified Beam Theory without residual displacement, force and preloading
20	G_{IC} (-Residuals) MBT		Opening Mode I interlaminar fracture toughness calculated with Modified Beam Theory without residual displacement and force
21	Info		Test situation

Mode I interlaminar fracture toughness of 10 DCB specimens is calculated by using Equation (A.2) and Equation (A.3) and values are presented in Table A.2. In this study, fracture toughness calculated with MBT (G_{IC} (-Residuals) MBT (J/m^2)) is used because the results are conservative for 80% of the DCB specimens [44].

Table A.2: Results of Mode I tests

Results			
Mode I			
Specimen #	G_{IC} BT (J/m^2)	G_{IC} (-Residuals) BT (J/m^2)	G_{IC} (-Residuals, -Preloading) BT (J/m^2)	G_{IC} (-Residuals) MBT (J/m^2)
1	600.98	524.05	556.98	449.11
2	600.91	559.92	557.01	545.32
3	660.88	551.23	513.37	455.66
4	707.99	562.97	562.62	524.5
5	640.07	490.34	564.02	428.77
6	625.35	511.97	504.49	471.63
7	683.99	571.03	581.87	489.31

8	600.19	500.89	507.79	400.85
9	630.43	516.56	549.1	437.64
10	641.68	559.13	558.77	497.06
Average	**639.25**	**534.81**	**545.60**	**469.99**
Std. Dev.	**36.41**	**29.24**	**26.97**	**44.62**

A.1.2 Calculation of Mode II Interlaminar Fracture Toughness, G$_{IIc}$ [45]

Mode II test is based on DIN-EN 6034 "Determination of interlaminar fracture toughness energy - Mode II - G[IIC]" [45]. Mode II interlaminar fracture toughness, G_{II} is given by Equation (A.4) [29].

$$G_{IIC} = \frac{9Pa^2 d1000}{2w(1/4L^3 + 3a^3)}$$
(A.4)

where P is the critical load to start the crack, a is the initial length of the delamination, d is the crosshead displacement at the onset of delamination , L is the span length, and w is the width of the specimen [45]. The ENF specimen is shown in Figure A.8.
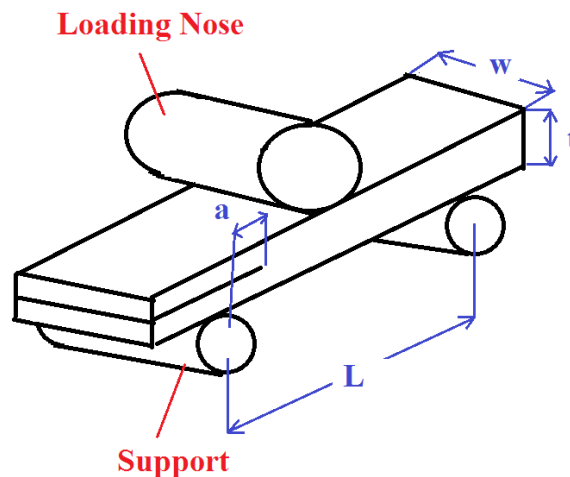

Figure A.8: End notched flexure specimen[45]

The test machine can be seen in Figure A. 9. During the test, the ENF specimen is mounted in supports of the machine as three point bending loading and load is applied from the top support called as the loading nose.
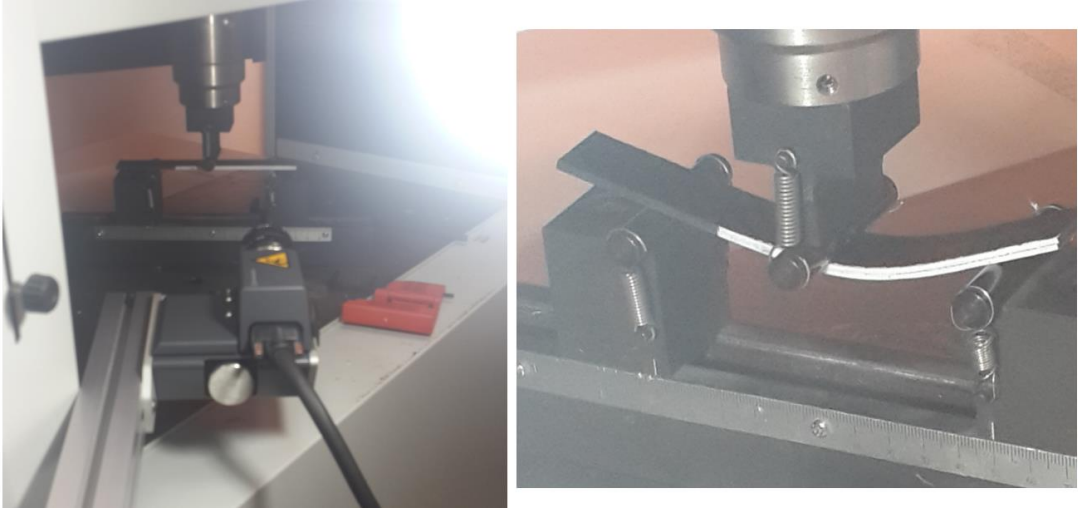

Figure A. 9: The test machine for Mode II test

Figure A.10 shows the data recorded by the software of the test equipment. These data are collected from the top arm of the test machine (load is applied from the loading nose, Figure A.8).

Loading for specimen 1

	A	B	C
1	1_1		
2	Time	Force	Stroke
3	sec	N	mm
4	0	5.46875	0
5	0.05	5.46875	0
6	0.1	5.3125	0.001
7	0.15	5	0.002
8	0.2	4.84375	0.003
9	0.25	5.46875	0.004
10	0.3	5.46875	0.005
11	0.35	5.3125	0.006
12	0.4	5.15625	0.007
13	0.45	5.15625	0.007
14	0.5	5.3125	0.008
15	0.55	5.78125	0.009
16	0.6	5.46875	0.01
17	0.65	6.25	0.011
18	0.7	6.09375	0.012
19	0.75	6.25	0.012
20	0.8	5.46875	0.013
21	0.85	5.15625	0.014
22	0.9	5.3125	0.015
23	0.95	5.78125	0.016
24	1	5.46875	0.017
25	1.05	5.78125	0.017
26	1.1	5.625	0.018
27	1.15	6.25	0.019
28	1.2	5.78125	0.02

Data continue

Figure A.10: Load and displacement recorded by the software of the test equipment-Mode II

Figure A. 11 shows generally basic parameters on the sample calculation page of the fracture toughness for Mode II [45]. All parameters in Figure A. 11 are explained in Table A.3.

	3	4	5	6	7
	Specimen #	w (mm)	Force (N)	d (mm)	G_{IIC} (J/m^2)
1	a (mm)	35	1	19.85	327.1	6.80	1631.43
2	L (mm)	100	2	19.89	322.2	6.96	1641.49
			3	19.88	326.0	6.74	1609.16
			4	19.84	316.1	6.30	1461.38
			5	19.84	308.2	5.81	1314.03
			6	19.88	324.7	6.85	1628.91
			7	19.90	321.3	6.12	1438.63
			8	19.85	308.9	6.20	1404.72
					Avg.	1516.22
					Std. Dev.	126.85

Figure A. 11: Calculation page of fracture toughness-Mode II

Table A.3: The explanations of the values in sample calculation page

1	a	Initial delamination length
2	L	Span length of the ENF specimen
3	Specimen #	Specimen number
4	w (mm)	Width of the ENF specimen
5	Force (N)	Applied load
6	d (mm)	Displacement at the load point
7	G_{IIC} (J/m^2)	Mode II interlaminar fracture toughness

Mode II interlaminar fracture toughness of 8 ENF specimens is calculated by using Eq.(A.4) and values are presented in Table A. 4.

Table A. 4: Results of Mode II tests

Results	
Mode II	
Specimen #	G_{IIC} (J/m^2)
1	1631.43
2	1641.49
3	1609.16
4	1461.38
5	1314.03
6	1628.91
7	1438.63
8	1404.72
Average	**1516.22**
Std. Dev.	**126.85**

APPENDIX B

B.1 THE BENDING EFFECT of THE LOADING POINT IN DCB FINITE ELEMENT MODEL

In the finite element analysis of the DCB specimen, specimen is exposed to pure Mode I loading in opening mode. The location of the one loading block in the DCB specimen is fixed in 3 displacement directions (Ux, Uy, Uz) at point A_{bottom} and in 2 rotation directions (URx, URy) in the region of the initial delamination. The location of other loading block attached to the DCB specimen is fixed in 3 displacement directions (Ux, Uz) at point A_{top} and in 2 rotation directions (URx, URy) at the initial delamination, as shown in Figure B. 1. The applied displacement at A_{top} is 40 mm in +y direction. In this appendix it is shown that the bending effect of the loading point is very important on the analysis results and the stiffness of the DCB specimen. For this purpose, boundary conditions are changed from A_{bottom} and A_{top} to B_{bottom} and B_{top} in order to observe the effect of load application point in the analysis results of DCB test simulation. Figure B. 2 shows the load versus opening displacement curves obtained in the DCB tests and two separate finite element analyses. In the finite element analysis which agrees with the test results, boundary conditions are applied at point A, and when the boundary condition are applied at point B, load displacement curves deviates from the test results.
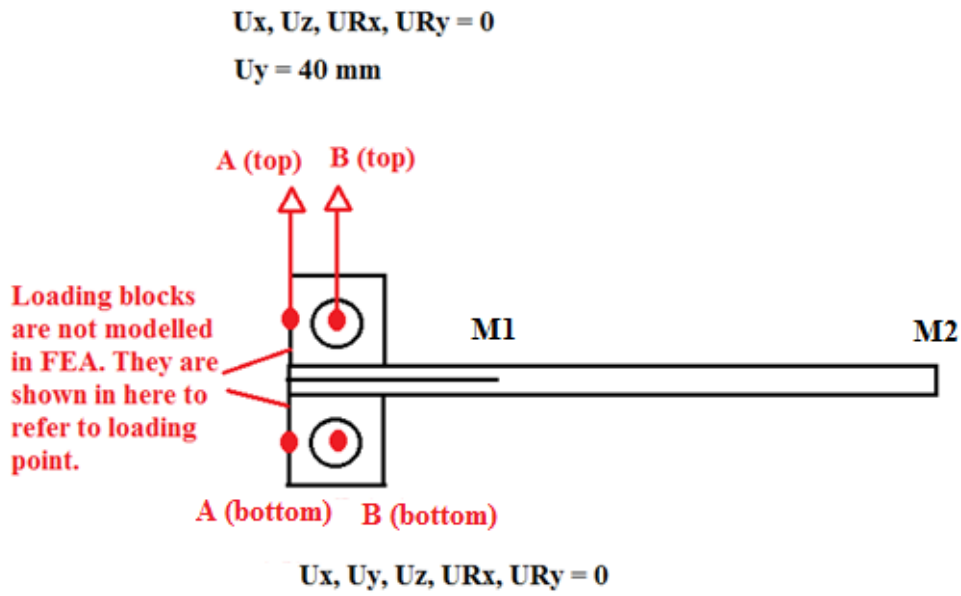
Figure B. 1: Two different boundary condition application points to the DCB specimen in finite element analysis
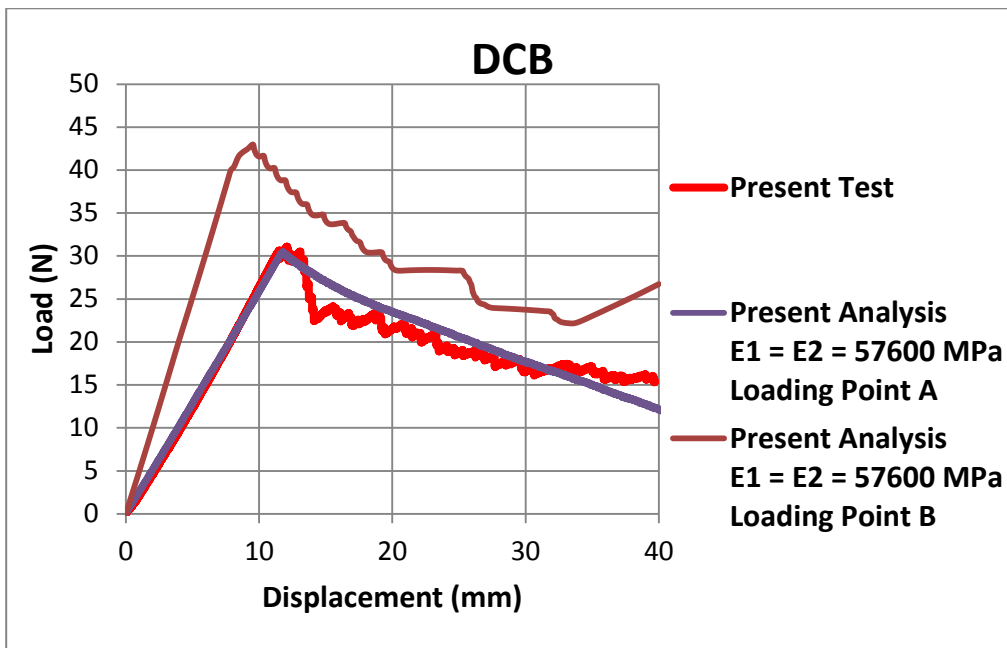

Figure B. 2: The effect of loading point on the finite element analysis results in the DCB test simulation

The bending effect of the loading point is also explained with the bending moment calculations. If the displacement is applied from A_{top} as shown in Figure B. 2, the maximum load is obtained from the results of the finite element analysis as 30.56 N. To generate the same moment effect at the M2, a force of 32.74 N has to be applied at point B_{top}. On the other hand, to generate the same moment at M1, 37.35 N force has to be applied from at point B_{top}. To summarize, to create the same moment effect of the force 30.56 N applied at point A_{top}, one should apply a force between 32.74 N-37.35 N at point B depending on the total delamination length. Thus, the difference between the forces applied at points A_{top} and B_{top} is in the range of 2.18 N – 6.79 N. In the present study, the DCB tests are performed in test machine with 100 kN load capacity. Load cell accuracies of the test machines are normally specified as %1 of the maximum capacity but it is known that loads cells are more accurate than %1 of the maximum capacity. During the DCB test maximum load is the 30-40 N range and for A_{top} and B_{top} loading points maximum force difference is about 7 N. If one assumes that load cell accuracy is %0.01 accurate then the accuracy of the test system is about 10 N. Thus, one can conclude that an incorrect load measurement by 2-7 N is very probable because of the high load cell capacity of the material test system used in the DCB tests. An incorrect load measurement of $2 - 7$ N can create significant effect on the load displacement curve in the DCB test, as shown in Figure B.2. It should also be noted that if the E1 elastic modulus of the twill composite is taken close to the experimentally determined value of 56700 MPa, then the load-displacement curve for the case when the load is applied at point A agrees well with the experimentally determined load-displacement curve. To conclude, the difference between the initial slopes of the experimentally determined load-displacement curve and the load-displacement curve obtained by the finite element analysis using the elastic modulus E1 obtained in the material tests is primarily attributed to the slight errors that might have occurred in the recorded load cell value because of the very low levels of load readings compared to the load cell capacity of the test machine.

APPENDIX C

C.1 MODAL TEST AND ANALYSIS of WINGS (without film)

In this study, modal analyses and tests are performed to obtain natural frequency and verify the elastic moduli in wrap and fill directions of the composite wings without film (W) used to initiate delamination during structural testing.   Therefore, modes of W wings are determined and they are validated by test-finite element analysis comparison. Finite element analyses are performed with 3D solid elements in FEM. Element type used is linear hexahedral element (C3D8), 181994 elements, and 192449 nodes are used in finite element model. Global element size is taken as 2 mm and all plies have 2 elements in thickness direction. In-plane elastic modulus is taken as 65313MPa. Finite element model and material direction of W wings are shown in Figure C. 1 and Figure C. 2.
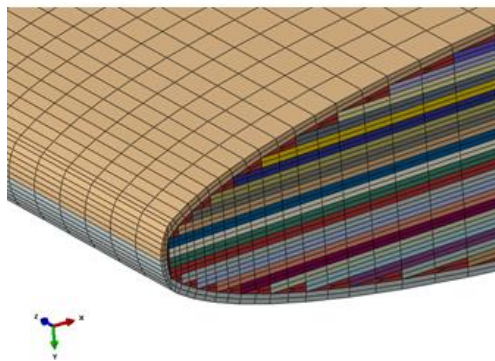
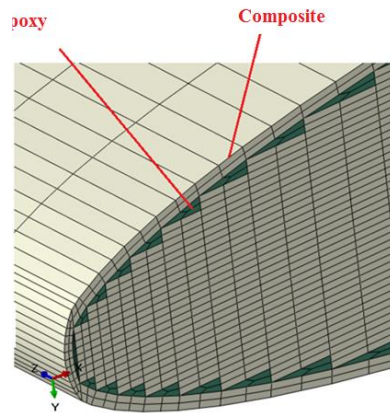Figure C. 1: Finite element model of W wings for modal analysis

Figure C. 2: Material directions for W wings for modal analysis

Finite element analyses are run in order to decide locations of accelerometers before two composites wing are tested. According to mode shapes in analysis results, 9 accelerometers are placed in important locations, as shown in Figure C. 3. As shown in Figure C. 4, modal tests are conducted in free conditions by hanging the wing by elastic rubber to a support arm.
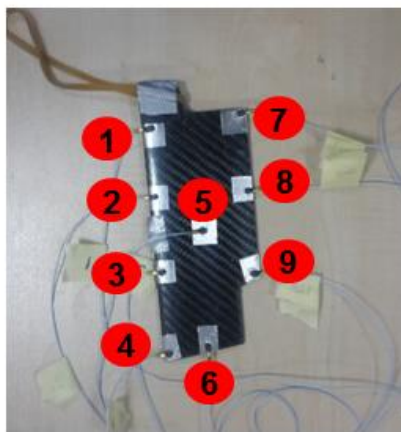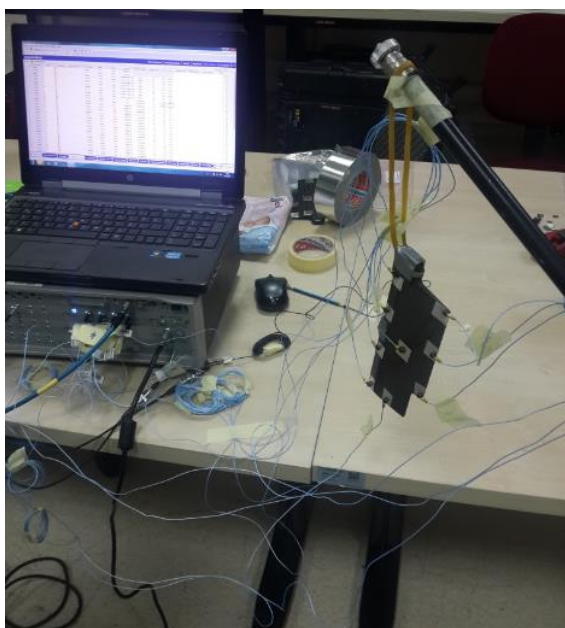

Figure C. 3: 9 Sticky accelerometers in W wings

Figure C. 4: Data acquisition system and modal test of W wings

Experimental results for modal tests of W wing are presented Table C. 1. Two tests are performed by changing the hanging point of the wing.

Table C. 1: Modal test results of the W wings

	W-1	**W-2**
1. Mod (Hz) (1.bending)	824	844
2. Mod (Hz) (1.torsion)	1405	1417
3. Mod (Hz) (2.bending)	2296	2321
4. Mod (Hz) (2.torsion)	2636	2802

W-1 is hung from its root while W-2 is hung from its body to minimize boundary condition effects, as shown in Figure C. 5. It should be noted that to generate the free boundary condition, hanging the wing from its body instead of root is considered to be better for modal test. Thus, the experimental results of W-2 are used to compare against the finite element results.
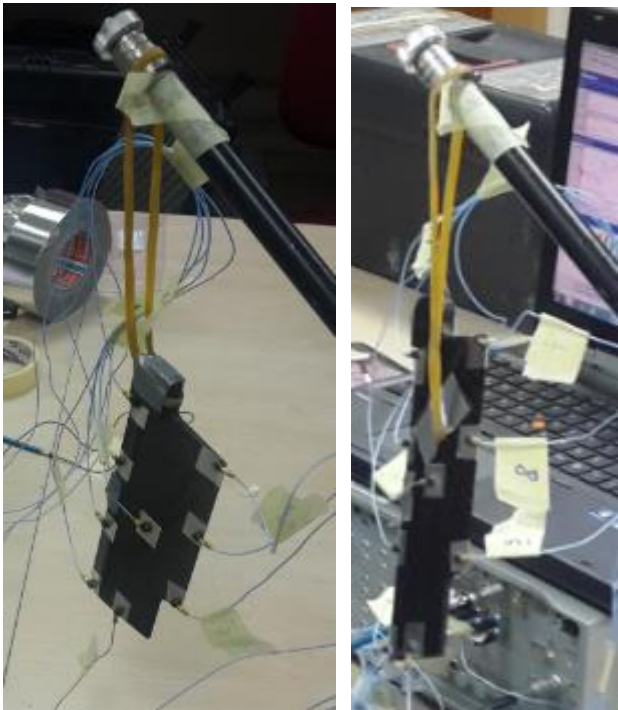

Figure C. 5: Boundary conditions for W-1 and W-2 wings

Figure C. 6-Figure C. 9 compare the modal test and analysis results if in-plane elastic modulus is taken as 65313MPa. It is seen that modal test and analysis results agree with each other within %15. It is also seen that finite element analysis results are consistently higher than the modal test results.
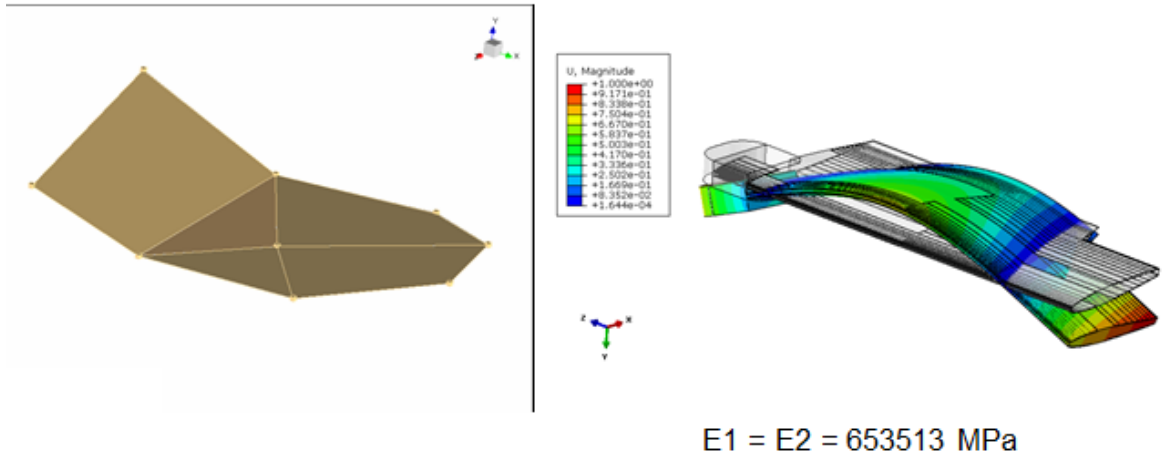
Figure C. 6: Test and analysis results Mode 1- 1.Bending (E1= E2 = 65313 MPa)
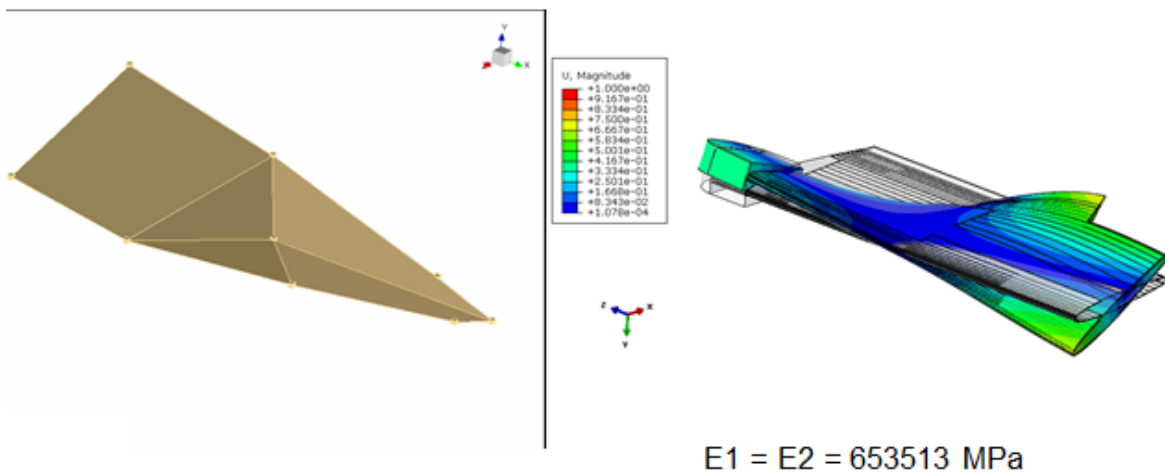
Figure C. 7: Test and analysis results Mode 2- 1.Torsion (E1= E2 = 65313 MPa)
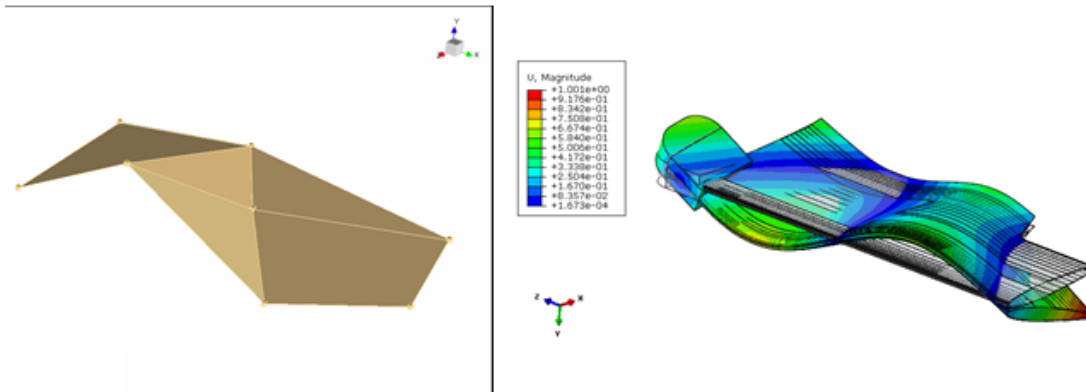
Figure C. 8: Test and analysis results Mode 3- 2. Bending (E1= E2 = 65313 MPa)
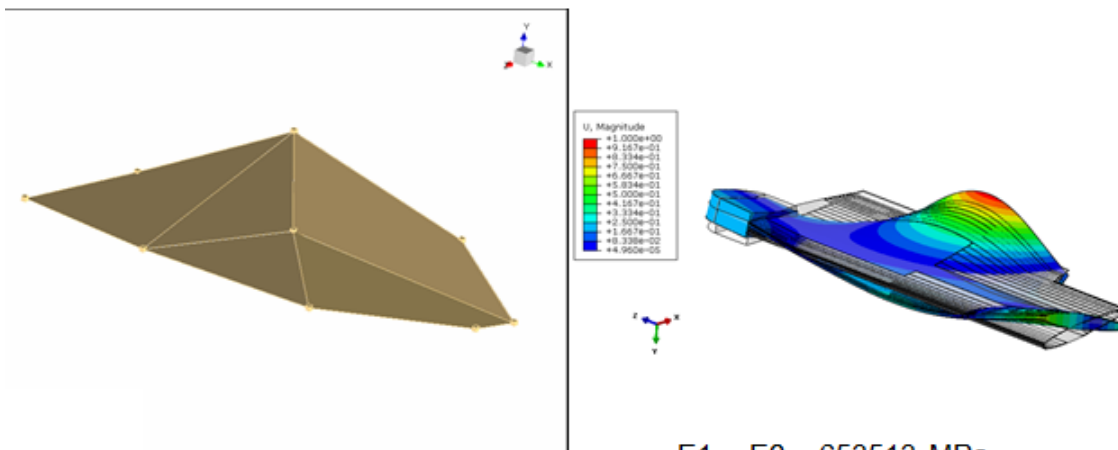
Figure C. 9: Test and analysis results Mode 4- 2.Torsion (E1= E2 = 65313 MPa)

Based on the results given in Table C. 2, it can be said that difference in the frequency in the tests and in the finite element analysis are compatible with elastic moduli 65313 MPa.

Table C. 2: Modal analysis and test results of the W wings

	TEST		ANALYSIS	
	W-1	**W-2**	**(E1 = E2 = 65313 MPa)**	
			W	*Difference (%)*
1. Mod (Hz) (1.bending)	824	844	933.7	*10.6*
2. Mod (Hz) (1.torsion)	1405	1417	1626.8	*14.8*
3. Mod (Hz) (2.bending)	2296	2321	2553.1	*10.0*
4. Mod (Hz) (2.torsion)	2636	2802	3231.7	*15.3*

APPENDIX D

D.1 ANALYSIS of THE SIMPLE COMPOSITE WING

The curves of the load-displacement obtained by the finite element analysis of the missile wings do not show non-linear behavior as the test results. In the main test of the thesis, possible reasons for the non-linear load displacement behavior observed in the tests are attributed to the material and geometrical nonlinearity and progressive failure. Nonlinear constitutive behavior of the matrix of the composite structure, progressive failure of delamination, stiffness reduction in the composite structure, and geometrical nonlinearity such as wavy tows under tensile loading are considered to be the possible reasons of the non-linearity [59]. To study the reason for the non-linearity of the composite missile wings under bending load, finite element analyses of a simpler structure which resembles the missile wing are performed, and the results are presented in APPENDIX D along with the discussions. Simpler wing has a planform shape of trapezoid. The uniform thickness of the simple composite wing is taken as 6 and plies are oriented as $[0^o/45^o]_s$ in the whole wing. Thickness of each layer of the simple wing is taken as 1.5 mm. The elastic moduli in wrap and fill directions ($E_{11}= E_{22}$) for twill material are taken as 65313 MPa for the simple composite wing, as in the actual wing. Finite element analyses are performed with 3D solid linear elements (C3D8) by ABAQUS. The solver of the analysis is selected as the nonlinear solver. The total number of elements is 5104 and the total number of nodes is 6611. Global element size in finite element model changes between from 0.75 mm to 5 mm. Mesh details of the finite element model for the simple composite wings are shown in Figure D. 1. Boundary conditions of finite element model for basic model (Model - 1) are shown in Figure D. 2. The surface-to-surface interaction

with friction coefficient of 0.2 is defined between the simple composite wing and the test set-up. The concentrated load that is applied to the wing is 3000 N and the test set-up is clamped, as shown in Figure D. 2.
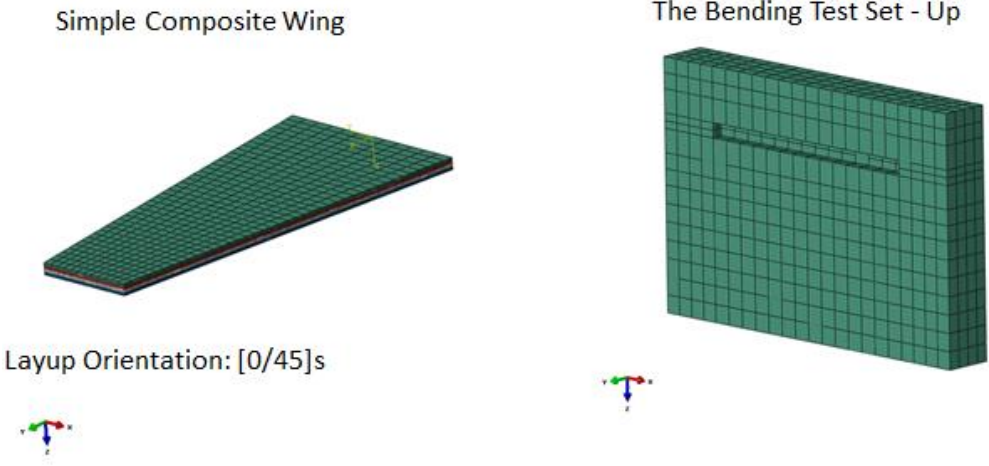

Figure D. 1: Mesh details of finite element model of the simple composite wing
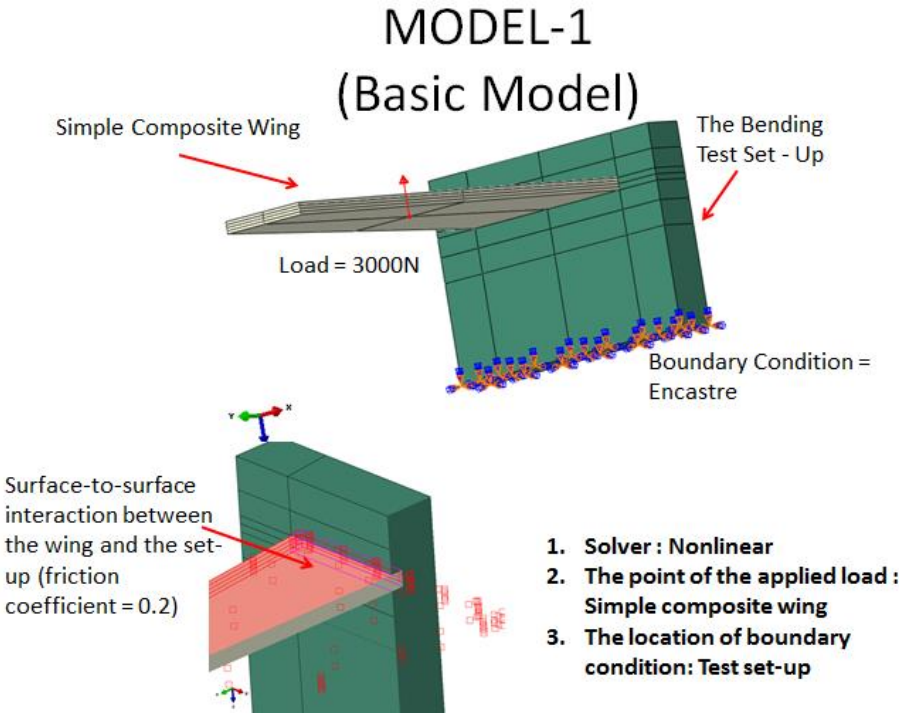

Figure D. 2: Boundary conditions of finite element model of the simple composite wing / Model - 1

Four finite element models are created in order to determine the possible effects of the non-linear behavior. Basic model is Model-1 and all comparisons are made with this reference model. Models are introduced in Table D. 1. The effect of the nonlinear solver and the linear solver is investigated in the comparison of Model – 1 and Model – 2. The effect of the point of the applied load is investigated in the comparison of Model – 1 and Model – 3. In Model -3, a rigid surface is defined and external load load is applied to this rigid surface which is in contact with the wing. Thus, in Model -3 external load is not directly applied on the wing. The effect of the location of the boundary condition is investigated in the comparison of Model – 1 and Model – 4.

Table D. 1: The differences between the finite element models

Model	Solver	The point of the applied load	The location of the boundary Condition
Model-1 (Basic Model)	Nonlinear	Simple Composite Wing	Test Set-Up
Model-2	**Linear**	Simple Composite Wing	Test Set-Up
Model-3	Nonlinear	**Rigid Surface**	Test Set-Up
Model-4	Nonlinear	Simple Composite Wing	**Simple Composite Wing**

Boundary conditions for Model – 2 are shown in Figure D. 3. The surface-to-surface interaction with friction coefficient – 0.2 is defined between the simple composite wing and the test set-up. The concentrated load is applied on the wing as 3000 N and the test set-up is clamped. The solver is chosen as linear solver.
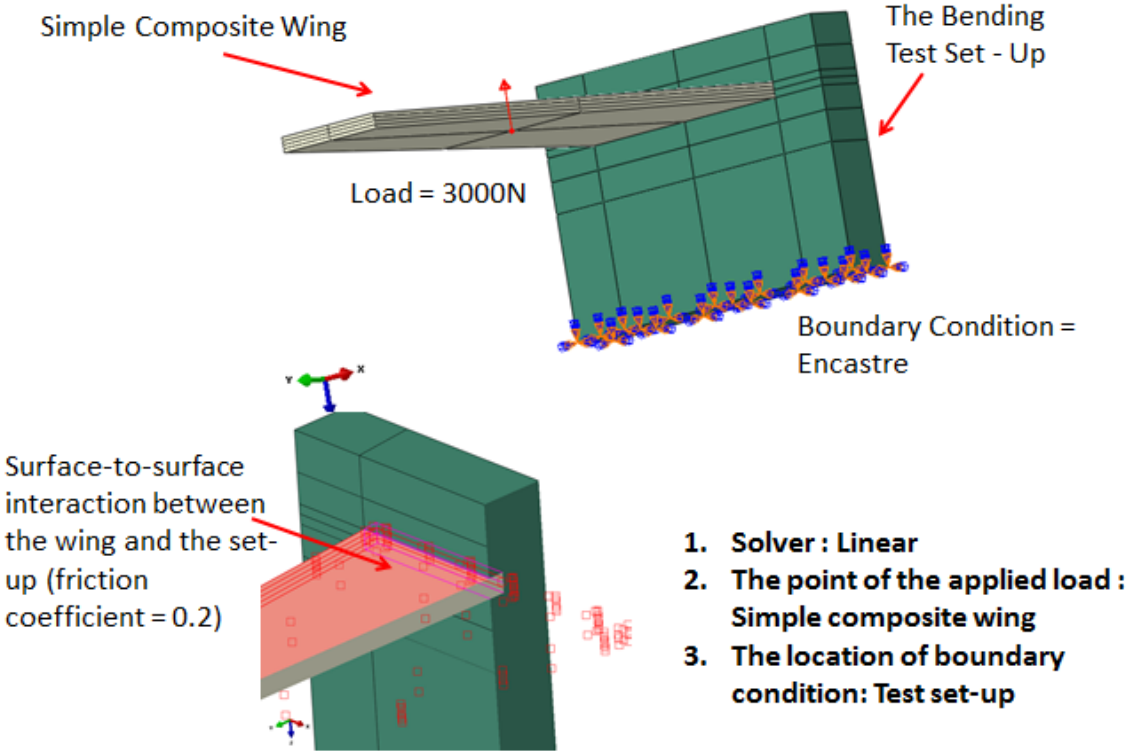
Figure D. 3: Boundary conditions of finite element model of the simple composite wing / Model – 2

Boundary conditions for Model – 3 are shown in Figure D. 4. The surface-to-surface interaction with friction coefficient – 0.2 is defined between the simple composite wing - the test set-up and the wing-the rigid surface. The concentrated load is applied from this rigid surface as 3000 N and the test set-up is clamped. The solver is chosen as nonlinear solver.

MODEL-3

Simple Composite Wing

The Bending Test Set - Up

Surface-to-surface interaction between the wing - the set-up and also the wing – the rigid surface (friction coefficient = 0.2)

Rigid Surface

Load = 3000N

Boundary Condition = Encastre

1. **Solver : Nonlinear**
2. **The point of the applied load : Rigid surface**
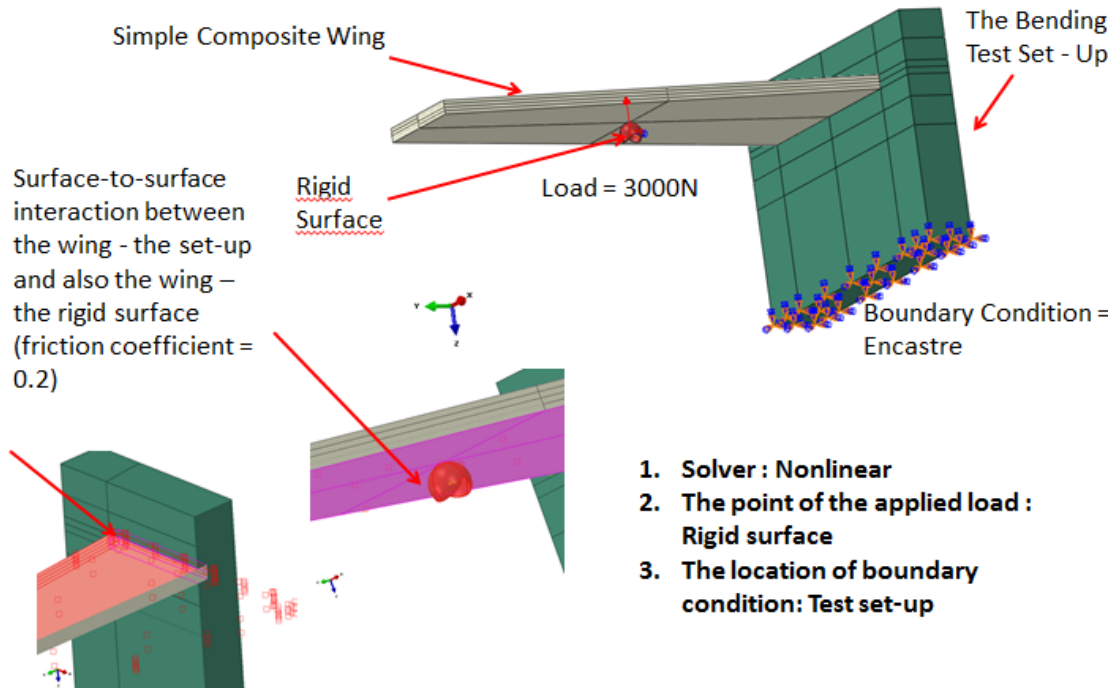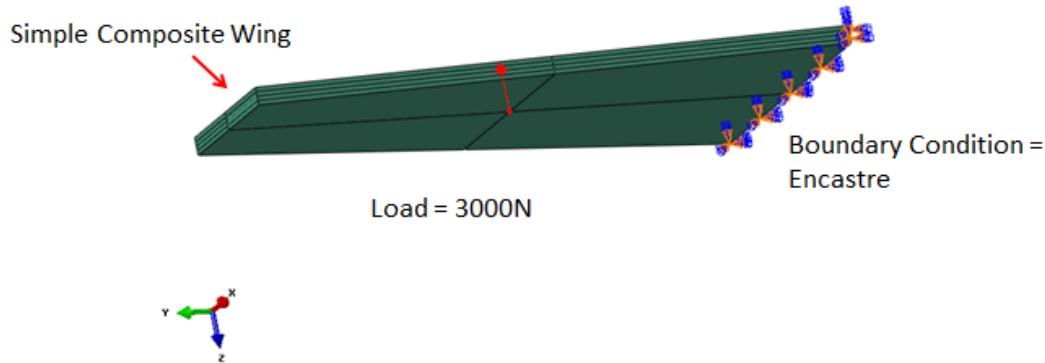3. **The location of boundary condition: Test set-up**

Figure D. 4: Boundary conditions of finite element model of the simple composite wing / Model – 3

Boundary conditions for Model – 4 are shown in Figure D. 5. The test set-up is not modelled. The concentrated load is applied from the wing as 3000 N and the root of the wing is clamped. The solver is chosen as nonlinear solver.

MODEL-4

Simple Composite Wing

Boundary Condition = Encastre

Load = 3000N

1. Solver : Nonlinear
2. The point of the applied load : Simple composite wing
3. The location of boundary condition: Simple composite wing

Figure D. 5: Boundary conditions of finite element model of the simple composite wing / Model – 4

Figure D. 6 compares the load displacement curves obtained by four different analysis models described in Table D. 1. According to the analysis results of the simple composite wing, the location of the boundary condition is more effective than the point of the applied load and the kind of the solver on load – displacement curve. The simple composite wing is stiffer when the root of the wing is clamped instead of clamping the test set-up. Also, the simple composite wing is slightly stiffer if the solver type is linear solver instead of nonlinear solver. From the load displacement results presented in Figure D. 6, it is seen that in none of the models, non-linear load displacement behavior is observed. Therefore, the main reason for the non-linear load displacement behavior observed in the bending tests of the composite wing is primarily attributed to the material nonlinearity at higher load levels and progressive failure occurring in the wing which may also induce material nonlinearity.
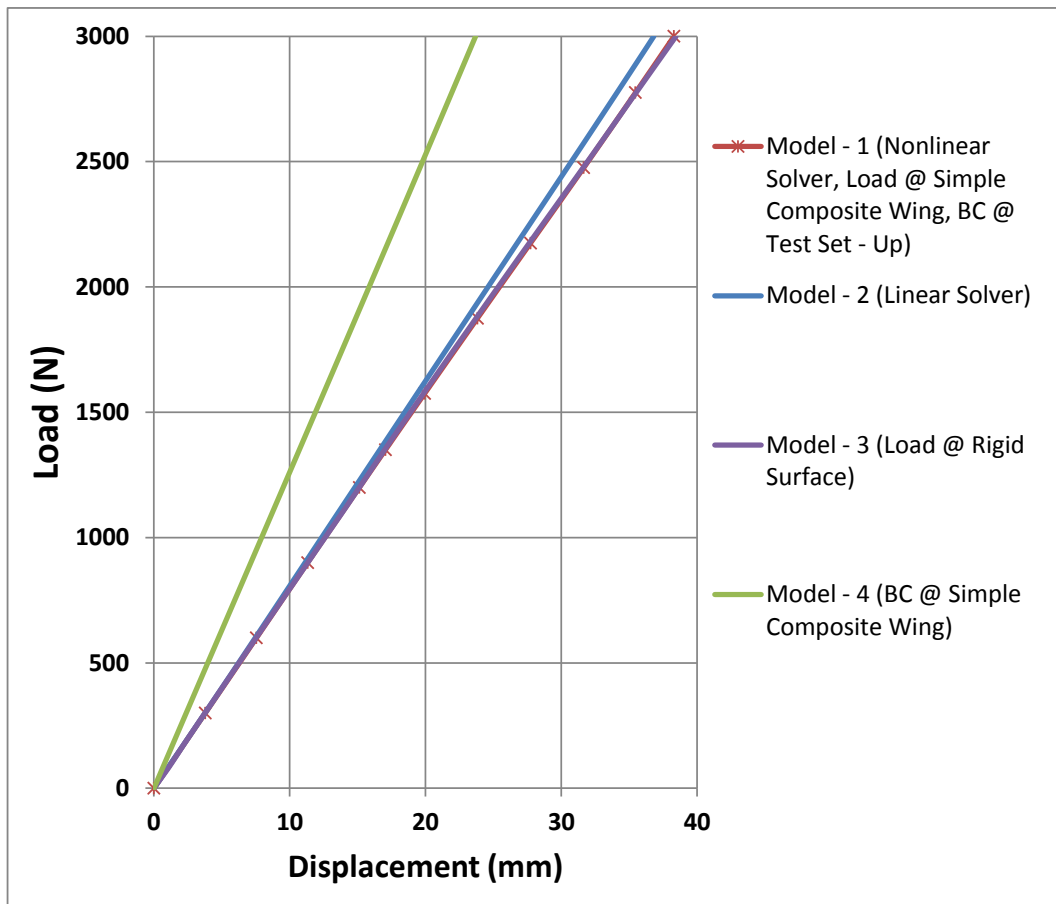
Figure D. 6: Load – displacement curves for different analysis models